Individual beam control in multi electron beam systems

Zonnevylle, Christiaan

DOI
10.4233/uuid:23221904-c9c1-4537-af7f-abdbb9df06ed

Publication date
2017

Document Version
Final published version

Citation (APA)
Zonnevylle, C. (2017). *Individual beam control in multi electron beam systems*. [Dissertation (TU Delft), Delft University of Technology]. https://doi.org/10.4233/uuid:23221904-c9c1-4537-af7f-abdbb9df06ed

Individual beam control in multi electron beam systems

A.C. ZONNEVYLLE

The work presented in this thesis was performed at the Charged Particle Optics group, Department of Imaging Physics, Faculty of Applied Sciences, Delft University of Technology.

This thesis is partially sponsored by MAPPER lithography.

This thesis is a part of NanoNextNL, a micro and nanotechnology innovation consortium of the Government of The Netherlands and 130 partners from academia and industry. More information: www.nanonextnl.nl

ISBN: 978-94-6186-783-4

An electronic version is available at: http://repository.tudelft.nl/

Individual beam control in multi electron beam systems

Proefschrift

ter verkrijging van de graad van doctor
aan de Technische Universiteit Delft,
op gezag van de Rector Magnificus prof.ir. K.C.A.M. Luyben;
voorzitter van het College voor Promoties,
in het openbaar te verdedigen op
maandag 6 februari 2017 om 10:00 uur

door

Aernout Christiaan Zonnevylle
Natuurkundig ingenieur Technische Universiteit Delft
geboren te Leiderdorp, Nederland

This dissertation has been approved by the
promotor: Prof.dr.ir. P. Kruit

Composition of the doctoral committee:

Rector Magnificus	chairman
Prof.dr.ir P. Kruit	Delft University of Technology

Independent members:

Prof.dr.ir. N. de Jong	Delft University of Technology
Prof.dr.ir. J.L. Herder	Delft University of Technology
Prof. dr. P.M.Sarro	Delft University of Technology
Prof.dr.ir. M. Steinbuch	Eindhoven University of Technology
Dr.ir. Jacob Hoogenboom	Delft University of Technology
Dr. H.W. Mook	Mapper Lithography

Ch. 1 Introduction

In this era of information technology everyone uses semiconductor devices (or so called chips), as they are nowadays present in virtually every electronic device. Society expects the next generation of devices to be even faster and better performing. To achieve this goal the functional patterns on these chips need to shrink every time. This trend of continuous downscaling is known as Moore's law, formulated by Gordon Moore in 1965[1]. Moore's law projects the critical dimension for downscaling by a factor of 0.94 every 2 years. This law is also included in the International Roadmap for Semiconductors (ITRS)[2], see figure 1.

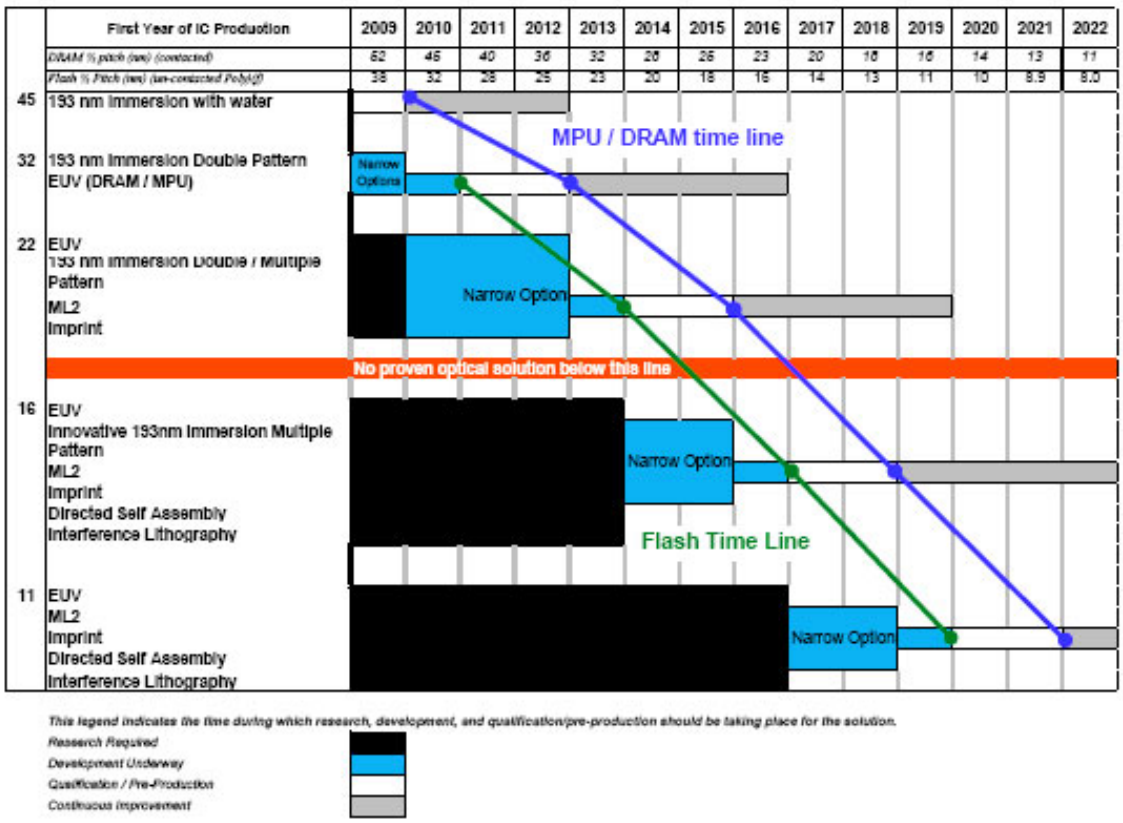

Figure 1: International Roadmap for Semiconductors (ITRS)[2]

Depicted in figure 1 we see a red line which indicates that there are no proven optical solutions yet when considering a desired throughput of 100 wafers per hour (wph). There are technologies available to create patterns sub 5nm [3–6][that can be used for the fabrication of devices, but none of these can yet deliver the required throughput of 100 wph.

For the next generation lithography tools, as the future technologies below the red line are named, there are two categories of possible technology solutions: **direct write approaches** such as imprint [7,8], maskless lithography (ML2)[9][10] and extreme ultra violet (EUV)[11,12]and **indirect approaches** such as directed self-assembly[13], pitch division lithography[14] and double(multiple) patterning. Expectations are that the second category of indirect approaches can be used up to the 16 nm node [15]. Beyond this node other solutions were still unknown at the time of writing this thesis. We think that ML2 direct writing will become one of the new dominant technologies for the semiconductor industry, especially for small series productions in which the costs of mask are too high.

The scope of this thesis is about a ML2 technology based on multi beam electron beam lithography. In the introduction we have therefore limited ourselves to electron beam lithography technology, a maskless direct write technology.

The scanning electron beam as lithography tool.

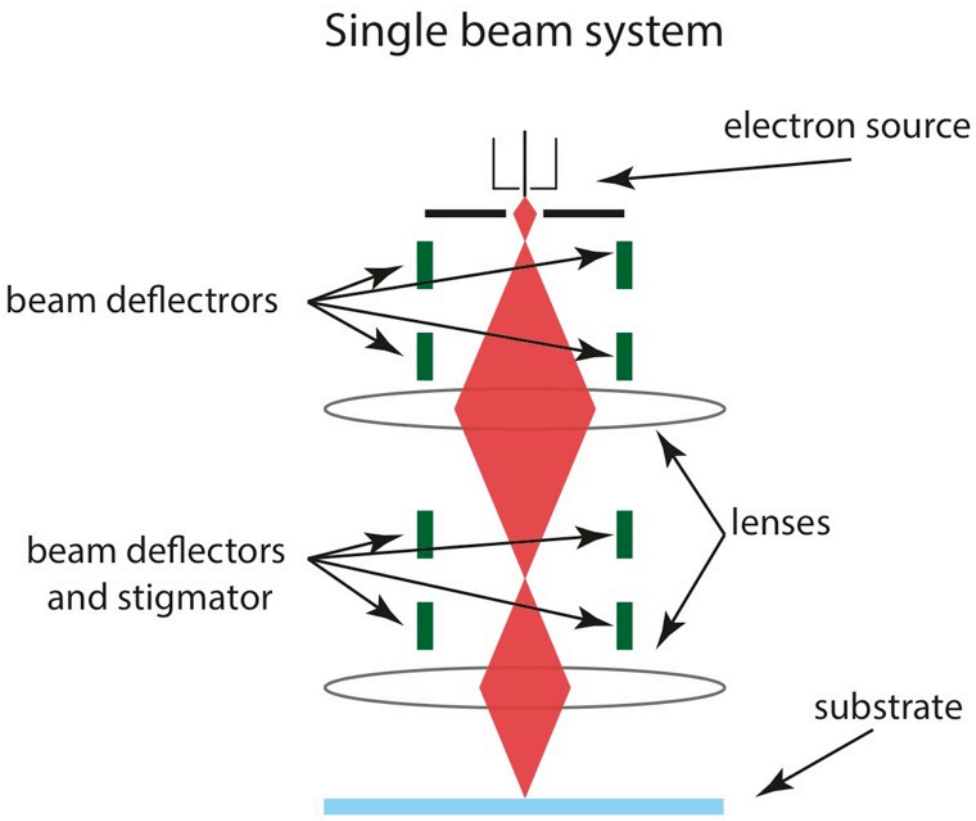

Figure 2: Schematic setup of a scanning focused electron beam system.

Figure 2 shows a schematic sketch of a scanning focused electron beam system that can be used for lithography enabling patterning with characteristic dimensions of sub 5 nm [4,5,16–18]. Focused electron beams are more than able to reach the needed features size as set by the ITRS roadmap, but are they fast enough to have a throughput of 100 wafer per hour?
The throughput is determined by the time required to pattern a 300mm wafer. This is the so-called exposure time and is determined by:

$$t = \frac{c \cdot A \cdot D}{d_I}$$

where t is the required exposure time, c is the pattern coverage of the wafer, A is the total wafer area, D is the required electron dose per area and d_I is the electron beam current. To give a realistic example: for a 300mm wafer with a wafer coverage of c=50%, a dose of 30μC/cm^2 [19,20] is needed for the 22 nm node and with a beam current of d_I=6 nA it leads to an exposure time of 20.4 days for one wafer. The required exposure time is 36 sec per wafer in order to reach the 100wph throughput target. A possible solution would be to increase the beam current to 294 μA. Unfortunately this is not possible in an electron beam system, without losing the required resolution of 22nm or below.
This is due to the relation between probe size and probe current:

$$I_p = B_r \frac{\pi^2}{4} d_p^2 \alpha^2 V$$

where B_r is the reduced brightness, d_p is the probe size, α is half the opening angle of the aperture and V is the beam potential. In the previous calculation example for the exposure time we have used B_r=1x10^7 [Am^{-2}s**r**$^{-1}$V^{-1}], α=10 [mRad], d_p=22 [nm] and V=5 [kV], which are typical values. Unfortunately the probe size, opening angle and beam potential cannot be changed independently since they are related [21]. The reduced brightness is a unique property of the electron source and is invariant in any electron-column. Increasing the reduced brightness will increase the probe current for the given parameters. However, the maximum reduced brightness of existing electron sources is in the order of B_r=1x10^9 [Am^{-2}s**r**$^{-1}$V^{-1}]. This is by far insufficient for the required throughput, while discarding the fact that a high-reduced brightness source does not automatically mean that the source can deliver the needed total current.

The throughput can be increased drastically by splitting up the beam in multiple beamlets and, as long we can treat the reduced brightness as an invariant property, the total exposure current I_{total} goes up. As a result exposure times go down as well.

$$I_{total} = n \cdot B_r \frac{\pi^2}{4} d_p^2 \alpha^2 V$$

A system with a probe current of 6 nA per beamlet would require 49.087 beamlets for the 22 nm node. Current literature describes four different multi beam system configurations [22], as sketched in figure 3. Figure 3a is a sketch of a single source single column where

the beam has been split in multiple beamlets by an aperture array and the beamlets are demagnified by macroscopic lenses into nanometer sized probes[23–26]. Figure 3b is a sketch of a multi source single column system where the individual sources are demagnified by macroscopic lenses into nanometer sized probes [27,28] Figure 3c is a sketch of a single source multi beam column where the beam originating from the source is split in multiple beamlets that are demagnified by individual micro columns. Figure 3d is a sketch of a cluster of individual columns that each have their demagnification lenses [28,29].

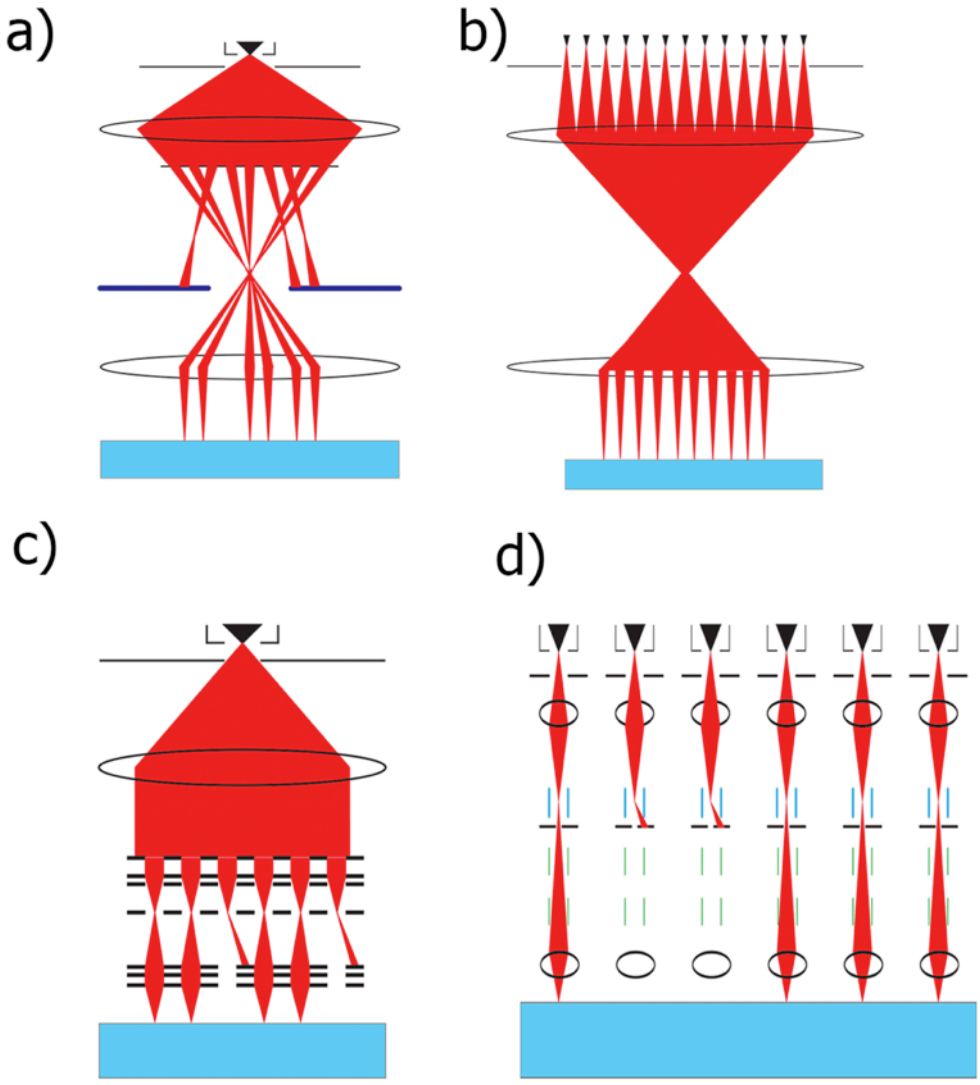

Figure 3: Various multi electron beam schematic system setups; a) Single colum-Single source b) Single column-Mulitiple sources c) Multiple columns-Single source d) Multiple columns-Multiple sources

All the sketched concepts of figure 3 could work if and only if stochastic coulomb interactions could be neglected. The coulomb interactions are the interactions between the individual electrons and are responsible for blurring of the finely focused electron beam spot. For more information see chapter 7 of the Handbook of Charged Particle Optics [30] and Jansen et al.[31,32]. These interactions are most dominant in regions of the beam where high current densities are present, such as in beam cross-overs [33–35] Due to these interactions, the multi beam concepts sketched in figure 3a-b are not suited for high throughput systems and shall not be discussed further.

This leaves the clustered single beam systems and the single source multi column approach. The clustered single beam system, depicted in Figure 3 d could be viable but it is an enormous engineering challenge to cluster 49.087 single columns [36]into an acceptable footprint [37]. This would only be feasible when it is possible to miniaturize all emitters to fit in a miniaturized optical multi beam system. Currently it has not been possible to do this for lithography systems with their strict requirements of throughput.

The concept depicted in Figure 3 c is being developed since 2001 by MAPPER Lithography bv. This makes MAPPER, during the writing of this thesis, the only known competitor for ML2[38,39] able to get near the 100 wph target with an electron beam lithography system.

The Mapper machine

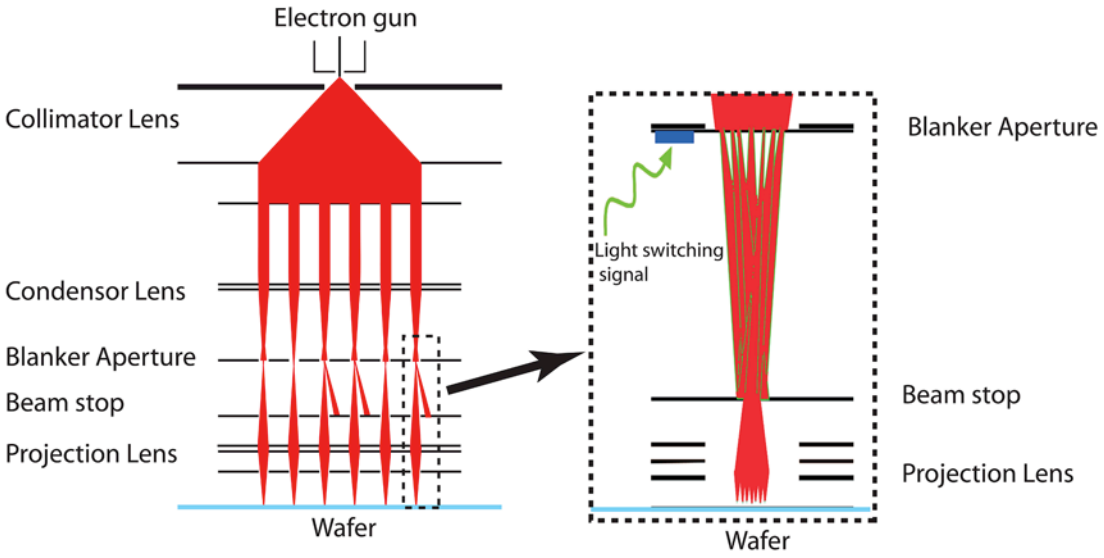

Figure 4: Schematic system design of the MAPPER system, whereby the every beam is separated agan in multiple beam at the blanker aperture into 49 individual controlable sub beams.

Figure 4 shows a sketch of the current Mapper design for a 10 wph throughput machine. This machine will have 13,260 parallel electron beams per unit, delivering 170 μA to the wafer [38–40]. To realize this large current and a sufficiently small spot size at the wafer MAPPER uses a patterned beam approach where each beam consists of 49 sub beams, as is illustrated in the inset of Figure 4 [39]. Clustering ten of these units enables a competitive high throughput 100wph machine for the 22nm node and beyond [38–40].

Figure 5 shows the progressing of the obtainable resolution with the MAPPER system [39] and is capable of patterning 16 nm half pitch lines[41]. Next step is to reach their 10wph target per machine so that the cluster can deliver the needed throughput of 100wph.

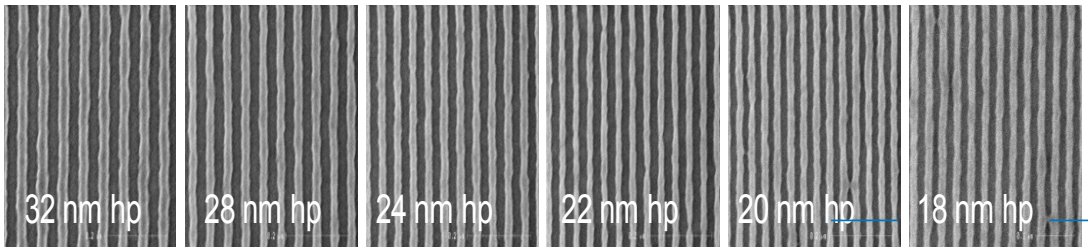

Figure 5: Results of the mapper machine that were published in Wieland et al. [39]**.**

In the MAPPER column a single electron source is split into multiple beamlets each having their own individual columns which are later again split into the 49 sub beams at the blanker. The pitch in the MAPPER design between the individual beamlets is 150 µm and the pitch between the sub beams is in the sub 5 µm regime. As a consequence these electron optical components can only be made with micro/nano fabrication technology [42]. Every electrostatic lens for each beamlet has the same strength and cannot be changed individually, since they are array lenses made out of one piece. The only component that has individual control is the beam blanker for each sub beam[39].

In comparing the MAPPER system with a single beam column as is sketched in Figure 2, we note that the single beam column has beam deflectors and a stigmator, without which it would be impossible to create finely focused electron beams of nanometer size.

In the MAPPER system there are no individual beam deflectors or stigmators for individual beam correction of the beamlets. Alignment in the MAPPER system is reached by extremely precise shaping of the micro fabricated lens arrays [42] which is possible nowadays with current micro/nano fabrication technology [43]. Additionally, special tools have been developed for building up these multi beam lenses from the array electrodes; lateral alignment between the array electrodes must be better than <1µm after stacking. The alignments between the multi beam lens stacks are obtained by precise mechanical alignment and/or sometimes with macroscopic beam deflectors that can deflect the array of beamlets at once in the x/y direction.

To be able to continue the roadmap, specifications must be improved in the near future. Just like regarding a single beam, tool the following sequential improvement strategy can also be applied for a multi beam tool like the MAPPER system, since every beamlet can be seen as single beam with its own column to improve its specifications.

1) Individual beam alignment.
2) Individual focus.
3) Individual stigmation.

Scope of this thesis

In order to continue the development of multi beam technology, the alignment between the multi beam array lenses as well as the individual alignment of each beamlet in its own column will increase in importance and become essential as a first step in improving the system.

This kind of research and development will not only impact future generations of the MAPPER system, but also other applications with multi electron beam technology such as inspection and high throughput microscopy, whereby beam alignment will be the first step in improvement.

The work reported in this thesis focuses on two possible alignment technologies that could be implemented in multi beam systems in order to achieve better individual beamlet alignment and related equipment for multi electron beam MEMS components. We did not study focus and stigmation improvement in this thesis as these are the second and third step in improvement and both have a degree of dependency on beam misalignments that needs to be addressed first.

Topics of research:

'One knob' alignment, to correct rotation misalignment between array blocks placed at different positions along the beam path

Individual beam control, to control each beamlet independently

In the first research topic we looked at alignment solution between blocks of multi beam lenses, where we have, for example, a rotation misalignment that cannot be solved with beam deflectors as depicted in Figure 6. The solutions we explore are novel ideas in that we incorporated intentional asymmetry in multi beam micro lenses as a function tangential to the rotation center. This is discussed in chapters 2 and 3.

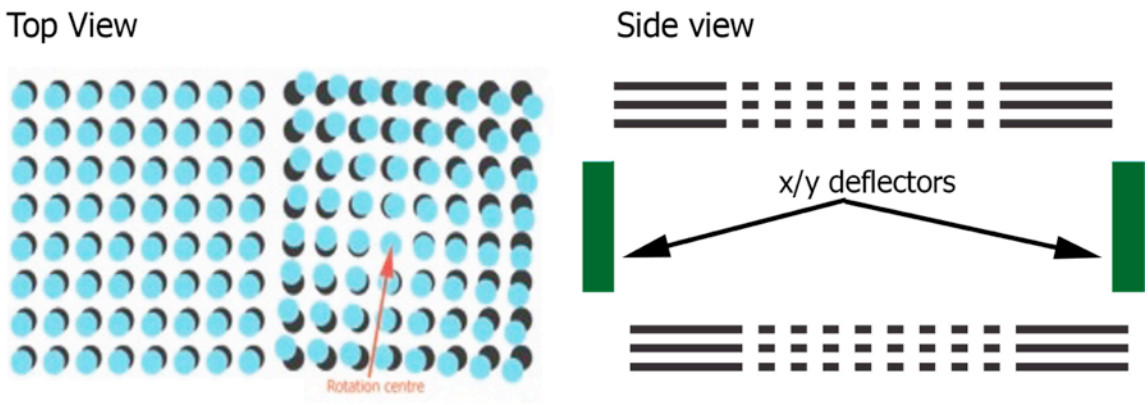

Figure 6: Array rotation errors that can occur between the building array blocks of a multibeam system that cannot be solved with macroscopic beam deflectors

The second research topic studies a possible engineering solution for incorporating truly individual beam control for every beamlet without running into unsolvable practical issues when being scaled up to 13000 or more individual beamlets. This is discussed in chapter 4.

In order to produce functional multi electron beam elements, we found it necessary to develop a new alignment tool which is capable of sub-micron alignment and bonding of these specific elements. This tool has been designed keeping in mind that university research changes very rapidly and flexibility is needed in using it in multiple applications with limited funds and time. This is discussed in chapter 5.

In order to test the electron optical properties of new multi beam elements, we decided to use a modified scanning electron microscope instead of developing a dedicated experimental set-up for each experiment. For this purpose we have developed an integrated optical microscope inside a SEM. This microscope can be used to study multi beam components in combination with a fluorescent screen. Another application of this platform is its use for correlative microscopy study of biological samples with a high NA fluorescent light microscope and scanning electron imaging. This is discussed in chapter 6.

We would like to inform the reader that most of the chapters are intended for publication or are already published and can therefore be read independently. Unfortunately this leads to some information appearing more than once.

Reference:

[1] G.E. Moore, L. Fellow, Proc. IEEE 86 (1998) 82.
[2] www.itrs.gov
[3] W.F. Van Dorp, B. Van Someren, C.W. Hagen, P. Kruit, P.A. Crozier, Nano Lett. 5 (2005) 1303.
[4] A.E. Grigorescu, M.C. Krogt, E.W.J.M. van der Drift, C.W. Hagen, Joutnal of Micro/Nanolithography, MEMS, MOEMS 7 (2008).
[5] V.R. Manfrinato, L. Zhang, D. Su, H. Duan, R.G. Hobbs, E.A. Stach, K.K. Berggren, Nano Lett. 13 (2013) 1555.
[6] J.C. van Oven, F. Berwald, K.K. Berggren, P. Kruit, C.W. Hagen, J. Vac. Sci. Technol. B Microelectron. Nanom. Struct. 29 (2011) 06F305.
[7] S.Y. Chou, P.R. Krauss, P.J. Renstrom, S.Y. Chou, P.R. Krauss, P.J. Renstrom, Appl. Phys. Lett. 3114 (1995) 15.
[8] S.Y. Chou, P.R. Krauss, W. Zhang, L. Guo, L. Zhuang, S.Y. Chou, P.R. Krauss, W. Zhang, L. Guo, L. Zhuang, J. Vac. Sci. Technol. B 15 (1997) 2897.
[9] P. Brandt, C. Sardana, D. Ibbotson, M. Wieland, A. Fay, I. Drive, S. Jose, G. Cedex, Proc. SPIE 9423 (2015) 1.
[10] L. Pain, S. Tedesco, C. Constancias, Comptes Rendus Phys. 7 (2006) 910.
[11] J.E. Bjorkholm, Intel Technol. J. Q3 (1998) 1.
[12] T. Ito, S. Okazaki, Nature 406 (2000) 1027.
[13] B. Copolymers, B.J.Y. Cheng, C.T. Rettner, D.P. Sanders, H. Kim, D. Hinsberg, Adv. Mater. 20 (2008) 3155.
[14] M.C. Smayling, V. Axelrad, K. Tsujita, H. Yaegashi, Proc. SPIE 8326 (2012) 1.
[15] C. Bencher, H. Dai, Y. Chen, Proc. SPIE 7274 (2009) 1.
[16] H. Duan, D. Winston, J.K.W. Yang, B.M. Cord, V.R. Manfrinato, K.K. Berggren, J. Vac. Sci. Technol. B Microelectron. Nanom. Struct. 28 (2010) C6C58.
[17] A.E. Grigorescu, M.C. van der Krogt, C.W. Hagen, P. Kruit, Microelectron. Eng. 84 (2007) 822.
[18] A.E. Grigorescu, C.W. Hagen, Nanotechnology 20 (2009) 292001.
[19] P. Kruit, S. Steenbrink, Scanning 28 (2006) 20.
[20] P. Kruit, S. Steenbrink, R. Jager, M. Wieland, J. Vac. Sci. Technol. B 22 (2004) 2948.
[21] J.E. Barth, P. Kruit, Optik (Stuttg). 101 (1996) 101.
[22] R.F. Pease, J. Vac. Sci. Technol. B 28 (2010) C6A1.
[23] M. Muraki, S. Gotoh, J. Vac. Sci. Technol. B 18 (2000) 3061.
[24] M.J. van Bruggen, B. van Someren, P. Kruit, J. Vac. Sci. Technol. B 23 (2005) 2833.
[25] A. Mohammadi-Gheidari, P. Kruit, Nucl. Instruments Methods Phys. Res. Sect. A 645 (2011) 60.
[26] A. Mohammadi-Gheidari, C.W. Hagen, P. Kruit, J. Vac. Sci. Technol. B 28 (2010) C6G5.
[27] A.K. Dokania, P. Kruit, in:, Tech. Dig. 20th Int. Vac. Nanoelectron. Conf. IVNC 07, 2007, pp. 52–53.

[28] M. Mankos, S. Coyle, A. Fernandez, A. Sagle, P. Allen, W. Owens, J. Sullivan, T.H.P. Chang, J. Vac. Sci. Technol. B 18 (2000) 3010.
[29] T.H.P.H.P. Chang, M. Mankos, K.Y. Lee, L.P. Muray, Microelectron. Eng. 57 (2001) 117.
[30] J. Orloff, ed., Handbook of Charged Particle Optics, 2nd Edition, Edited by J. Orloff, 2nd ed., CRC Press, 2009.
[31] G.H. Jansen, J. Vac. Sci. Technol. B 298 (1988) 1977.
[32] G.H. Jansen, I. Introduction, J. Appl. Phys. 84 (1998).
[33] M. Mankos, a. Sagle, S.T. Coyle, A. Fernandez, J. Vac. Sci. Technol. B 19 (2001) 2566.
[34] M. Mankos, L.H. Veneklasen, R. Garcia, H. Pearce-Percy, J. Vac. Sci. Technol. B 16 (1998) 3206.
[35] L. Han, M.A. McCord, G.I. Winograd, R.F.W. Pease, J. Vac. Sci. Technol. B 16 (1998) 3215.
[36] M.-S. Su, K.-Y. Tsai, Y.-C. Lu, Y.-H. Kuo, T.-H. Pei, J.-Y. Yen, Proc. SPIE 7637 (2010) 76371Q.
[37] B.J. Lin, Microelectron. Eng. 86 (2009) 442.
[38] M.J. Wieland, G. de Boer, G.F. ten Berge, M. van Kervinck, R. Jager, J.J.M. Peijster, E. Slot, S.W.H.K. Steenbrink, T.F. Teepen, B.J. Kampherbeek, Proc. SPIE 7637 (2010) 76370F.
[39] G. De Boer, M.P. Dansberg, R. Jager, J.J.M. Peijster, E. Slot, S.W.H.K. Steenbrink, M.J. Wieland, Proc. SPIE 8680 (2013) 1.
[40] E. Slot, M.J. Wieland, G. de Boer, P. Kruit, G.F. ten Berge, a. M.C. Houkes, R. Jager, T. van de Peut, J.J.M. Peijster, S.W.H.K. Steenbrink, T.F. Teepen, a. H. V. van Veen, B.J. Kampherbeek, SPIE Lithogr. 6921 (2008) 69211P.
[41] I. Servin, N.A. Thiam, P. Pimenta-Barros, M.-L. Pourteau, A.-P. Mebiene, J. Jussot, J. Pradelles, P. Essomba, L. Lattard, P. Brandt, M. Wieland, 9423 (2015) 94231C.
[42] P. Kruit, Microelectron. Eng. 84 (2007) 1027.
[43] R. Waser, Anoelectronics and Information Technology : Advanced Electronic Materials and Novel Devices, 2nd ed., Weinheim: Wiley-VCH, 2005.

Ch. 2 Electrostatic rotator for alignment purposes in multi electron beam systems

Authors: A.C. Zonnevylle, C.Th.H. Heerkens, P.Kruit, M.L. Wieland, F.M. Postma and S.W.K.H. Steenbrink

This chapter has been published in: A.C. Zonnevylle et al., *Microelectronic Engineering 87 (2010) 1095–1099*

Abstract

In single charged particle beam column the alignment is obtained either by mechanical shift of the lenses or by XY alignment deflectors. The problem in multi beam array systems is that it is only possible to deflect the array of beams in the XY direction and not able to correct for a possible rotation errors between arrays blocks. A new concept is presented here that can electro statically align multi beam array systems.

Introduction

Optical mask based lithography has been the workhorse of the semi conductor industry for almost 50 years. In order to keep up with Moore's law lithography tools are, in every generation, on the cutting edge of mans technology. To reach lower resolutions people are designing EUV (Extreme ultraviolet) systems. However there are increasingly concerns about EUV, due to its estimated high operational cost [1].

An alternative is the use of electron beam based maskless technology, which has several advantages over mask-based technology, especially in prototyping and small series productions. A high throughput maskless lithography machine based on MEMS multi electron beam technology is currently being developed by MAPPER bv [2]. These machines consist of more than 10 000 individual electron beams, focused, blanked and deflected by MEMS elements [3]. The first generation MAPPER litho tool is expected to step in at the 22nm node.
The electron lenses in these machines consists of several arrays of electrodes that have to be aligned with sub 500 nm precisions.

However, the alignment of the lens arrays (block of array electrodes and spacers) in the column is not as straightforward as in the case of a single electron beam system, where it is achieved either by mechanical shift of the lenses or by using electrostatic beam alignment deflectors. The problem in multibeam systems is that it is only possible to deflect the array of beams in the XY direction and not to correct for a possible rotation

error between lens arrays. This alignment problem is visualized in figure 1. A rotation error results in a rotational shift for the outermost lenses of the array.

Mechanical rotation alignment of the lens arrays with piezo-stages is possible, but has disadvantages (space occupation, cables, drift, stray electric fields etc.), so we are investigating an alternative. By making use the off axis properties of an electrostatic lens in combination with variable lens strength we show that we can create a tunable image rotation while keeping the focal distance (z-direction) unaltered.

First we shall discuss with a single shift lens how to obtain a variable XY position shift, before explaining our solution for the rotation error. Finally we will discuss the fabrication of the device.

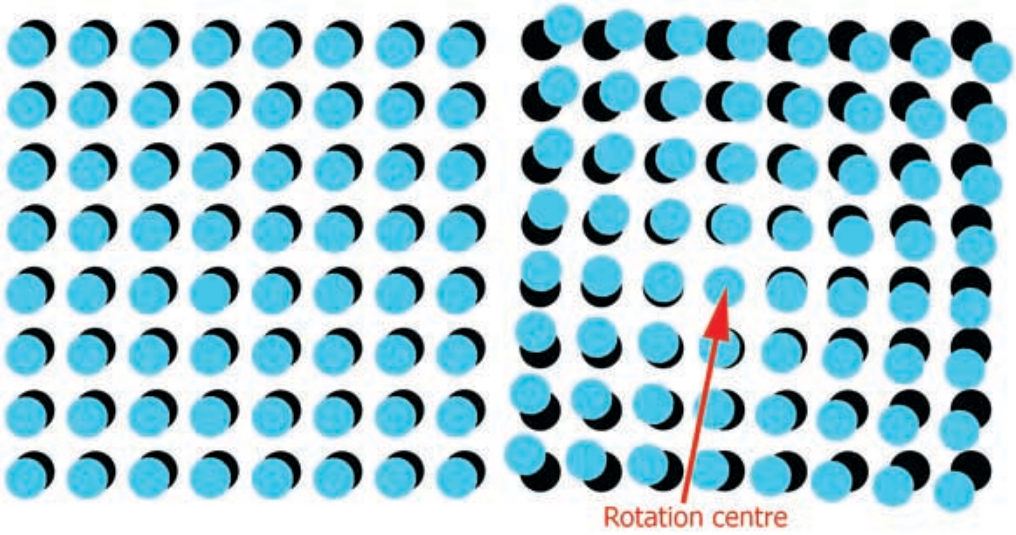

Figure 1: Left: alignment error solvable with XY deflectors. Right: Rotation error where XY deflectors are not enough for alignment.

Theory and Simulations

In an electron optical system there are several possibilities to steer the beam through the column. Until now only electrostatic or magnetic deflectors have been used. We give an alternative by using the off-axis lens properties in an electro static lens. Figure 2 explains the geometric principle. By changing the incident height $\mathbf{h_o}$ the focal position will shift perpendicular to the optical axis by an amount $\mathbf{h_i}$ which depends on $\mathbf{h_o}$ and the lens strength **a**. If the lens becomes stronger, **hi** becomes greater. A drawback of a single symmetric lens is that the focal position shifts along the z-axis when the lens strength **a** is changed [4].

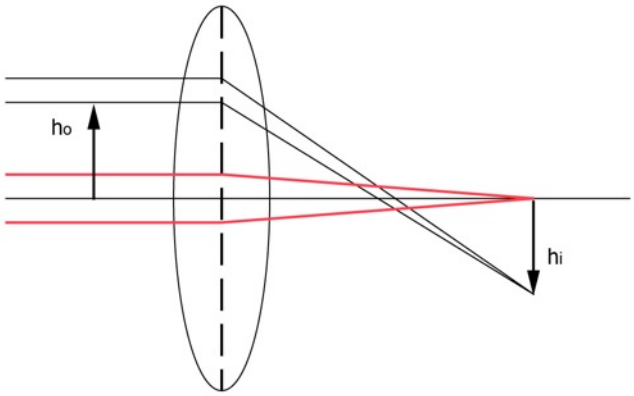

Figure 2: In red on axis beam, in black off axis beam. It can be seen that the focal position of the off axis beam is being shifted perpendicular to the optical axis.

The change in focal distance (z-direction) can be compensated by using a 5 element electrostatic lens [5] (shown in figure 3). In this lens the focal position can be shifted in the XY plane in correspondence with the electrode shift and applied voltage between el2, el3 and el4. The focal position (z-direction) and kinetic energy can be maintained by changing the voltage on electrodes el2 and el4. The situation is shown in figure 3, with potential lines and a ray trace, to visualize the effect.

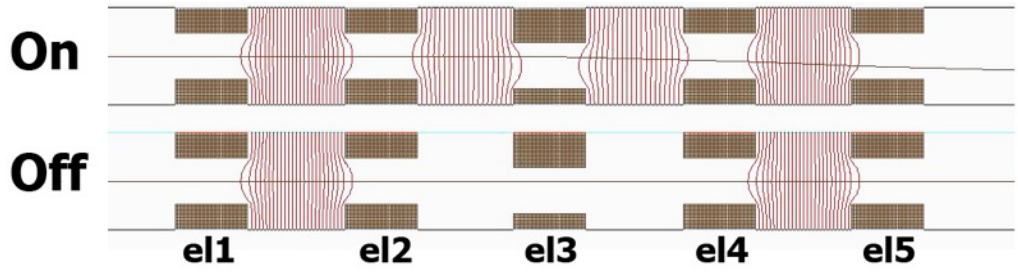

Figure 3: Ray trace simulation of a 5-element shift lens in two states. Down: off state, el3 has same potential as el2 and el4, beam passes straight. Up: on state el3 has a different potential from el2 and el4, the beam is deflected in the direction of the lens shift. The Lens hole diameter is 100 µm, the thickness of the electrodes is 150 µm and the spacing is 200 µm.

When small voltage changes are applied on electrode el3 with respect to its neighbors a linear shift of the focal point position in the XY-plane is seen with negligible focal distance shift in the z-direction. The shift depends on the original mechanical shift of electrode 3.

This is shown in figure 4 for different lens shifts and electrode 3 potentials. These results are from simulations in Simion 3D [6]. Data recording is done in the optical axis direction in steps of 2 µm, no focal distance shift in the z-direction and no astigmatism is found even without adjusting the voltage on el2 and el4.

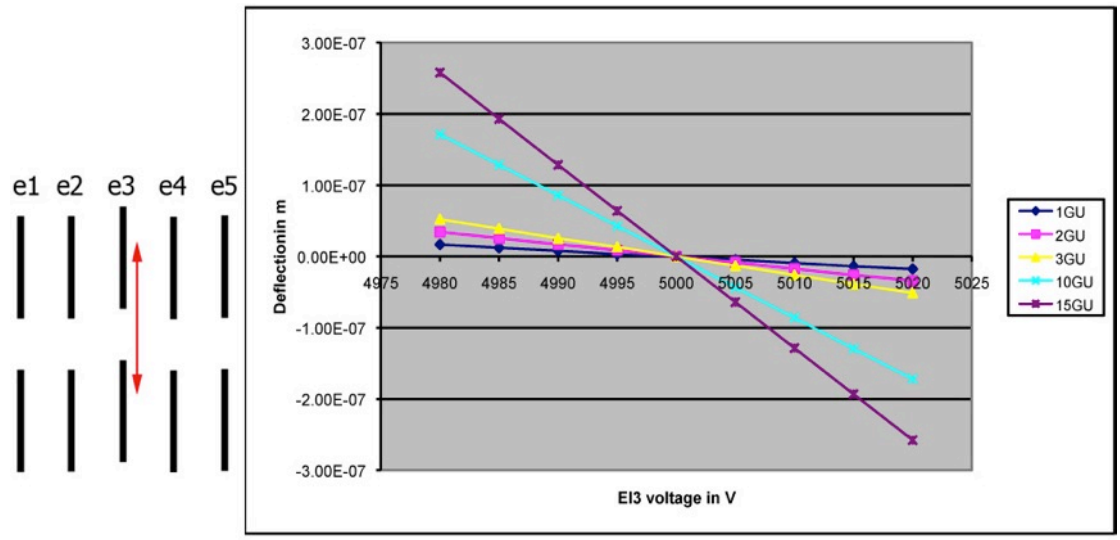

Figure 4: Left: 5 element shift lens configuration. Lens diameter is 100 µm, electrode thickness is 150 µm and spacing is 200 µm. Right: Plotted y shift in focal position (with f= 1.73 mm) versus applied voltage e3, for various shifts of electrode 3 in the y direction. Voltage e1 and e5 = 0V and e2 and e4 = 5kV. 1 GU stands for 2 µm shift.

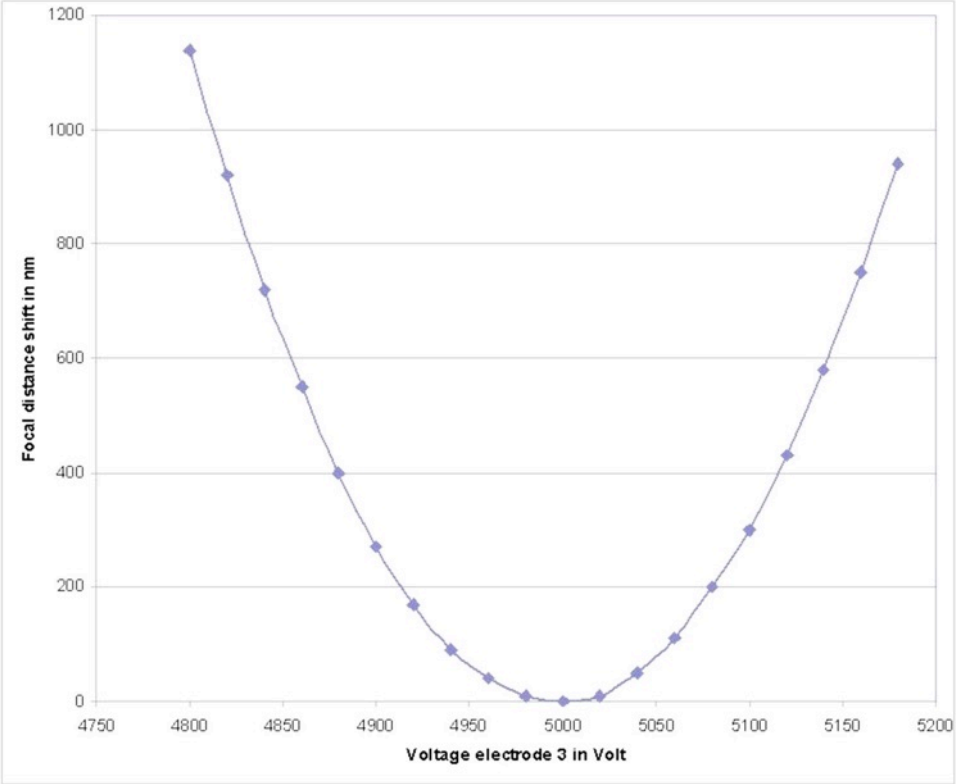

Figure 5: Vertical: Z shift in focal distance in nm. Horizontal: applied voltage on electrode 3. El1 = el5 = 0V and el2 = el4 = 5kV.

More detailed studies on the focal position shift in the z-direction caused by the potential variation of electrode 3 are done in EOD (Electron Optical Design simulations) [7] for a rotational symmetric configuration. These results are shown in figure 5. To correct a typical misalignment in our case the correction range will not exceed +/- 20 Volt, so the focal distance change in the z-direction is negligible.

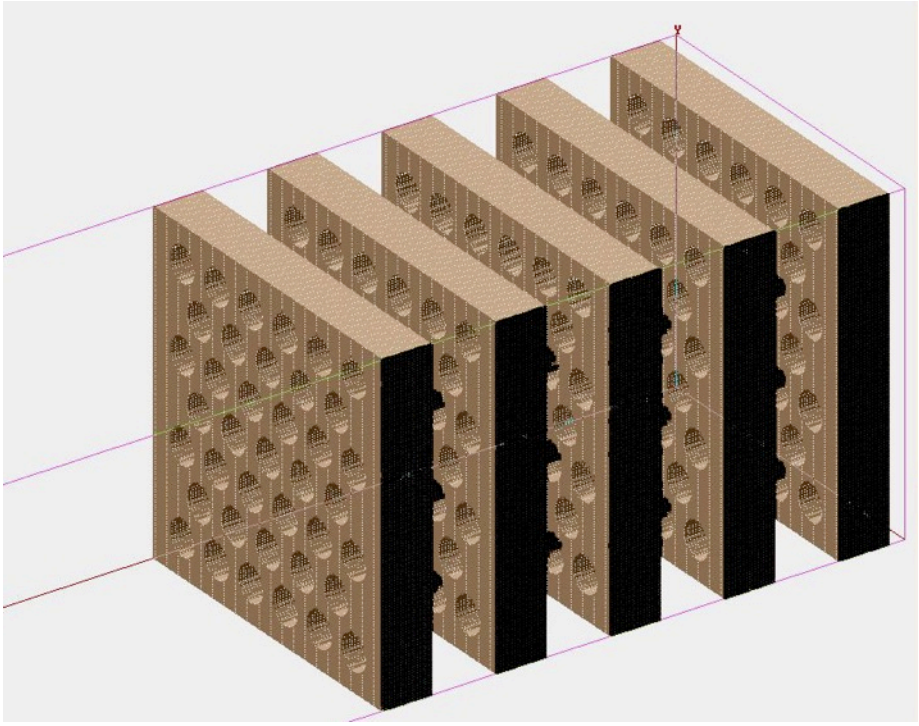

Figure 6: 3D picture of 5 element mems lens array stack. Thickness of the electrodes is 150 µm, the spacing is 200 µm and the pitch between the beams is 150 µm.

Further studies are necessary to characterize the aberrations that will ultimately limit the practical limits of the shift that can be obtained with this method.

The seen linear behavior between mechanical shift and beam position shift in the XY plane is an essential property for our rotation corrector to be able to create a tangential shifts in an multi beam array system.
Our suggested multi beam rotation solution is build up as followed.
In a 5 electrode lens array the middle array electrode is rotated along the array rotation center. This gives an individual lens shift per beam let that is proportional to the distance from the system center. The principle geometry is shown in figure 6.

Thus, it is now possible to correct for rotation misalignment by applying a voltage on the middle electrode. In figure 7 an extreme correction rotation is shown with our simulation model to show that there is tangential beam shift. In red dots rotation correction **on** versus **off** by the blue dots.

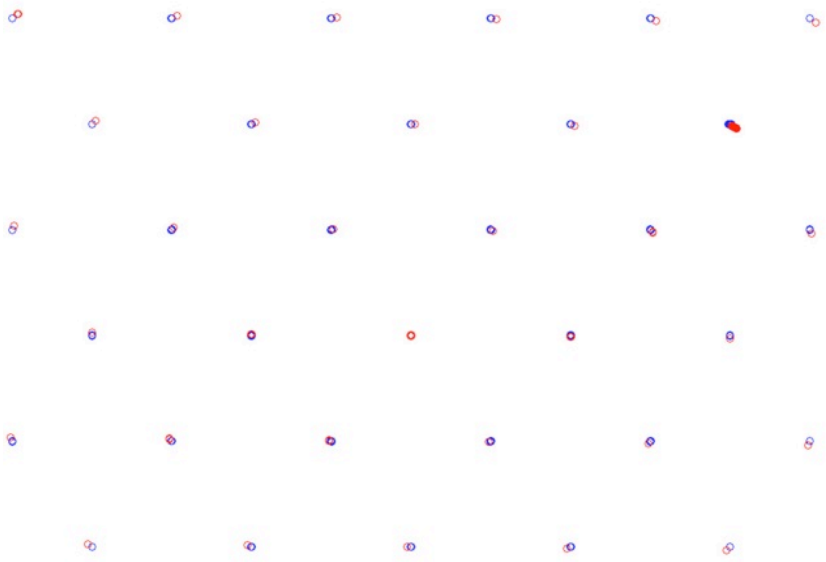

Figure7: Blue dots: rotator off (e3 is on the same potential as e2 and e5), red dots: rotator on. Rotation is around the middle beam let. Results from simulation in Simion 3D.

Fabrication

The RZ-deflector consists of a stack of five conducting electrodes separated by non-conducting spacers.
The electrodes all have an array of lens holes. The middle electrode is rotated around the central lens hole by a small angle.
The starting material for the electrodes is a thin double side polished 4" silicon wafer (#1 in figure 8) that is then covered with a silicon dioxide layer by thermal oxidation (#2 in figure 8). The pattern of the lens holes is defined by optical lithography (#3 in figure 8) and this pattern is transferred to the oxide layer by reactive ion etching (#4 in figure 8). Then the lens holes are etched through the electrode using the oxide as an etch mask in a Bosch DRIE process. (#5 in figure 8). After etching, the electrodes are cleaned using a combination of wet and dry processes and coated by sputter deposition.

The starting material for the non-conducting spacers is a thin double side polished 4" glass wafer that is diced to the required size (#6 in figure 8). Mechanical drilling makes the central hole. (#7 in figure 8). Finally the spacers are cleaned using a combination of wet and dry processes.

Since the alignment of the electrodes in the stack is crucial for the functioning of the device a dedicated add-on was developed for a Karl Suzz mask aligner allowing for accurate positioning of the electrodes during the stacking sequence.

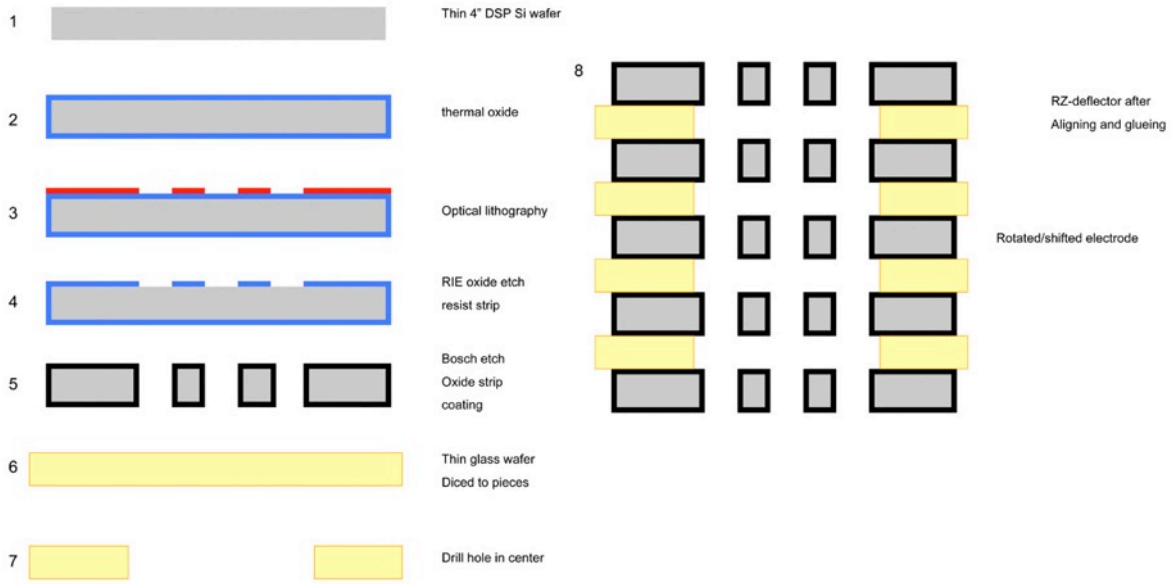

Figure 8: Processing steps

Although the individual lens electrodes and spacers have successfully been manufactured, the alignment procedure is still problematic. Mechanical alignment and electrical connection of the 5 electrodes has not been successful yet using the mask aligner. The optics need to be upgraded to have a higher resolving power with longer working distance or we need to adapt the electrodes and spacers to fit in a dedicated alignment tool as used by MAPPER Lithography bv.

Conclusion and outlook

In this paper we have shown a method that rotation misalignments can be solved with a special five-electrode array electrostatic lens. We have shown the working of the apparatus by discussing a single beam let and lens array version. In the five electrode electrostatic lens we have shown that XY beam shifts can be induced without changing the focal distance in optical axis z-direction. The fabrication method of such a device has been described. The fabrication of all the electrodes and spacers has been accomplished, but the modified mask aligner needs additional modifications or we need to use a different tool to successfully stack and connect our five-electrode rotation aligner. Further work will concentrate on manufacturing issues and proof of concept experiments

Acknowledgements
We would like to thank MAPPER Lithography bv for facilitating this research. DIMES and **the Kavli Institute of Nanoscience Delft** for the use of their facilities.

References

[1] B.J. Lin, Microelectron. Eng. 86 (2009) 442

[2] M.J. Wieland, G. de Boer, G.F. ten Berge, M. van Kervinck, R. Jager, J.J.M. Peijster, E. Slot, S.W.H.K. Steenbrink, T.F. Teepen, B.J. Kampherbeek, Proc. SPIE 7637 (2010) 76370F.

[3] P. Kruit, Microelectron. Eng. 84 (2007) 1027.

[4] E. Hecht, Optics 4th Edition, 2001.

[5] J. Orloff, ed., Handbook of Charged Particle Optics, 2nd Edition, Edited by J. Orloff, 2nd ed., CRC Press, 2009.

[6] Simion 3D v.8.0, Scientific Instrument Services

[7] B. Lencová, J. Zlámal, Phys. Procedia 1 (2008) 315.

Ch. 3 Deflection properties of an electrostatic electron lens with a shifted electrode

Authors: A.C. Zonnevylle, T.Verduin, I. Lazić, C.W. Hagen and P.Kruit

This chapter has been the basis for the publication: A.C. Zonnevylle et al. J. Vac. Sci. Technol. B 31(6), Nov/Dec 2013

Abstract

In this chapter we discuss a new electron optical component: an electrostatic lens in which one electrode is intentionally shifted laterally, breaking the rotational symmetry. This lens is called a 'shift lens'. Usually, a shifted electrode is undesired and the resulting aberrations are calculated only for the purpose of setting manufacturing requirements. However, the shift lens can be applied as a deflector. Thus, in multi beam systems with an individual micro-lens for each beam, all beams can be deflected with a single voltage. By giving a different shift to each lens, the deflection can be different for each beam. This allows the creation of a multi beam rotation error corrector. The optical properties of an electrostatic 5-electrode lens with a shifted middle electrode are analyzed in this paper. For describing the optical properties of the shift lens, a simple mirror symmetric model in combination with Taylor polynomials is used. This model is then verified with a newly developed ray-tracing program, and the obtained aberrations are discussed. The middle electrode is shifted over a range of 1% up to 20% of the diameter of the lens. We have found dependences of deflection, defocus, astigmatism and second order on shift distance and excitation. We expect the shift lens to be a useful new optical component, especially in multi beam systems.

Introduction

Electrostatic electron lenses usually consist of several rotationally symmetric electrodes at different potentials. Deviations from rotational symmetry, whether caused by unroundness of the electrodes or by misalignments between the electrodes, usually cause undesired beam aberrations and are avoided as much as possible. In some situations, of course, non-rotational symmetry is created on purpose in order to create deflection, stigmation [1] or other multi-pole effects. To create multi-pole effects, the construction usually contains multiple electrodes around the optical axis of the system; various examples can be found for example in Hawkes and Kasper[2].

A new concept, proposed by Zonnevylle et al. [3], intentionally breaks the rotational symmetry of an electrostatic lens into a mirror symmetric configuration. The proposed lens is set up with five electrodes. The middle electrode is translated in the lateral direction. This is what we call a 'shift lens'. This shift lens moves the focused electron beam in the same lateral direction as the shifted electrode. Applying a voltage difference between the shifted middle electrode and the non-shifted neighbor electrodes displaces the focused electron beam. This configuration could be implemented for

alignment purposes in a multi-beam system[4]. This kind of beam alignment is not preferred for a single beam system, because beam deflectors are much more suited and well understood.

Implementing this idea in a microfabricated multi beam system should enable the correction of rotation misalignment in a multi-beam MEMS system by adjusting the voltage on its middle array electrode, as described by Zonnevylle et al.[3]. We remark that in a multi-beam system such as for example the MAPPER[4] machine, each beamlet column can be modeled as an individual system. In Figure 1 we illustrate the lateral shift for each individual lens in a multi beam array lens. The amount of lateral shift is a tangential function with respect to the center of the array, making it possible to correct array rotation errors.

In this paper we will propose a model for describing the induced aberrations of the shift lens. We apply the model to a MEMS lens with characteristic dimensions that are typical for a micro fabricated multi beam system. However, the conclusions should be similar for macroscopic lenses with shifted electrodes. The model is investigated with a new three-dimensional simulation program that was developed for this study.

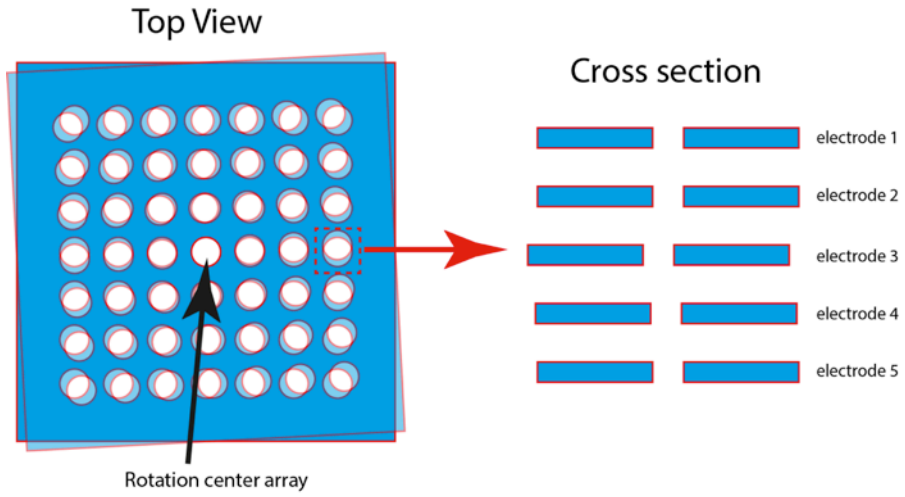

Figure 1: Top view of five stacked 7x7 array electrodes, with the middle array electrode rotated around the rotation center. The cross section view shows the lens build up for the red dashed square marked beamlet.

Modeling

To the best of our knowledge, there are no experimental or theoretical studies on a similar proposed shift lens. However, introductions to non-rotational systems can be found in literature, for example in chapter 23 of Hawkes and Kasper [2] and in Whitmer et al. [5].

Consider an arbitrary optical system without any symmetry in the geometric approximation. A ray approaches an optical component at a distance *x,y* from the *z*-axis. We concentrate the action of the optical component in a single plane perpendicular to the *z*-axis. If the optical component is a lens, this is called the "thin lens approximation". For an electron that travels approximately parallel to the z-axis, the change in angle between the ray and the z-axis can be expressed in two Taylor expansions for both angles in *x* and *y*. These Taylor expansions for an arbitrary system are given in Eqs.(1)-(2).

$$\alpha_x = \sum_{i=0}^{\infty}\sum_{j=0}^{\infty} a_{ij} x^i y^j \qquad (1)$$

$$\alpha_y = \sum_{i=0}^{\infty}\sum_{j=0}^{\infty} b_{ij} x^i y^j \qquad (2)$$

At first, we will show that for rotationally symmetric systems the given expansions reduce to well known expressions, as can be found for example in the books of Hecht[6] and Thong[7]. Then, the same approach is used to derive the expressions for the shift lens that is mirror symmetric. We have limited the expansions up to the 3rd order, since that is considered sufficient [7,8] for most electron optical systems.

Derivation of the general equations for a rotationally symmetric system

The rotational symmetry of the system is identified through the following expressions for the change in angle (see figure 2a):

$$\alpha_x(-x,y) = -\alpha_x(x,y) \Rightarrow \alpha_x(-x,y) + \alpha_x(x,y) = 0 \qquad (3)$$

$$\alpha_y(x,-y) = -\alpha_y(x,y) \Rightarrow \alpha_y(x,-y) + \alpha_y(x,y) = 0 \qquad (4)$$

Equations (5)-(6) follow from applying the symmetry expressions to the Taylor expansions (Eqs. (1)-(2)) keeping the terms up to the 3rd order.

$$\alpha_x = (a_x + a_{xy^2} y^2)x + a_{x^3} x^3 \qquad (5)$$

$$\alpha_y = (b_y + b_{x^2y} x^2)y + b_{y^3} y^3 \qquad (6)$$

Additionally, we must have $\alpha_x(\phi,0)=\alpha_y(0,\phi)$ for every ϕ, giving $a_x=b_y$ and $a_{x^3}=b_{x^2y}=a_{xy^2}=b_{y^3}$.

Finally, this gives:

$$|\alpha|=\sqrt{\alpha_x^2+\alpha_y^2}=a_1\sqrt{x^2+y^2}+a_3\left(\sqrt{x^2+y^2}\right)^3=a_1h+a_3h^3 \qquad (7)$$

Which is the textbook [6–8] equation for a rotational symmetric optical system, where the deflection strength α depends on a_1 and a_3 that represent respectively the first order and third order strengths as function of the distance h from the optical axis.

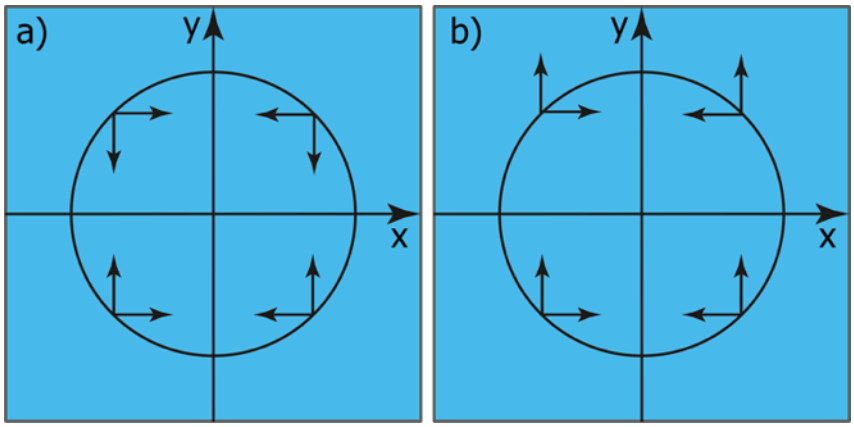

Figure 2: The change of angle split up in the x and y components for a rotationally symmetric geometry (a) and a mirror symmetric geometry (b) the latter corresponds with the proposed shift lens.

Derivation of the general equations for a mirror symmetric system

The displacement of the middle electrode breaks the rotational symmetry of the system. However, mirror symmetry remains because the displacement is only in one lateral direction.

We will now assume that the middle electrode is shifted in the *y* direction. Therefore, the mirror symmetry is with respect to the plane x=0. We will use the same analysis as for the rotationally symmetric system. The only exception is that the symmetry conditions (see figure 2b) are now given by equations (8) (9).

$$\alpha_x(-x,y)=-\alpha_x(x,y)\Rightarrow\alpha_x(-x,y)+\alpha_x(x,y)=0 \qquad (8)$$

$$\alpha_y(-x,y)=\alpha_y(x,y)\Rightarrow\alpha_y(-x,y)-\alpha_y(x,y)=0 \qquad (9)$$

The change in angle for the mirror symmetric system is now given in equations (10) (11).

$$\alpha_x = (a_x + a_{xy}y + a_{xy^2}y^2)x + a_{x^3}x^3 \qquad (10)$$

$$\alpha_y = b_0 + b_{x^2}x^2 + (b_y + b_{x^2y}x^2)y + b_{y^2}y^2 + b_{y^3}y^3 \qquad (11)$$

Simulation program CCPO

In the 1950's Sturrock [9] conducted theoretical studies on the aberrations induced by small misalignments using a first order perturbative method on rotationally symmetric systems. This is known in the field of electron optics as Sturrock's method. This proposed model by Sturrock is valid as long as the perturbation is small, giving only a first order approximation of the perturbed system with respect to the rotationally symmetric system. This method has been implemented in special versions of the simulation programs developed by Munro[10] and Zlámal[11] for the purpose of tolerance calculations. In standard rotationally symmetric systems these tolerances are the shifts and tilts caused by machine tolerances and fabrication inaccuracies. In practice, the first order approximation proposed by Sturrock is sufficient, because these shifts and tilts are generally less than, or in the order of one percent of the diameter of the aperture of the modeled lenses. In the case of the proposed shift lens, the displacement of the middle electrode can be much larger. Therefore, our shift lens cannot be studied using only a first order perturbation method. Thus, a full three-dimensional simulation program is required. Unfortunately, the commercially available programs are not accurate enough and/or just take too long for investigating the proposed system for different shifts. Because of this, we developed our own three dimensional simulation program CCPO (Computational Charged Particle Optics). The simulator is based on the Boundary Element Method (BEM)[12]. The issue of computational time is addressed by utilizing the (massively) vectorized parallelism of modern graphics cards (GPGPU) (General-Purpose computing on Graphics Processing Units). Actually, this three-dimensional version is an upgrade of the simulator used by Verduin et al. [13] who has calculated the Coulomb interactions in a field emission gun. In our case, we have not included the Coulomb interactions between the simulated electrons. The central idea of the Boundary Element Method is simple: determine the surface charges on a boundary of electrodes such that the electrodes have the desired potential. The calculation process for the three-dimensional simulation presented in this article is depicted in the top part of figure 3.

The surface charges on the boundaries are passed on to another sub-program that takes care of non-relativistic ray-tracing of particles through the system of electrodes. Each simulated charged particle follows the loop depicted in the lower part of figure 3 until a predetermined destination is reached.

The implementation of the ray-tracer on General-Purpose Graphics Processing Units (GPGPU) reduces the computational time per trace considerably. Further reduction in computational time is obtained by using single precision arithmetic, which can be chosen before each ray trace run. This reduction, however, depends on the type of GPU and limits the accuracy to approximately 6 digits. We have checked if this is

sufficiently accurate by also running some simulations in double precision. In every case, the surface charges of the boundary elements were always computed using double precision arithmetic. We have implemented Kahan's compensated summation algorithm [14] in order to avoid truncation and accumulation errors to become significant.

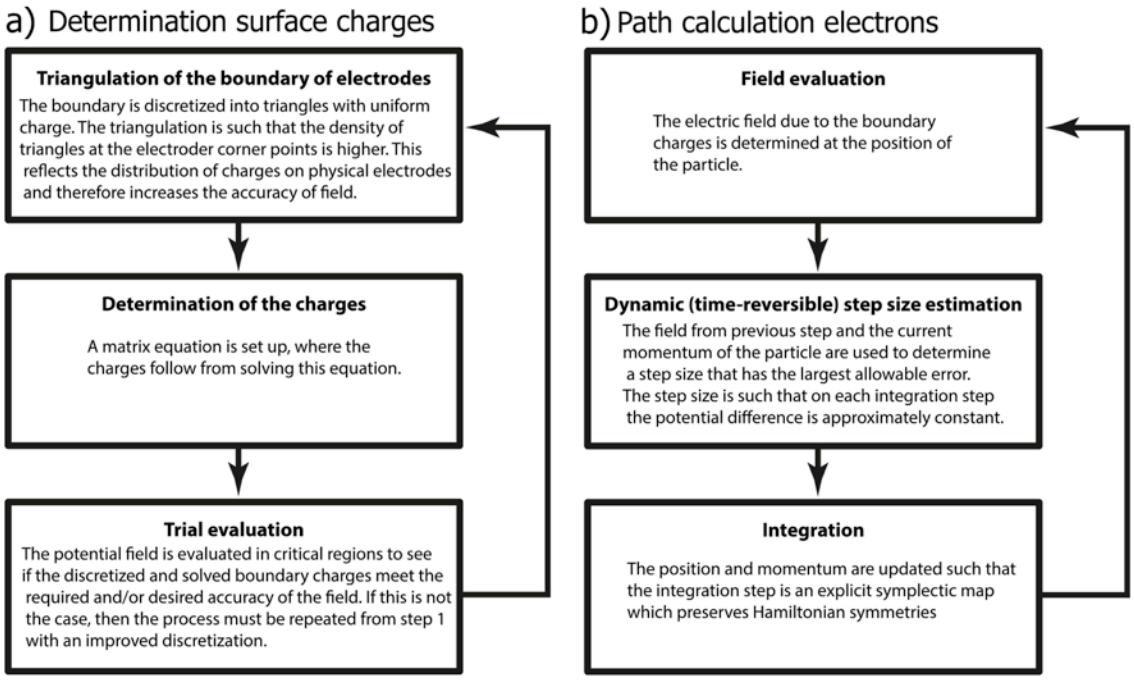

Figure 3: Computation diagrams: of the determination of the surface charges (a) and the paths of the electrons (b).

Simulation setup

Figure 4 shows the geometry of the system as implemented in the CCPO simulator; the total geometry is discretized into 16820 triangles. The triangles are not divided evenly but are concentrated on the lens electrodes near the apertures in the electrodes. The outside of the shift lens is connected to a surrounding shield, which has the same potential as electrode 1 and 5. The potentials on electrodes 2 and 4 are +5kV and are not changed in our simulation. Electrode number 3 is the displaced electrode that is shifted from 0-20 µm in seven steps. The potential of the middle electrode is varied from 2kV-8kV in steps of approximately 100 V. The total number of simulations is 350. Due to the changes in geometry and potentials, the field solution is recalculated for every simulation. We allowed the potential difference between the middle electrode and its neighbors to vary more than described by Zonnevylle et al.[3], where the potential only varies from 4980-5020 Volt. Here, we did not want to limit the setup to that particular case.

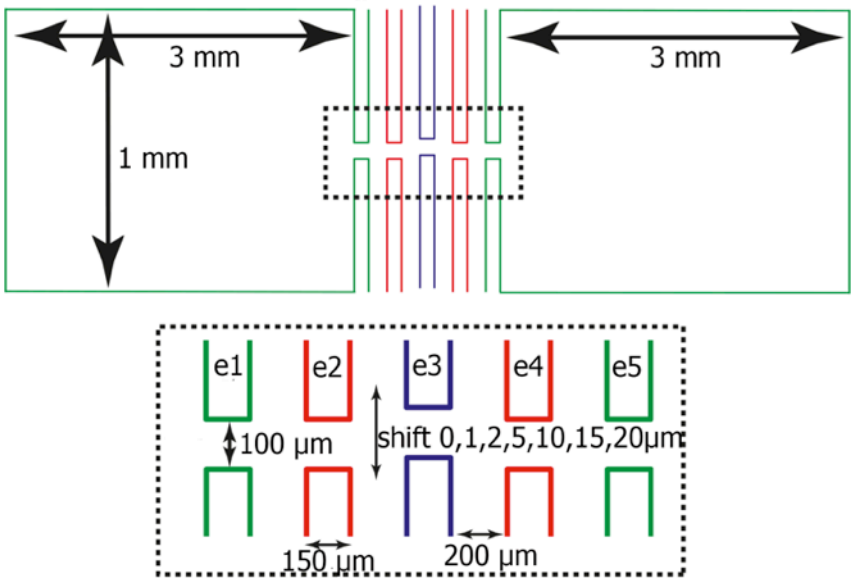

Figure 4: Simulation geometry used in the CCPO simulator for the study of the shift lens. Note dimensions are not equally scaled.

Therefore we have extended the deflection range significantly in order to find the limits of practical use for the shift lens. The electrons are uniformly distributed in a circular beam with radius of 5 µm, starting at z=-2 mm in a field free zone, centered at x=0 and y=0. The electrons travel parallel to the optical axis with a kinetic energy of 5 keV. Since all initial angles are zero, we use the angles found in the measurement plane at z = 2.5mm, which is located in a field free region, for our Taylor expansion. The coefficients for the Taylor expansion up to 3rd order are determined using the standard

surface-fitting algorithm of the curve fit toolbox of Matlab[15]. This process is repeated for every shift and potential of the middle electrode.

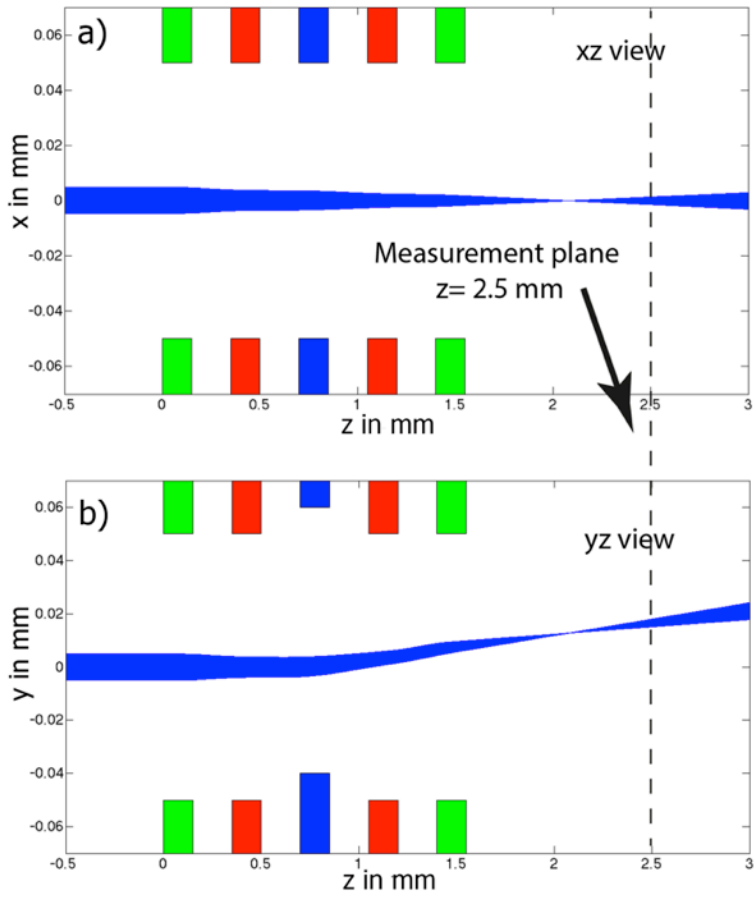

Figure 5: Ray trace plot of the simulated electrons, whereby the potential on electrode 3 is set to 2kV representing a decelerating lens, visualizing the shift action in the yz-view (a) and the symmetric behavior in the xz-view (b). Note x and y dimensions are not equally scaled with z dimension.

The total number of electrons per run is 1500. This number is based on the statistical error obtained from the post-trace analysis. In other words, the reduction on the statistical error by increasing the number of particles is negligible.

Results

Model verification

The ray tracing of the electrons through the shift lens is illustrated in figure 5. The different views of xz and yz planes clearly show the mirror symmetric behavior. The coefficients of the Taylor expansion up to the 3rd order are shown in figure 6. All coefficients labeled with green are found to be significant, all others have computation noise around zero with signal-to-noise levels that can be expected with the accuracy used for these particular simulations. We would like to note that the signal-to-noise level in the single floating-point arithmetic, even after Kahan enhancement[14] with compensated summation can be at most 10^6. The zero order coefficients have therefore the largest expected signal-to-noise ratio. Naturally, the higher order coefficients have smaller relative contributions and hence smaller signal-to-noise levels. The found signal-to-noise levels for first, second and third order coefficients are respectively 10^4, 10^3 and 10^2.

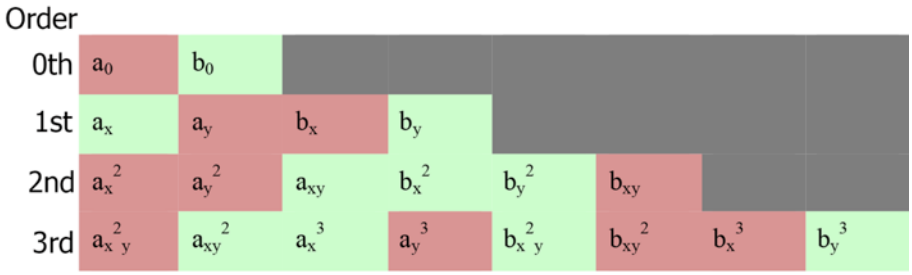

Figure 6: Coefficients of the Taylor expansions up to the 3rd order. The coefficients in the green boxes are found to be significant, red boxes are found to be negligible.

The found coefficients from the simulations support, within the error of the numerical calculations, the proposed mirror symmetric model for the shift lens as given in equations (10) (11).

Shift lens behavior, general trends

If the concept of a shift lens is implemented in a multi-beam rotation corrector, there is then a common z-plane for all beamlets. The most logical choice for a reference plane is the Gaussian image plane of the center beam, since this represents a non-shifted and rotationally symmetric lens.

Zero order effects

The zero order coefficient b_0 describes the intended deflection as a function of the potential difference of the middle electrode with respect to its neighbors (ΔV), which is shown in figure 7. We remark that the study by Zonnevylle et al.[3] concluded that the b_0 coefficient versus ΔV is linear. However, in this study (see Figure 7) we see that in a larger potential sweep the curves are no longer linear. Interestingly enough, the deflection is still a linear function of the lateral shift of the middle electrode, for all excitations. In other words, the zero order deflection angle for a 20 µm shift is always 20 times the zero order deflection of the 1 µm shifted electrode. For the multi beam rotation corrector this property is more important than the non-linearity with excitation voltage. This zero order deflection does not introduce any aberration to the beam, because there is no *x* and/or *y* dependence.

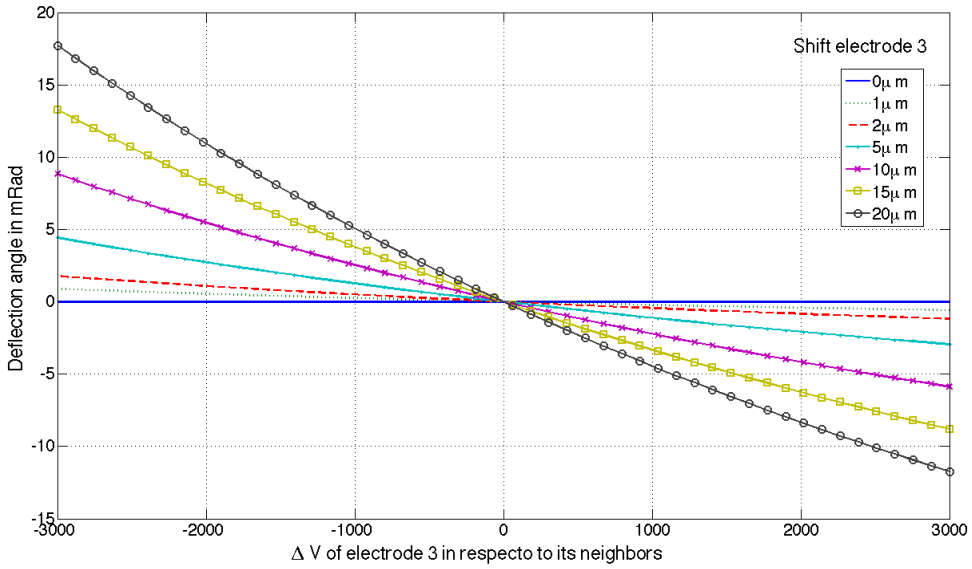

Figure 7: Zero order deflection strength in mRad versus ΔV in volts in respect to its neighbors for various lateral shifts values in µm of electrode 3.

First order effects

The first order coefficients a_x and b_y relate to the first order deflection in the *x* and *y* direction. In other words, these coefficients give the focal strengths in respectively the *x*

and y direction. The focal distance can be determined with $f_x = -\frac{1}{a_x}$ and $f_y = -\frac{1}{b_y}$. We have found that only for the non-shifted middle electrode (no shift) f_x and f_y are equal, as is expected for rotationally symmetric lens. For all other shift values of electrode 3 f_x and f_y are not equal. We expected this to happen for a mirror symmetric lens because of the aberration called astigmatism. The effect of astigmatism is plotted in figure 8 and 9 with $\Delta f = f_x - f_y$ on the vertical axis and ΔV or deflection in mRad, on the horizontal axis. We see that with increasing shift the astigmatism increases.

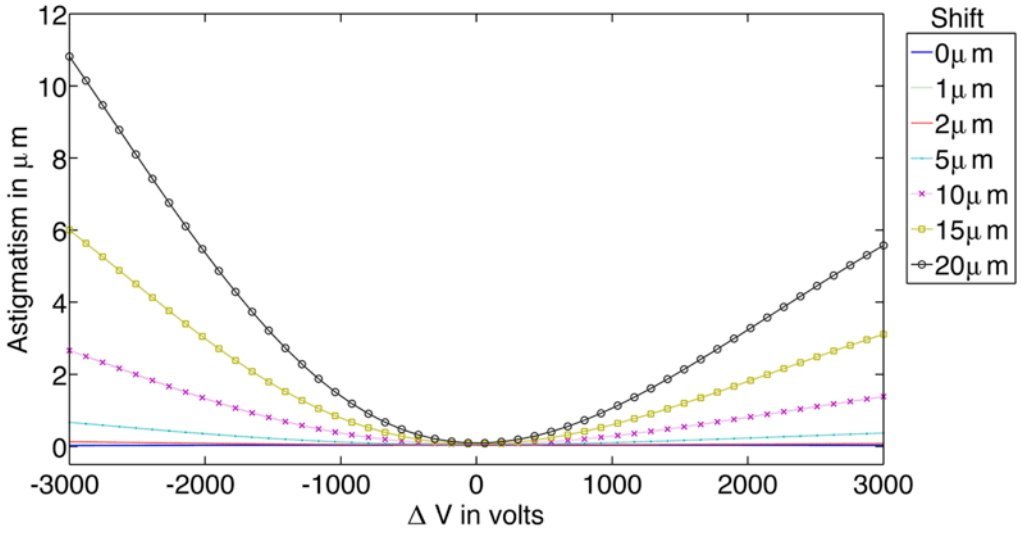

Figure 8: Astigmatism in μm versus ΔV in volts in respect to its neighbors for various shifts values in μm of electrode 3.

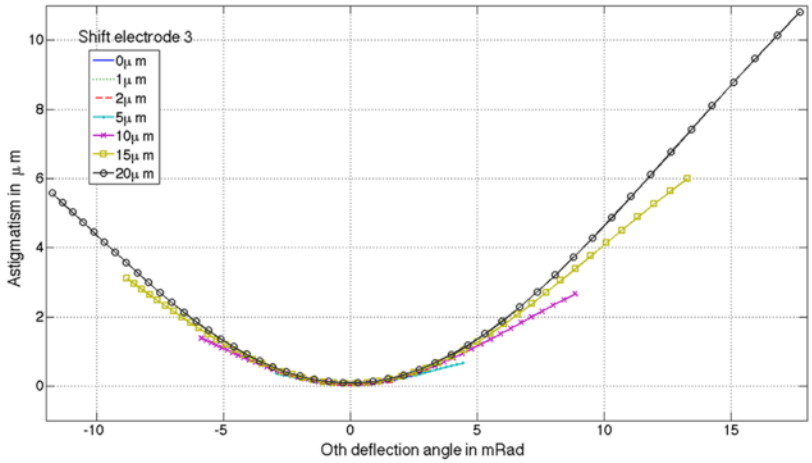

Figure 9: Astigmatism in μm versus deflection angle in mRad for various shifts values in μm of electrode 3.

The astigmatism caused by the different first order strengths will contribute to an enlargement of the beam at the reference focal plane. The numerical example in equation (12) gives an estimate for the contribution to the spot size at the reference z-plane. The largest contribution of astigmatism is approximately 11µm, this corresponds to f(-3000V) ≈1.45mm. In our simulations the largest starting value of x or y equals 5µm. This will give a maximum spot size contribution in the general focal plane of:

$$Astig_{contribution} = \frac{\max(x \vee y)}{f}\Delta f = \frac{5\mu m}{1.45mm}\cdot 11\mu m \approx 38nm \qquad (12)$$

Additionally we observed a less obvious first order effect, which can be ignored for a single beam system, but is important for a multi beam rotation corrector. We again use the center beamlet Gaussian image plane (the un-shifted lens) as a reference for all beamlets in the multi beam rotation corrector. If we compare the focal strengths in the same direction $\Delta f = f_{xvy}(shift) - f_{xvy}(0\mu m)$ for different shifts compared to no shift we see that there is a difference.

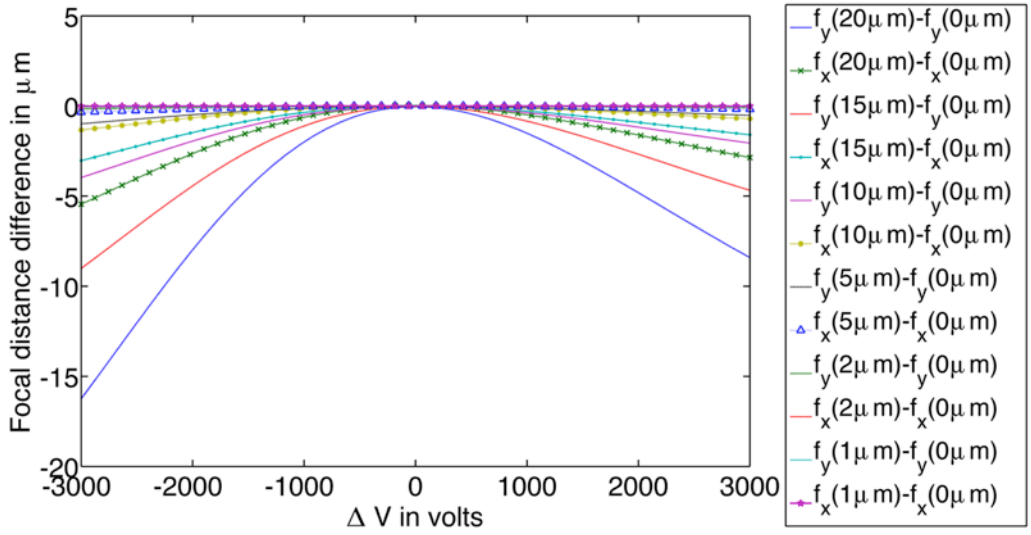

Figure 10: Focal distance difference in µm in same focal direction versus ΔV in volts in respect to its neighbors for various shifts values in µm of electrode 3. Plotted are seven different shift values in µm of electrode 3, for both fx and fy.

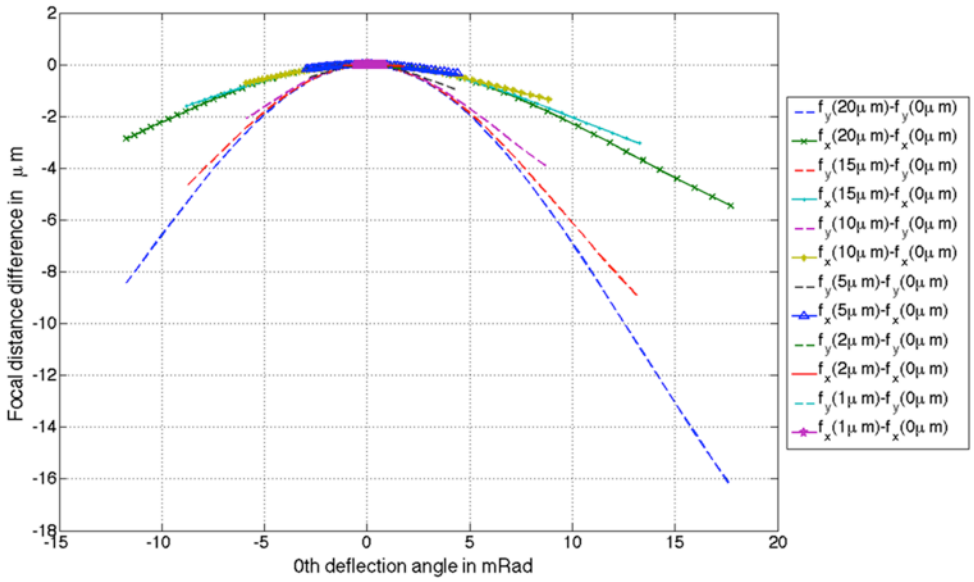

Figure 11: Focal distance difference in µm in same focal direction versus deflection angle in mRad for various shifts values in µm of electrode 3. Plotted are seven different shift values in µm of electrode 3, for both fx and fy.

Figure 10 and figure 11 shows the difference in focal shift (relative defocus) on the vertical axis versus ΔV or deflection angle, on the horizontal axis. We see an effect that is best described as a kind of "field curvature". The largest value for Δf is approximately 16µm, this corresponds to f (-3000V)≈ 1.45 mm. In our simulations the largest starting value of x or y equals 5µm, giving a maximum contribution to the spot in the general focal plane that is given in equation (13).

$$Curv_{contribution} = \frac{\max(x \vee y)}{f}\Delta f = \frac{5\mu m}{1.45mm}\cdot 16\mu m \approx 55nm \qquad (13)$$

We would like to note that in a multi-beam rotation corrector, this might be the most significant effect that needs to be taken into account.

Second order effects

The second order coefficients are plotted in figures 12-17. As expected, the second order coefficients in the direction of the shift have the largest overall value. The largest contribution is found in an accelerating lens at a value of ΔV= +3000 V.

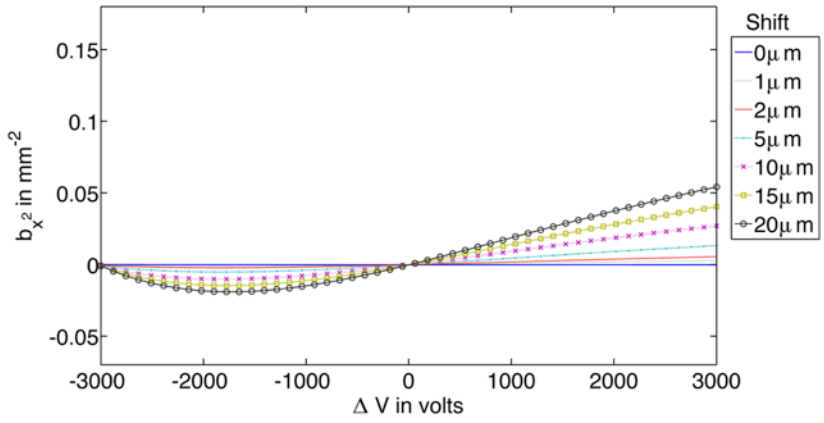

Figure 12: Second order b_x^2 coefficient in mm^{-2} versus ΔV in volts in respect to its neighbors for various shifts values in µm of electrode 3.

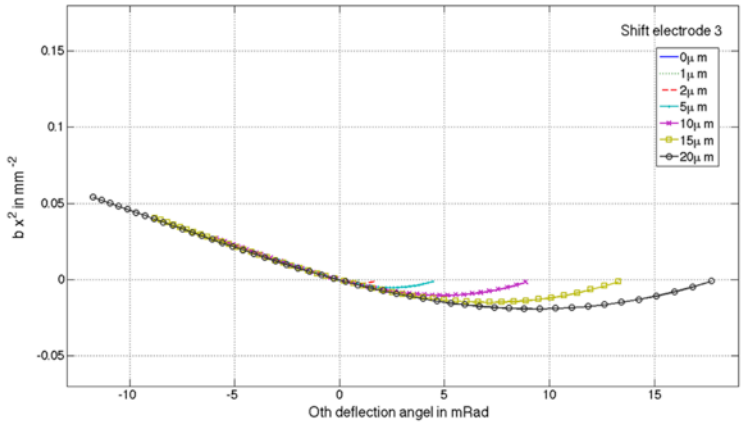

Figure 13: Second order b_x^2 coefficient in mm^{-2} versus deflection angle in mRad for various shifts values in µm of electrode 3.

We observe that the second order coefficients have a minimum negative value and then become positive again. This is best seen in figure 14.

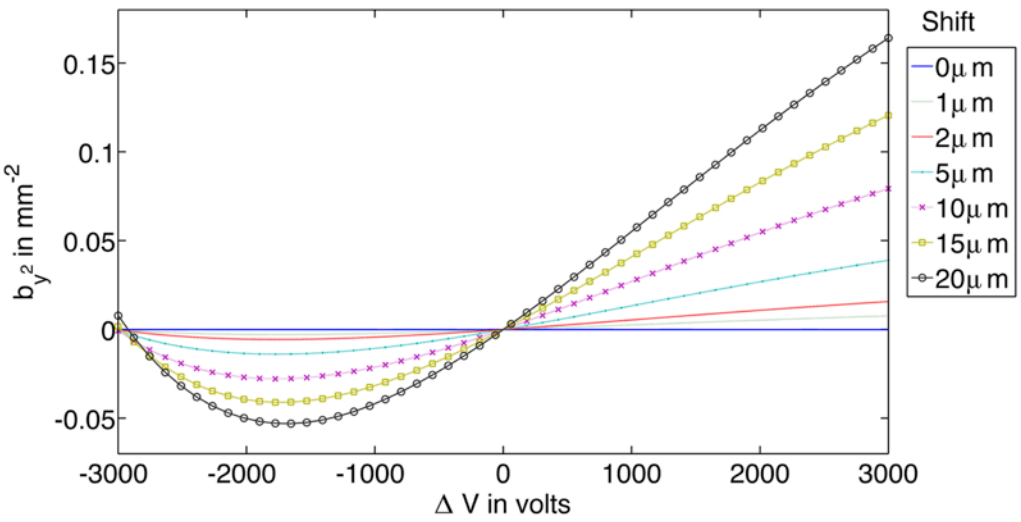

Figure 14: Second order b_y^2 coefficient in mm^{-2} versus ΔV in volts in respect to its neighbors for various shifts values in µm of electrode 3.

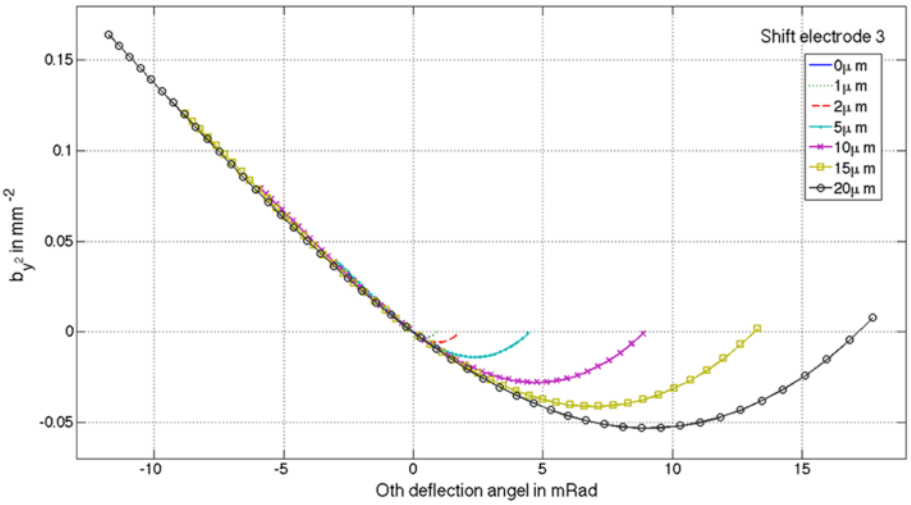

Figure 15: Second order b_y^2 coefficient in mm^{-2} versus deflection angle in mRad for various shifts values in µm of electrode 3.

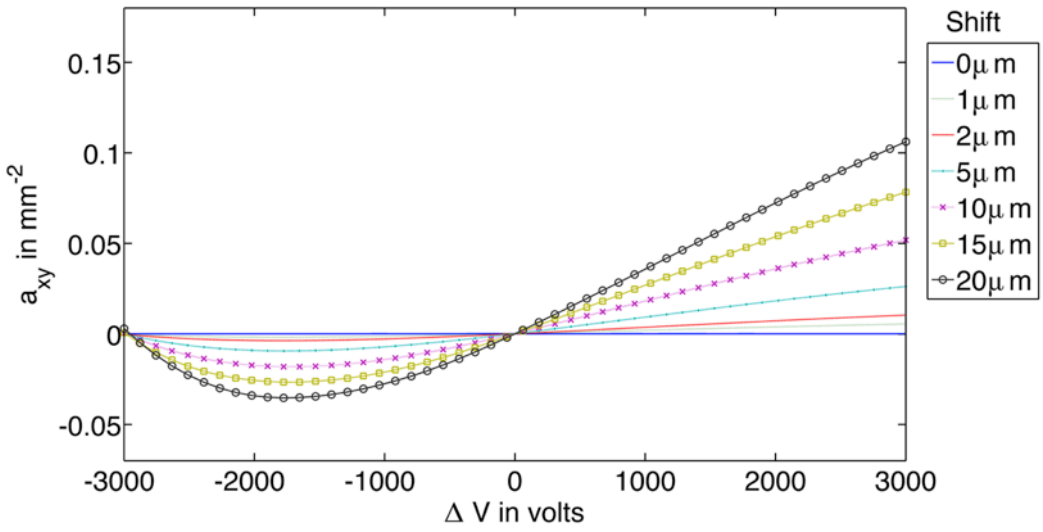

Figure 16: Second order a_{xy} coefficient in mm^{-2} versus ΔV in volts in respect to its neighbors for various shifts values in µm of electrode 3.

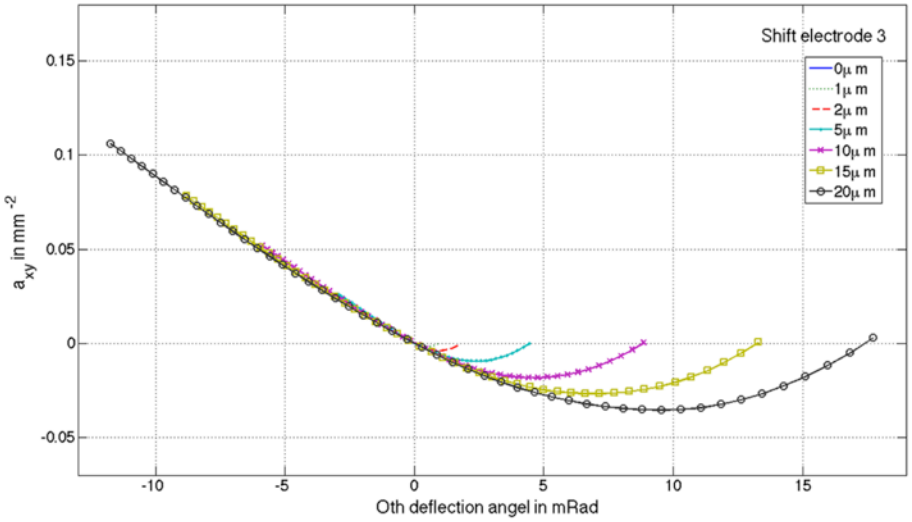

Figure 17: Second order a_{xy} coefficient in mm^{-2} versus deflection angle in mRad for various shifts values in µm of electrode 3.

The largest value for second order is b_{y2}=0.16 mm^{-2}, this corresponds to f (3000V) ≈ 1.57mm. In our simulations the largest starting value of x or y equals 5µm, giving a maximum contribution to the spot in the general focal plane that is given in equation (14).

$$2nd_{contribution} = b_{y^2} y^2 f = 0.16mm^{-2} \cdot (5\mu m)^2 \cdot 1.57mm \approx 6.3nm \quad (14)$$

The behavior of the second order coefficient for the decelerating shift lens is surprising. With the help of figure 18 we try to explain why the accelerating lens only shows an increase of the second order coefficients and the decelerating lens shows a curve with a minimum. An electrostatic lens can be thought of as consisting of many positive and negative lenses at the entrances and exits of the electrode apertures. Each sub-lens gives a deflection with one term proportional to the radius in the lens plus a term proportional to the radius in the lens to the third power. When a beam travels off-axis through a lens, the effect of the third order term in the radius is a second order deflection when analyzed with respect to the center of the beam. Thus, the second order terms of the sub-lens at the exit of our shift lens can either have the same sign or the opposite sign of the second order effect of the deflection in the shifted electrode. In the decelerating lens the two terms are clearly opposite, while in the accelerating lens they always have the same sign.

Third order effects

In our simulation of the rotationally symmetric case we have found a third order value of a_3=13mm^{-3} and f= 1.74 mm, corresponding with a Cs value of 119 mm. We have verified the value for the third order effect by calculating the spherical aberration coefficient for the system with rotational symmetry using the simulation program EOD[16]. The geometry is almost identical except that there is no closing boundary. EOD gives a Cs of 157 mm and f=1.73 mm. We did not look further into the possible causes of the discrepancy because for our present purposes the third order aberrations are not of interest. When they become important, we'll turn to double precision in the ray tracing.

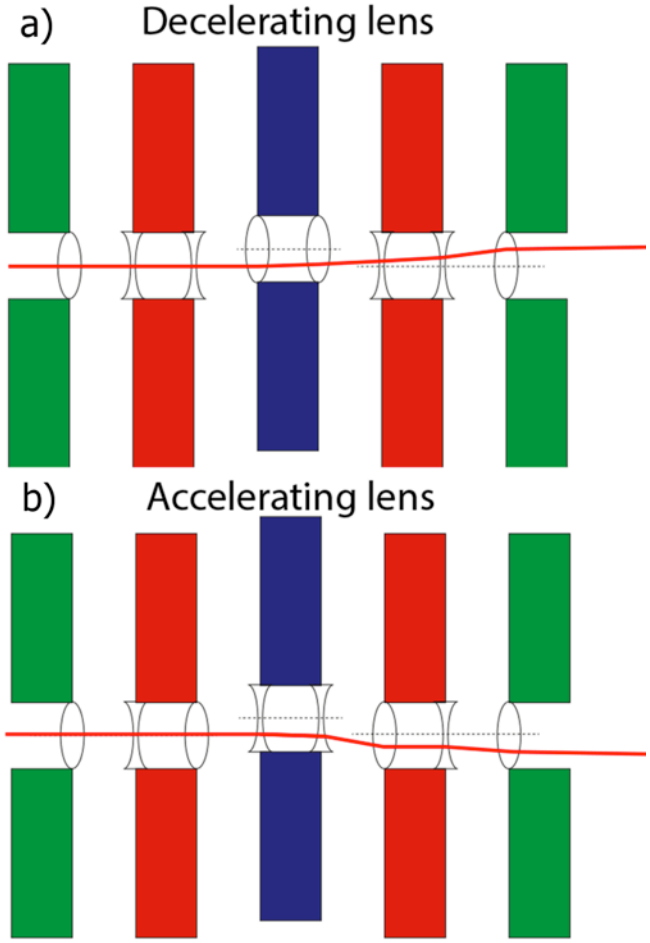

Figure 18: Sketch of on axis ray for both the decelerating (a) and accelerating (b) shift lens. The 'separated' negative and positive virtual lenses are sketched for purposes of explanation only. See text for more details. Note these 'separated' lenses do not have equal strengths!

Discussion

From the simulations of a beam with a radius of 5 μm, we conclude that the largest contribution to the spot size comes from the first order coefficients: defocus and astigmatism. However, since the calculated coefficients are independent of *x* and *y,* we can also calculate the contributions for beams with a larger radius. In table I we have calculated the contributions from the other orders for different beam radii, where we have used the largest value of the coefficients and their corresponding focus distance.

In table I we have separated the first order astigmatism from the curvature defocus. We see that the first order aberrations dominate for the given examples, but due to the power law behavior of the second and third order aberrations the higher orders become increasingly important: for a beam with a radius of 25 μm the third order is the

dominant contribution. Note that we have only looked at the largest off-axis distance in the Gaussian image plane of the center beam. In general, the authors recommend to calculate the contributions of the different orders to the full width containing 50% of the current (FW50)[17] and optimize the defocus from the Gaussian image plane.

Table 1: Aberration contributions for different beam radi

Beam radius	1st order (astigmatism)	1st order (curvature defocus effect)	2nd order	3rd order
5 µm	38 nm	55 nm	6.3 nm	2.6 nm
10 µm	76 nm	110 nm	25 nm	20 nm
15 µm	114 nm	165 nm	57 nm	69 nm
20 µm	152 nm	220 nm	100 nm	163 nm
25 µm	190 nm	275 nm	157 nm	319 nm

Conclusion and outlook

In this paper we have studied the optical deflection and aberrations that are induced by a five electrode electrostatic lens whereby the middle electrode is shifted laterally, a so-called shift lens. A simple model based on Taylor polynomial expansion has been proposed and validated to describe the optical behavior and aberrations. The validation has been done with a new developed simulation package based on the boundary element method. In contrast to the study of the multi-beam rotation corrector by Zonnevylle et al.[3], we did not focus on a specific application, but have run the simulation over a much wider range. We conclude that for every specific application a detailed study in combination with a geometry optimization will be necessary.

Further research on the concept of the shift lens could be aimed at minimizing the defocus/field curvature and astigmatism by changing the shape of the aperture of the shifted electrode. For example, a change in radii or the use of elliptical instead of circular electrode apertures may reduce these effects.

Another application of the shift lens could be the correction of the spherical aberration induced by the condensor lens in a single electron source multi beam[4,18]. For that purpose the shift of the lens aperture in the array electrode should be a third order function of the radius, instead of a first order function as in the rotation corrector and it should be in the radial direction instead of the tangential direction.

Acknowledgment

This work has been sponsored by the NanoNextNL program and Mapper Lithography bv.

Reference

[1] L. a. Baranova, F.H. Read, Rev. Sci. Instrum. 65 (1994) 1993.

[2] P.W. Hawkes, E. Kasper, E. Kasper, Principles of Electron Optics Series, Academic Press, 1996.

[3] A.C. Zonnevylle, C.T.H. Heerkens, P. Kruit, M.L. Wieland, F.M. Postma, S.W.K.H. Steenbrink, Microelectron. Eng. 87 (2010) 1095.

[4] M.J. Wieland, G. de Boer, G.F. ten Berge, M. van Kervinck, R. Jager, J.J.M. Peijster, E. Slot, S.W.H.K. Steenbrink, T.F. Teepen, B.J. Kampherbeek, Proc. SPIE 7637 (2010) 76370F.

[5] R.F. Whitmer, J. Appl. Phys. 27 (1956) 808.

[6] E. Hecht, Optics 4th Edition, 2001.

[7] J.T.L. Thong, ed., Electron Beam Testing Technology, Springer US, Boston, MA, 1993.

[8] L. Reimer, Scanning Electron Microscopy — Physics of Image Formation and Microanalysis, 2nd ed., Springer, 1987.

[9] P.A. STURROCK, Philos. Trans. R. Soc. London Ser. A-Mathematical Phys. Sci. 243 (1951) 387.

[10] E. Munro, J. Vac. Sci. Technol. B 6 (1988).

[11] J. Zlámal, B. Lencová, Nucl. Instruments Methods Phys. Res. Sect. A 645 (2011) 278.

[12] J. Orloff, ed., Handbook of Charged Particle Optics, 2nd Edition, Edited by J. Orloff, 2nd ed., CRC Press, 2009.

[13] T. Verduin, B. Cook, P. Kruit, J. Vac. Sci. Technol. B Microelectron. Nanom. Struct. 29 (2011) 06F605.

[14] W. Kahan, Commun. ACM 8 (1965) 40.

[15] MATLAB version R2011b,7.13.0.564. The MathWorks Inc., 2011.

[16] B. Lencová, J. Zlámal, Phys. Procedia 1 (2008) 315.

[17] J.E. Barth, P. Kruit, Optik (Stuttg). 101 (1996) 101.

[18] C. Klein, J. Klikovits, L. Szikszai, E. Platzgummer, H. Loeschner, Microelectron. Eng. 87 (2010) 1154.

Ch. 4 Multi-Electron-Beam Deflector Array

Authors: A.C. Zonnevylle, C.Th.H. Heerkens C.W. Hagen and P. Kruit

This chapter has been published: A.C. Zonnevylle et al., Microelectronic Engineering 123 (2014) 140–148

Abstract

In single electron beam columns the alignment of the beam is obtained either by mechanical shifting the lenses or by x/y alignment deflectors. We are developing multi electron beam columns for electron microscopy and lithography. The problem in multi-beam systems is that mechanical alignment and simple x/y deflectors can only align the total array of beams in the x/y direction and not correct the position of individual beamlets. We present here a simple design, fabrication, electron-optical analysis and experimental results of a multi-beam x/y deflector array that can deflect each beamlet separately. The array is fabricated with micro-fabrication technology with in-plane deflection plates made of molybdenum. The electron optical properties of this in-plane deflector are simulated and compared to a traditional deflector. The experimental measurements are compared with the simulations and are in agreement.

Introduction

Single beam scanning electron systems have been around for almost 50 years with two main applications: microscopy and lithography. These techniques have enabled respectively sub nm imaging [1] and sub 10 nm patterning [2].
The higher the resolution, the more difficult it is to get a large current in the electron beam. At the same time there is a need for higher speed, both in electron microscopy and in electron beam lithography. This can be obtained by having multiple beams simultaneous instead of only a single beam. A multi-beam system can only be realized by micro-fabrication of some of the multi-beam electron optical elements. Some examples of micro-fabricated multi-electron-beam optical elements can be found in [3–17].

A specific example of a multi-beam system that is being developed for high speed microscopy is the multi-beam SEM concept at the TU Delft[10–12]. This multi-beam SEM has 196 individual beams that are focused in a conventional scanning electron beam column into individual spots. The creation of these individual beams is done by micro-fabricated electron optical elements that are incorporated in the column.

An example of a multi-beam lithography system is the MAPPER system based on MEMS multi electron beam technology that is currently being developed by MAPPER Lithography b.v.[3,8] . This machine uses more then 13000 electron beams in parallel, all focused, deflected and individually blanked by micro-fabricated electron optical elements.

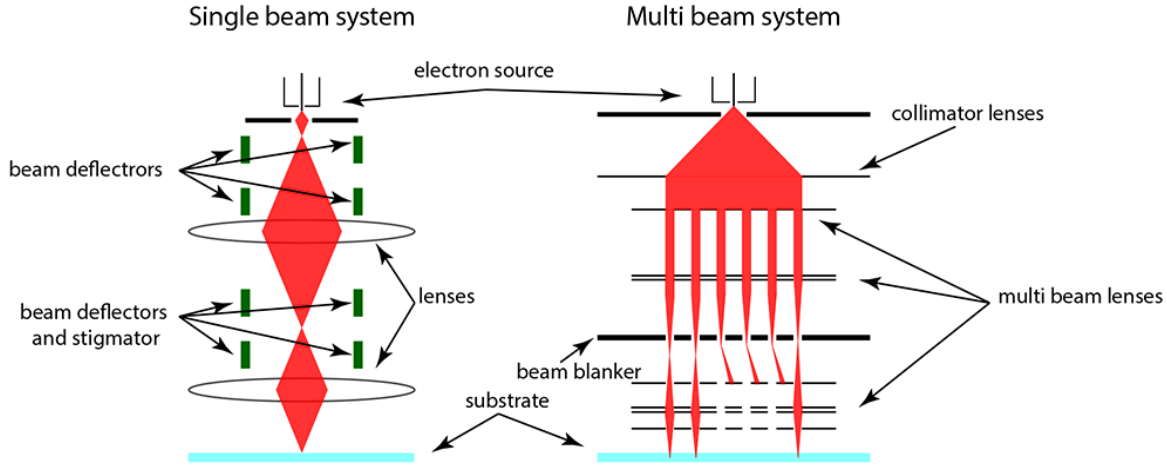

Figure 1: Single beam system with alignment deflectors and stigmator versus a Multi-beam system without any individual beam control. (Systems are illustrative sketches and are not drawn on scale)

In a single electron beam system the alignment of the beam through the different lenses is achieved either by mechanical shift of the lenses or by using deflectors. However, the alignment of many beams through the subsequent lens arrays in a multi-beam electron optical column is not as straightforward. Figure 1 shows a comparison between a multi- and a single-beam system. In most cases, the alignment in micro-fabricated multi-beam systems is done with mechanical translation devices based on leaf springs and piezo actuators and deflectors that deflect the whole array of beams in the *x*-*y* direction, but this is not always sufficient.

For future generation multi-beam systems it would be advantageous to also have alignment capabilities for each individual beamlet. This would allow for minimizing disturbances caused by, for example, charging effects, machine imprecisions, rotation alignment errors or even remaining deflection errors of beamlets due to residual spherical aberration of the collimator lens. To our current knowledge individual beam control systems that are implemented in multi-beam systems are beam blankers [14–17]. None of them have the capabilities of the *x*-*y* beam direction control as in single beam systems.

Deflector arrays for individual *x*-*y* beam control in a MEMS based multi-beam system can only be made using micro-fabrication technology, because the deflectors should have the same lateral size and pitch as the other micro-fabricated components. Typical aperture diameters are 5-100 µm at a pitch of 20-250 µm. In contrast with the design and fabrication of macroscopic deflectors, micro-fabricated deflector design and fabrication

is relatively new in the electron optics community [3–17]. One of the biggest challenges for multi-beam deflectors is to minimize the number of control wires necessary to control all these deflectors.

For example if we were to have *x-y* position control for each individual beamlet in a 200 multi-beam system it would require at least 4 deflector plates per beamlet and thus 800 control wires. Connecting that many control wires to a micro-fabricated device is already challenging, but having 800 vacuum feed through pins and wiring inside a vacuum chamber is almost impossible, let alone for high throughput lithography systems that can have up to 13000 beams needing 56000 individual wires or more!

Adding integrated control electronics to the micro-fabricated devices themselves can drastically reduce the number of control wires. Amplifiers that drive the deflection voltage per deflector plate can be realized by adding sample and hold circuitry [18] embedded on the multi-beam deflector substrate. In its most simple form this would reduce the required control wires to just 4 (ground, signal and 2 power wires), solving the control wire issue.
The next challenge that now arises is that the design of the micro-fabricated deflector plates should be compatible with both the IC fabrication process for the control electronics, the electron optical design rules and vacuum requirements. Conductive materials having insulating oxides and contamination residues of chemicals used in the processing will lead to beam disturbances through charging and have to be avoided. Copper and aluminum are well-established standard process metals in IC processing[19], but unfortunately they both have non-conductive oxides rendering them unsuitable from an electron optics point of view because the oxides may charge. Molybdenum as a conducting material is a good candidate, because it is allowed in some IC fabrication lines and has a conducting oxide. Although molybdenum has been used in IC fabrication since the 1970's [20], unfortunately there is little experience with this material in micro-fabrication processing and no experience whatsoever in the creation of micro-fabricated molybdenum deflector plates. A second challenge results from the fact that in IC processing it is much easier to deposit a thin layer in the plane of the wafer than to create a deflection plate perpendicular to the wafer, where the latter is the traditional deflector design: two plates, one on each side of the electron beam.

In this paper we will present a proof of concept design and manufacturing of a multi-beam *x-y* deflector array made by IC- compatible micro-fabrication technology for 25 beamlets with molybdenum as the conducting material.
We have excluded the integration of integrated circuitry since this has already been shown to be feasible for a multi-beam blanker array by Mapper Lithography bv.[3,8]. The focus lies on the fabrication of the electrodes of molybdenum within the restrictions posed by IC processing and the electron optical properties of deflectors made of thin layers in the plane perpendicular to the beam direction instead of traditional deflection plates along the optical axis. We shall call this kind of deflector an "in-plane deflector".

Multi-beam deflector design and electron optical properties

Figure 2 shows a principle sketch of the chosen design. The aperture diameter of 50 μm combined with a pitch of 150 μm has been chosen which are typical dimensions in multi-beam systems. To minimize crosstalk the wires connecting the electrodes to the contact pads on the edge of the chip have been buried under a shielding layer of molybdenum and each set of deflector plates is separated with a molybdenum grounded shield for the same reason.

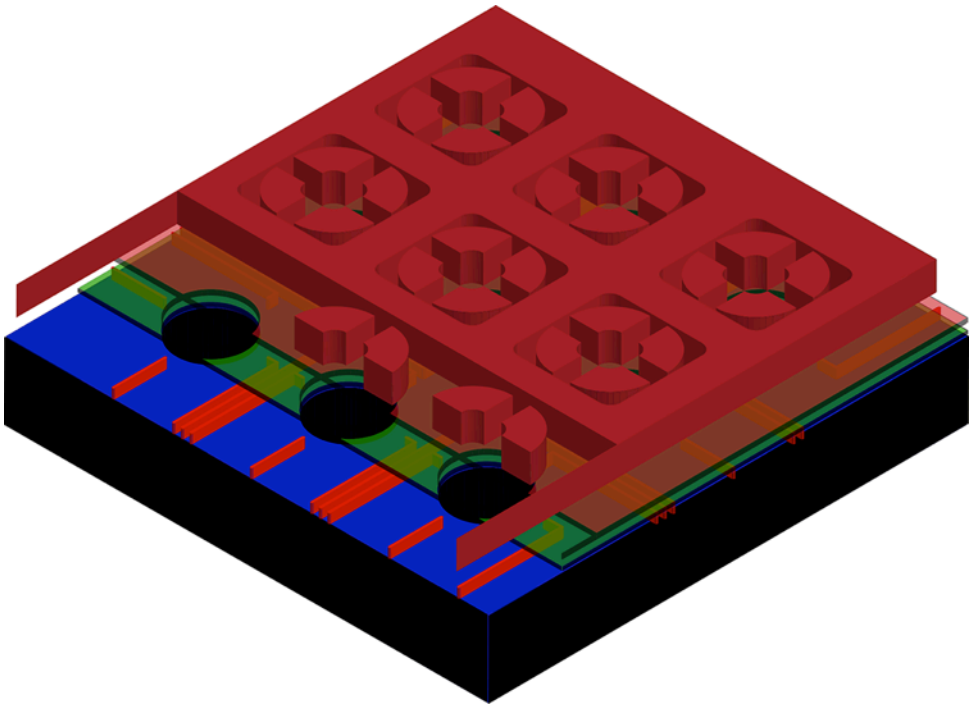

Figure 2: Design sketch of the 25 beam x-y deflector array. Deflectors and ground plane are etched out of deposited molybdenum. The first oxide layer is blue, the wiring is red, the second oxide layer is green and the molybdenum electrodes and shield are dark red. Note that the vertical scale is different from the horizontal scale.

The maximum number of contact pads that fit on the edge of a standard chip at our university's fabrication line is in the order of 100, which is equal to the maximum number of vacuum feed-through connections in our setup. This sets the upper limit of the number of beams to 25 for the deflector to be operated by simple external amplifier circuits with sample and hold electronics. We aim to measure the static deflection power and electrostatic cross talk so at this stage there is no need for high frequencies and the design does not have to be optimized for capacitance and induction.
To get a better understanding of the quantitative electron optical properties of the multi-beam deflector array we have first analyzed a single deflector.

Deflection strength and aberrations of a deflector

A general solution for the potential field in an electrostatic deflector, can be described by the harmonic coefficients of a Fourier series [21] as given in equation 1, for simplicity we leave out the sine term in equations 1 and 2, since it is just a matter of rotation.

$$\Phi(\mathrm{r},\varphi,\mathrm{z}) = \sum_{n=0}^{\infty} \Phi_n(z) \left(\frac{r}{a}\right)^n \cos(n\varphi)$$

eq. 1

In equation 1 $\Phi(\mathrm{r},\varphi,\mathrm{z})$ is the potential, r the radial distance from the axis, and φ the angle, $\phi_n(z)$ are the harmonic Fourier coefficients and a is the radius used in finding the ϕ_n Fourier coefficients by fitting equation 2 for the known potential distribution at r=a.

$$\boldsymbol{\Phi_{r=a}(\varphi, z) = \sum_{n=0}^{\infty} \Phi_n(\mathrm{z})\cos(n\varphi)}$$

eq. 2

If the 4 deflector plates are used as a *x-y* deflector, due to symmetry we will only have to consider the ϕ_1 and ϕ_3 terms, which are the dipole and the sextupole term while ignoring higher orders terms. The dipole term accounts for the deflection effect and the sextupole term accounts for the dominating unwanted aberration. Depending on the optical requirements, we can determine a maximum allowed beam radius. From this radius a fill factor can be determined. That is defined as the maximum allowed beam radius divided by the radius of the aperture. From equation 1 we note that the sextupole term must be made relatively small since it is proportional to r^3 in comparison with the wanted dipole term that is proportional to r, to obtain a large filling factor. Another option to increase the fill factor would be to use more electrodes around the aperture reducing aberrations, which we shall not further discuss here.

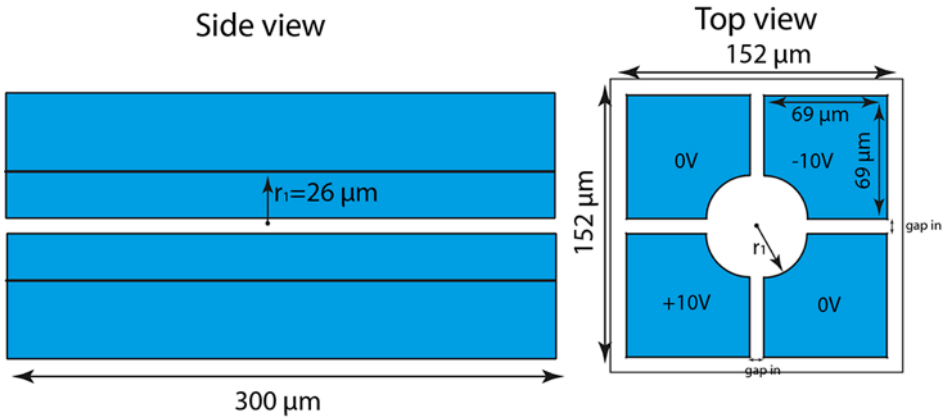

Figure 3: Finite length deflector, with same lateral dimensions as the in-plane MEMS deflector used later on. The blue patches in de top view are the individually controllable deflector plates, with applied voltages as used in the simulations. The distance gap-in is 4 µm.

In order to compare the properties of our deflector to the traditional electrostatic finite length deflector, we shall first review the properties of the latter. Figure 3 depicts a finite plate deflector with lateral dimensions as simulated. We have used SIMION3D [22] to calculate the potentials on a circle with a radius a=20 µm, for φ =[0-2π] from which the Fourier coefficients are determined at multiple z planes. This result is plotted in figure 4.

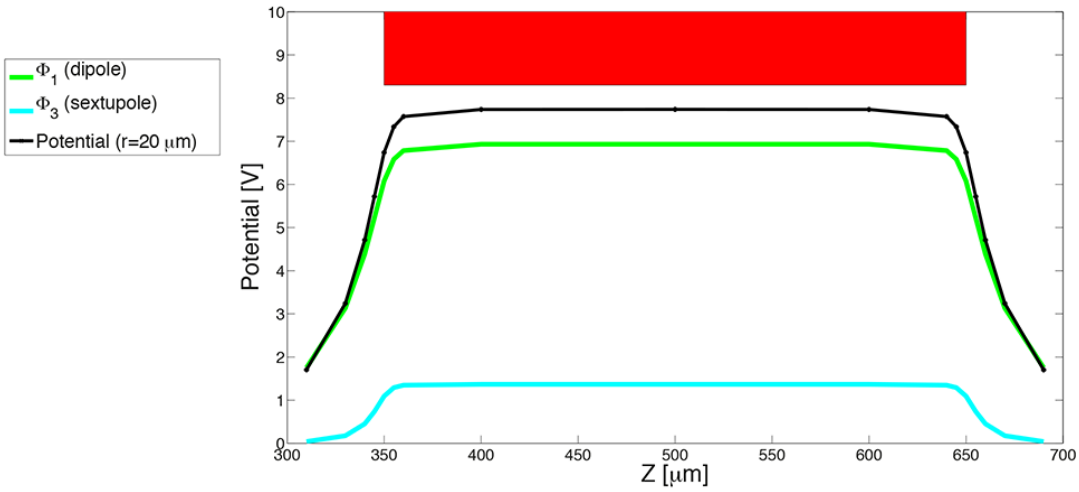

Figure 4: Potential and Fourier coefficients of the dipole and sextupole term at different z coordinates for the simulate plate deflector. The red block represents the defector plate.

Figure 4 shows that not only the area between the electrodes contributes to the deflection. Although the field is strongest inside the deflector also the area outside the deflector gives a contribution. For macroscopic deflectors this outside contribution can be neglected in most cases [21]. We can define a quality factor for a deflector as the ratio

between the desired dipole and the undesired sextupole by dividing the area below the dipole and the sextupole graph in figure 4, given in equation 3.

$$quality\ factor = ratio_{dipole/sextupole} = \frac{\int \phi_3\, dz}{\int \phi_1\, dz}$$

eq3.

For the simulated finite deflector we find a quality factor of 0.1846, using the values found for the dipole and sextupole terms at r=20 µm.

We shall now analyze the properties of the in-plane MEMS deflector. From experimental studies on sputter deposition of molybdenum we found that we could deposit layers up to 10 µm thick with low stress and good adhesion properties but due to practical limitations on the deposition time in the fabrication lab we limited the thickness, i.e. the deflector plate length, to 600 nm.

Following the same analysis as for the finite deflector we calculated the field for a 600 nm long deflector, i.e. the in-plane deflector.

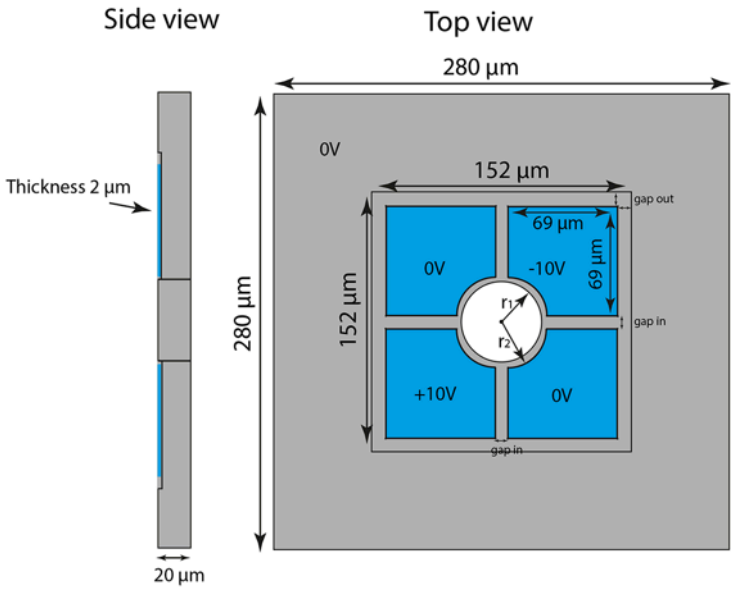

Figure 5: Geometry used in the simulation for the in-plane deflector. Grey is the base and surrounding ground plate on which the deflector plates are positioned. Blue are the individually controllable deflector plates, with applied voltages as used in the simulation. The dimensions are: gap-in= 4 µm, gap-out=5 µm, r1=25 µm and r2=26 µm.

Figure 5 shows the geometry used in the simulation, due to limited available mesh size we modeled the length as 2 µm, but we will see that this difference between fabrication and simulation can be ignored since the field outside the deflector dominates the

behavior. Figure 6 shows the simulated equipotential lines at different views and indeed we see that the outside field dominates the behavior.

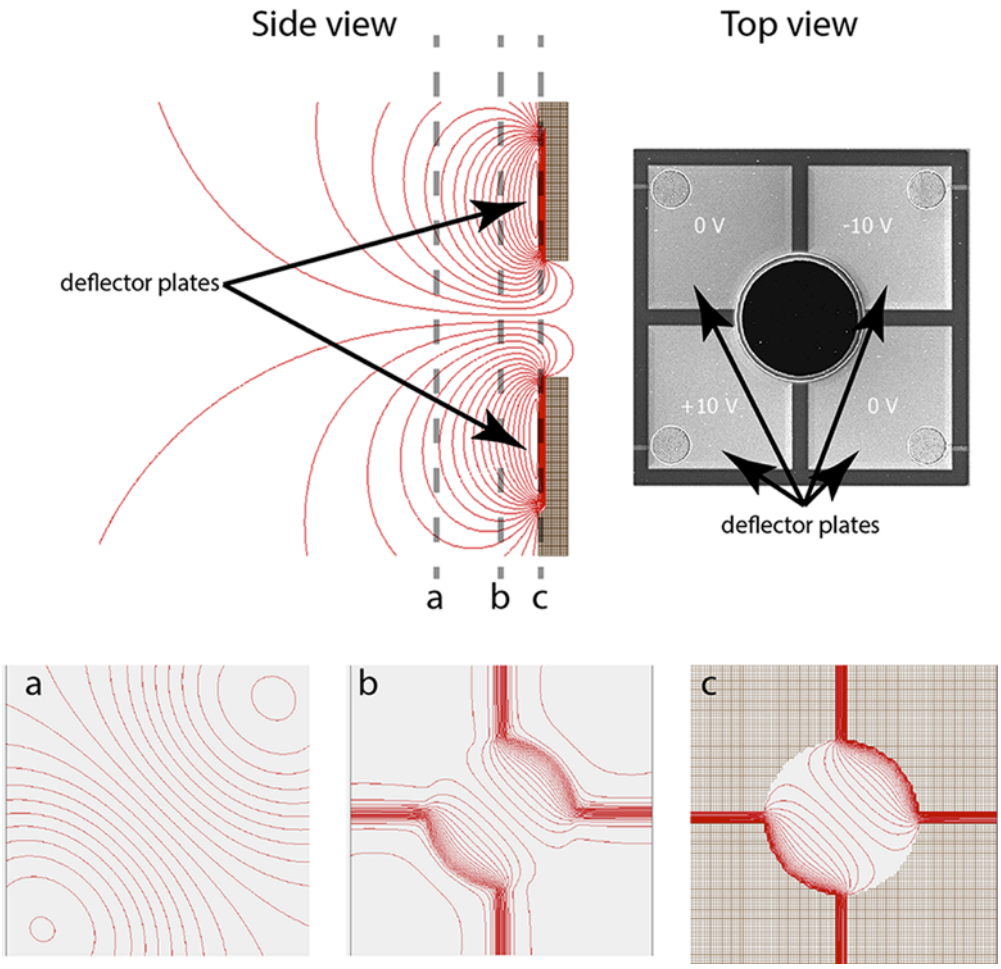

Figure 6: Simulation of the equipotential lines for the deflector visualizing the protruding equipotential lines in a side view in the upper left of the figure. The three lower images are top views of the equipotential lines, where a, b and c correspond to the cross sections drawn in the upper left side view image. Note the simulation program used is not able to use the same scaling for the equipotential fields drawn for each top view. Upper right image shows a top view of a set of individual deflector plates where the inset gives the applied voltage on the deflector plates as used in the determination of the equipotential lines.

As before, the potentials on a circle with a radius r=*a*=20 μm, for φ =[0-2π] are calculated with the same simulation program and the Fourier coefficients are determined as before, plotted in figure 7. Again, only the dipole and sextupole term need to be considered. The strongest field is no longer between the deflector plates.

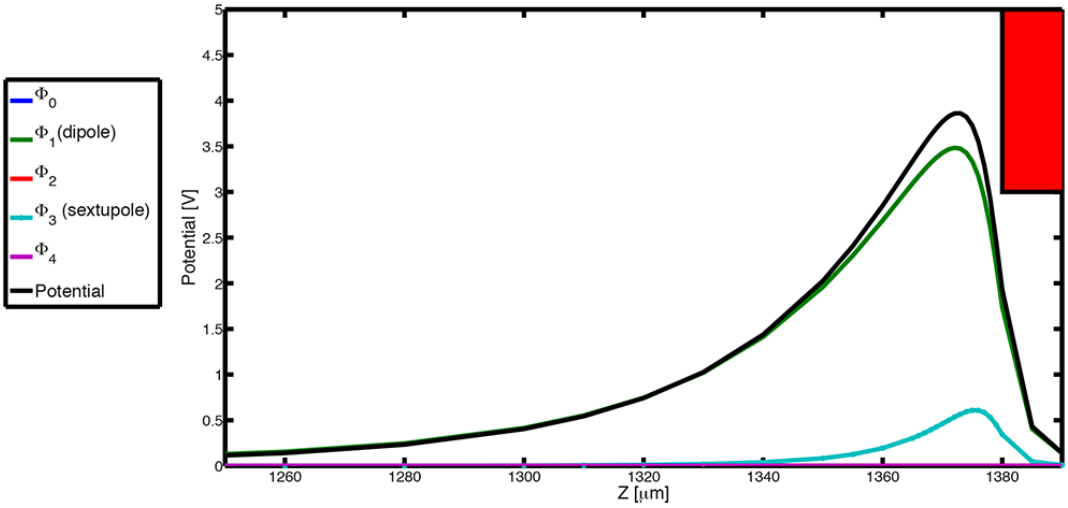

Figure 7: Potential and Fourier coefficients describing the in-plane deflector. The red rectangle represents the substrate with the thin plate electrode on the left hand side.

When we use $\alpha \overset{\text{def}}{=\!=} \frac{\int Edz}{2\theta}$ we see that the deflection angle for the in-plane deflector is only 0.2 mRad compared to 2.9 mRad for the long finite plate deflector for a 20 keV electron beam. We now express the total strength of the in-plane deflector by $\int Edz$=8.11V compared to 129.9V found for the long finite deflector, making this micro-fabricated deflector a much weaker deflector. This much smaller strength, however, is still sufficient for individual beamlet alignment in a multi-beam system. The quality factor for this thin plate deflector is found to be 0.0760, calculated with the same method and radius as for the finite length deflector. As the radii of the two deflectors are equal we can compare the quality factors of both deflectors. So we may conclude that although this thin plate deflector is much weaker, the quality factor is much better compared to the long deflector. Meaning that this thin plate deflector can be used with a larger fill factor than the finite deflector.

Fabrication

The devices were manufactured at the integrated circuit processing lab of DIMES following the standard process charts as much as possible. The only exception made is the choice for molybdenum for all metallization steps.
It can be anticipated that when circuitry is to be included in the future another IC fab might be chosen with a possibly more restricted policy towards molybdenum. In that case, all the steps involving the molybdenum deflector electrodes can be done in a separate fab after the circuitry is ready and tested.
The feasibility of etching arrays of apertures through an existing chip keeping the circuitry intact has been proven [3]. The processing sequence is depicted in Figure 8 and the separate steps are described in the text.

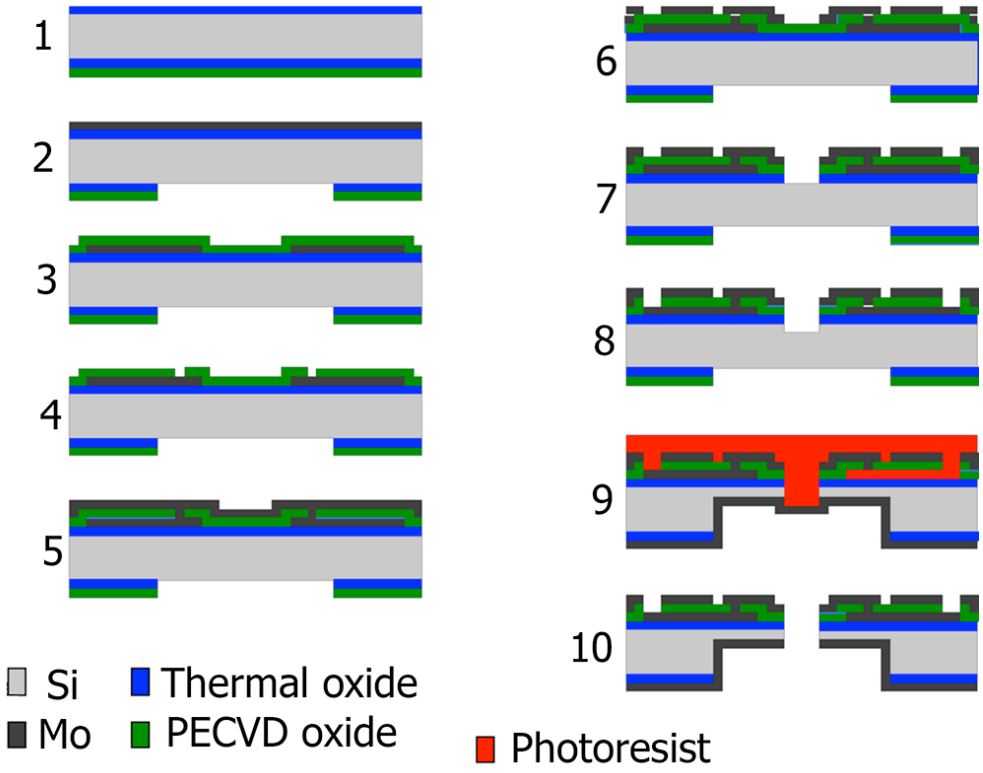

Figure 8: Process sequence of the 25 multi-beam molybdenum *x-y* deflector.

Step 1: Starting with a double side polished silicon wafer, alignment markers for lithography were etched by RIE (reactive ion etching) and a wet thermal silicon dioxide layer was formed. On the back side an additional PECVD (plasma enhancent chemical vapour deposition) oxide was deposited allowing for through wafer etching later on.

Step 2: The oxide layers on the backside were then patterned which later will be used to locally thin the wafer.

Step 3: The first molybdenum layer was deposited on the front side by sputter deposition and patterned using RIE to form the wiring and bonding pads. In this case molybdenum was used for all metalization steps, for simplicity, and to ensure good electrical contact between the different layers. The wiring was then buried under a layer of PECVD silicon dioxide. To improve the step coverage a PECVD oxide layer of 800 nm was deposited followed by an etch-back RIE step of 600 nm followed by a second deposition step of 600 nm. The intermediate etching step improves the step coverage since the anisotropic process etches mainly the horizontal surface leaving the side walls covered with oxide.

Step 4: The frontside oxide was then patterned to allow contact from the wiring to the deflector plates.

Step 5: A 600 nm layer of molybdenum was deposited that will form the deflector plates and surrounding shielding plane.

Step 6: The molybdenum layer is patterned and etched with RIE to form the quadrupole plates, the shielding and contact pads.

Step 7: The oxide was removed from the contact pads and around the apertures area by RIE etching

Step 8: The apertures were etched by DRIE (deep reactive ion etching) using a mask of hard baked photoresist.
Step: 9 The front side was then covered by a 15 μm thick spraycoated layer of photoresist and the backside was etched by DRIE until the photoresist pattern appeared on the back side of the wafer. By locally thinning the wafer the aspect ratio of the apertures can be kept low. The back side can then be covered by sputtercoating it with molybdenum.

Step 10: As a last step the photoresist can be removed together with the molybdenum on it's surface.

Since the sputtercoater was temporarily out of order the back side of the devices that were used for the actual experiments have not been sputtercoated with molybdenum. Figure 9 shows a SEM image of the fabricated multi-beam 4 plate *x*-*y* deflector.

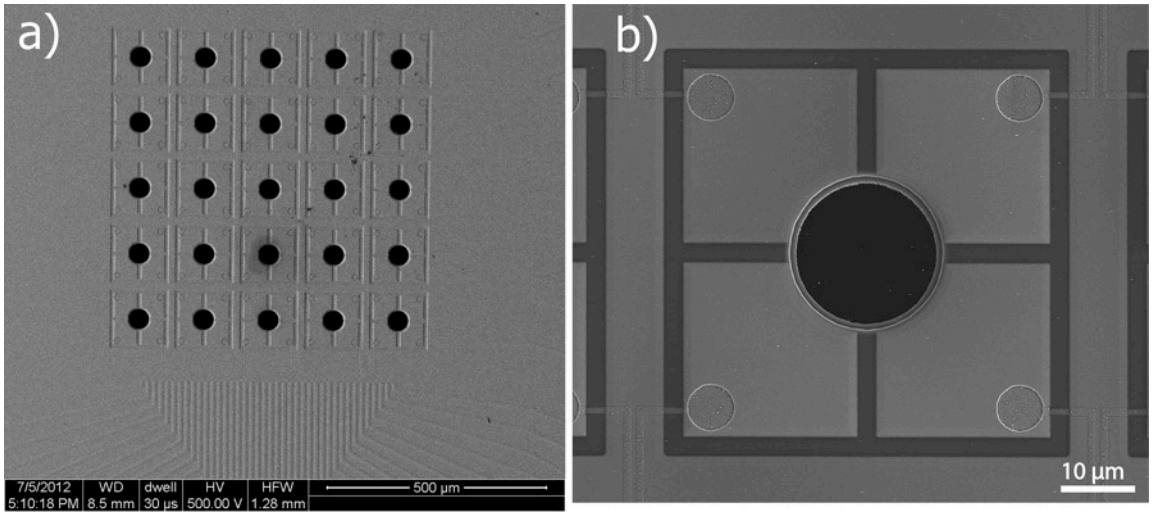

Figure 9: SEM image of the fabricated molybdenum deflector array. a) All 25 apertures with each 4 individually controllable deflection plates. b) Zoom-in of a single beamlet aperture and its 4 deflection plates.

The fabricated chips were ultrasonic wire bonded with aluminum 15 µm thick bond wires, from the molybdenum bond pads to the gold pads on a printed circuit board (PCB) that wires the connection to the outside world.

Experimental

The multi-beam deflector is tested in an FEI Quanta 200 FEG SEM that has a customized door with a dedicated stage. This stage is used as an experimental platform with enough space to build up small multi-beam stacks and install a 100-pin feed through for the electrical connections. An advantage of using the SEM is that the electron beam parameters can be adjusted in a matter of seconds from finely focused up to a parallel beam at different probe currents and beam energies.

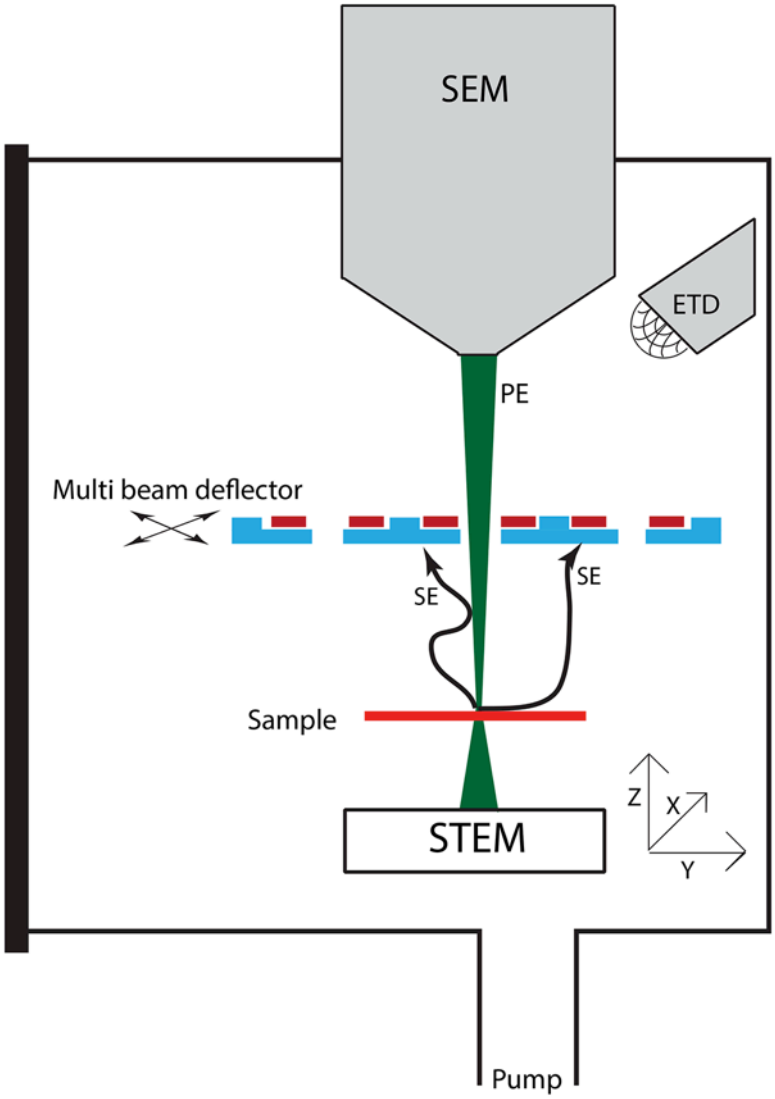

Figure 10: Schematic drawing of the SEM, the Everhart Thornley detector (ETD), the multi-beam deflector on an electronically controllable stage and the sample with the STEM detector that is mounted on a separate electronically controllable stage.

Since the deflector array in combination with the PCB and the wiring is blocking the secondary electrons, emitted from the sample, from reaching the detector, we used a STEM (scanning transmission electron microscopy) detector instead. This STEM detector is mounted below the sample as shown in the experimental setup in figure 10. Figure 11 shows a photograph of the experimental setup and its components.

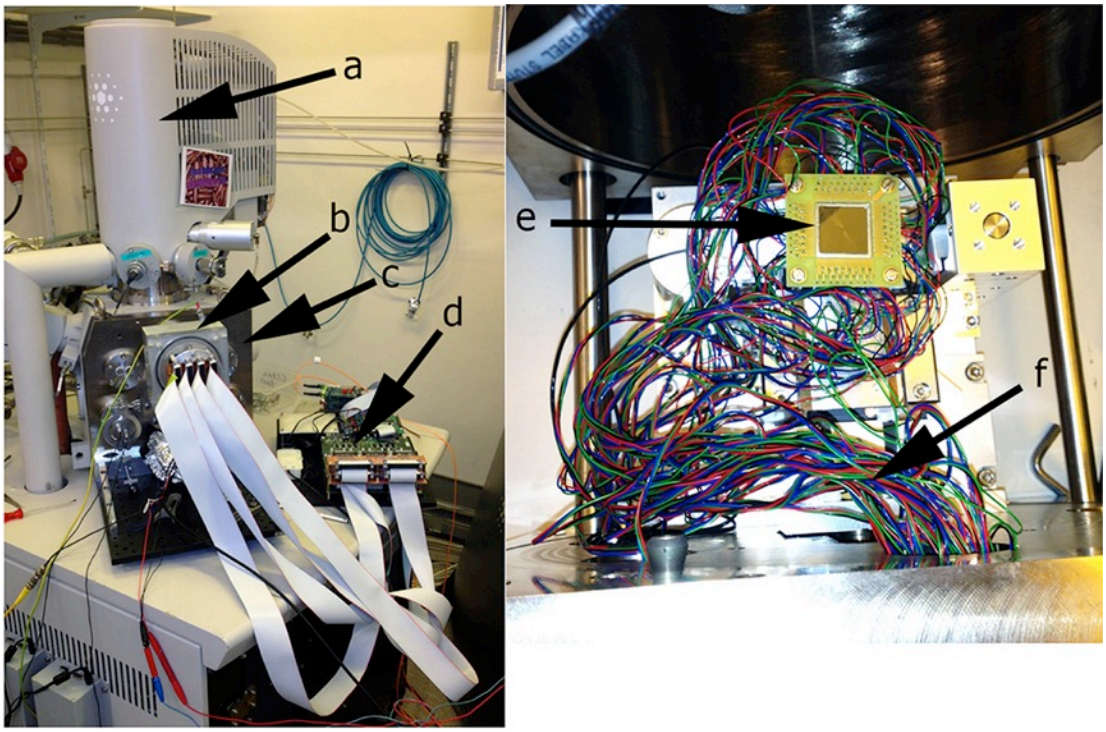

Figure 11: a) FEI quanta 200 FEG SEM, b) 100 pins vacuum feed through, c) custom SEM door, d) deflector electronics for 100 deflector plates, e) mounted multi deflector on x-y stage, f) the 100 control wires.

The voltages on the deflector plates are controlled by amplifiers, each of which has four channels such that each beamlet has its own amplifier electronics on the PCB board and we can supply each electrode with -10 to +10 volt in steps of 1.2 millivolt, 14 bit digitally controlled. The deflector plates were all controlled using a *Labview* [23] program and standard *National instrument* acquisition cards to supply the digital signals to home built amplifiers with sample and hold circuits.

The first measurement done inside the SEM was to check whether all deflectors could be controlled individually and whether there were internal short circuits. We used voltage contrast imaging [24] to visualize the different applied potentials to the deflector plates. When applying a potential to an object while imaging it in a SEM in secondary electron detection mode, the object will reveal a different contrast. When applying a negative potential more secondary electrons will be emitted from the object, giving more SE signal and the object becomes brighter in the image. The opposite will happen for a positive potential difference, the object will become darker.

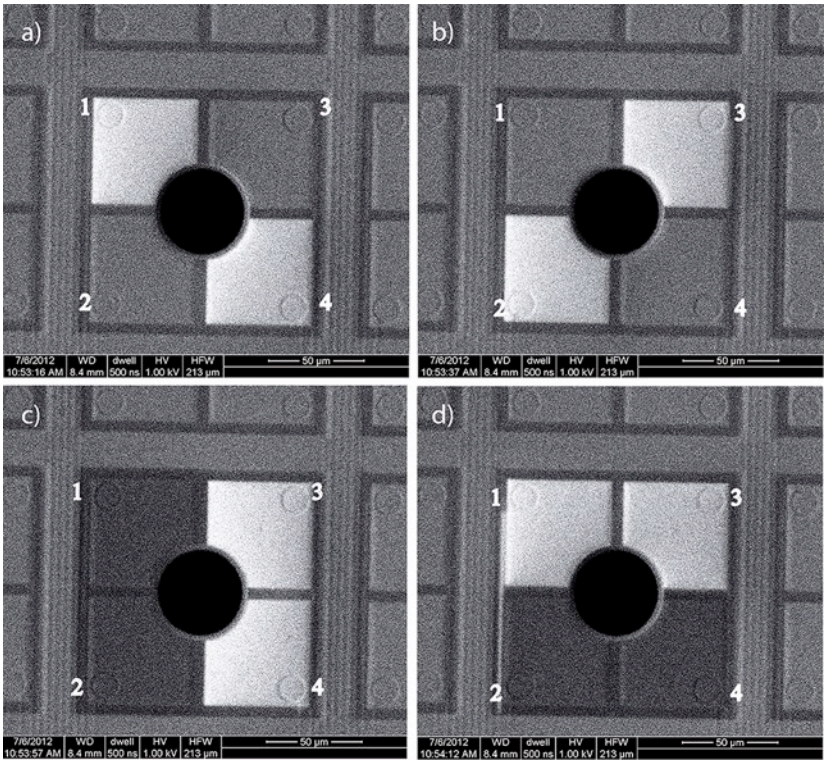

Figure 12: Voltage contrast images of a thin-plate deflector. a) -5 volt on plate 1 and 4, b) -5 volt on plate 2 and 3,c) -5 volt on plate 3 and 4, +5 volt on plate 1 and 2, d) -5 volt on plate 1 and 3, +5 volt on plate 2 and 4.

Figure 12 shows voltage contrast images for a set of deflector plates. We have repeated this measurement for all 25 deflector sets and found that from 100 deflector plates, 16 could not be controlled, due to fabrication errors.

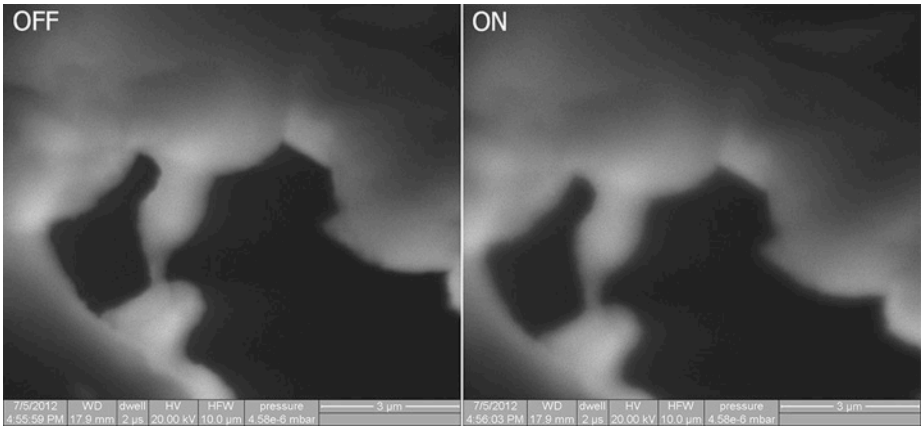

Figure 13: STEM images of sequential taken images of deflector (0V) off a) and on b) (-10V). In the ON image a clear shift and additional a blur are visible

Next the deflection angle was determined and compared to the we may expect displacements of the beam of only microns for the typical deflection angles of 0.2 mRad that these deflectors are designed to produce, and the typical working distances used in the experiment. In order to measure this, we take advantage of the high resolution imaging capabilities of the SEM. Focusing the SEM beam through the deflector at the sample underneath the deflector, as in figure 10, and acquiring an image with the STEM detector we can compare off-state and on-state images for various deflector excitations and measure the displacements. Figure 13 shows two sequential images as an example. This experiment was done at beam energy of 20 keV, and the beam radius at the deflector plane is estimated to be approximately 8 μm, corresponding to a fill factor of 32%.

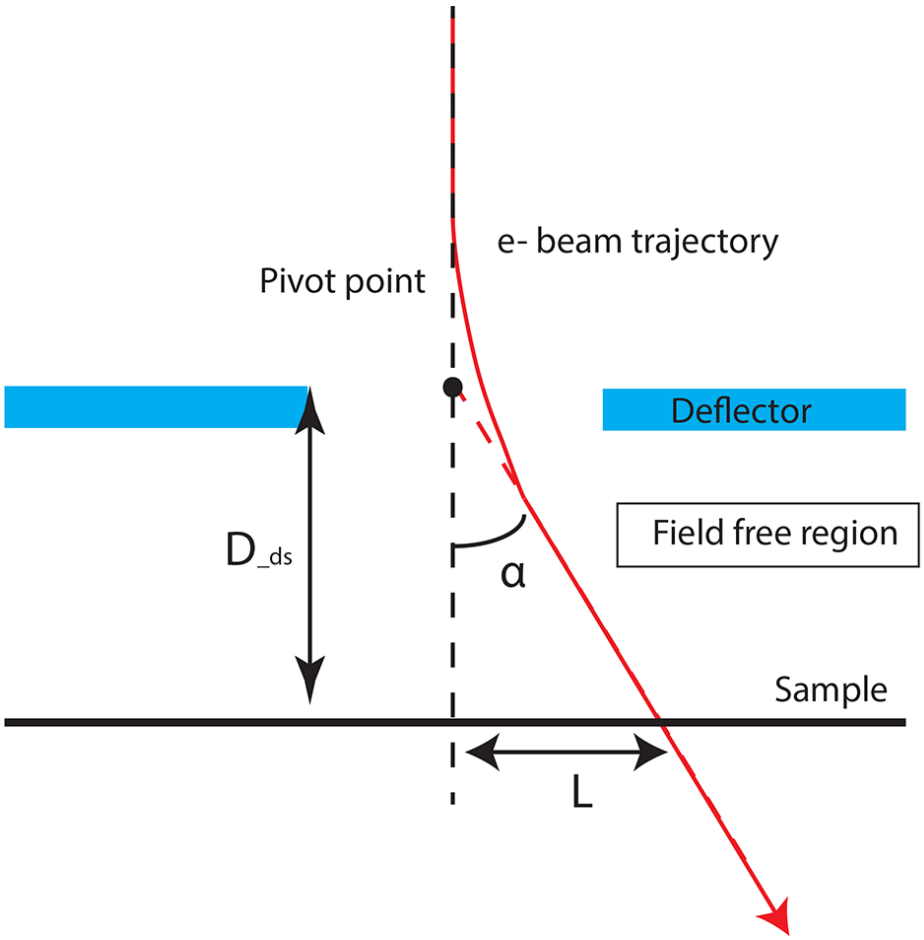

Figure 14: Deflection angle α determined by arctan(L/D_ds). L is the beam shift and D_ds is the distance between the top of the deflector and the sample.

The shift was measured using the "findshift" algorithm from the DIP image [25] toolbox in Matlab. This method is capable of detecting a shift of as little as 1/10 of a pixel[26]. This translates to a detectable physical image shift of at least 0.97 nm. With the measured image shift L the angle α was calculated as sketched in figure 14. The pivot point is assumed to be in the upper plane of the deflectors.

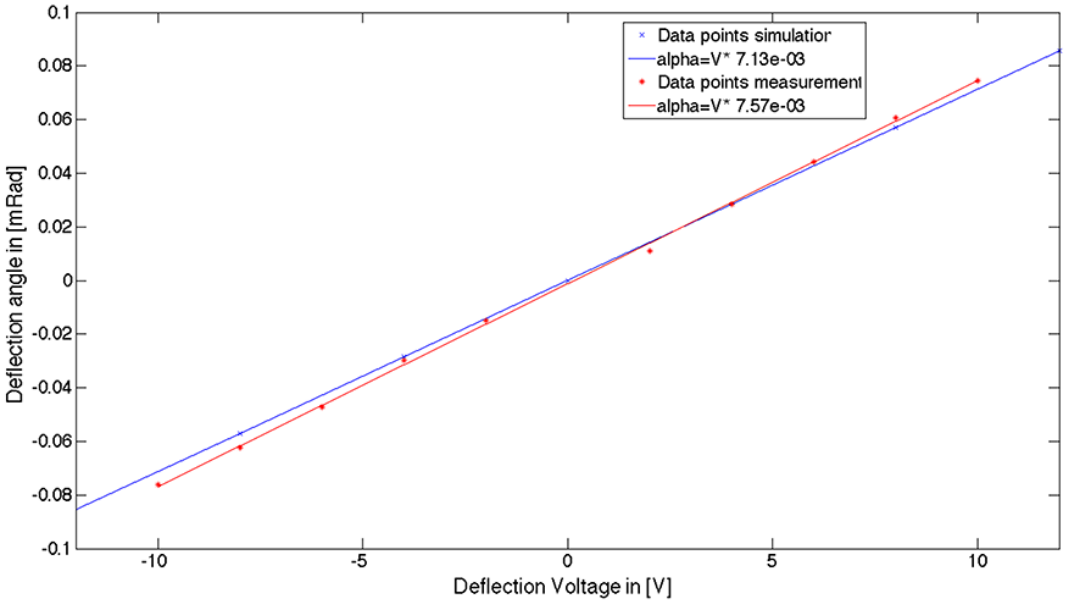

Figure 15: Measurement and simulation of the deflection angle α, for a 20 keV electron beam.

Figure 15 shows the simulated and measured deflection angle for different deflection voltages. We see a 5.8% difference in slope between measurement and simulation. This difference can be explained from a less-than-perfect SEM calibration and small differences between simulated and experimental geometries.

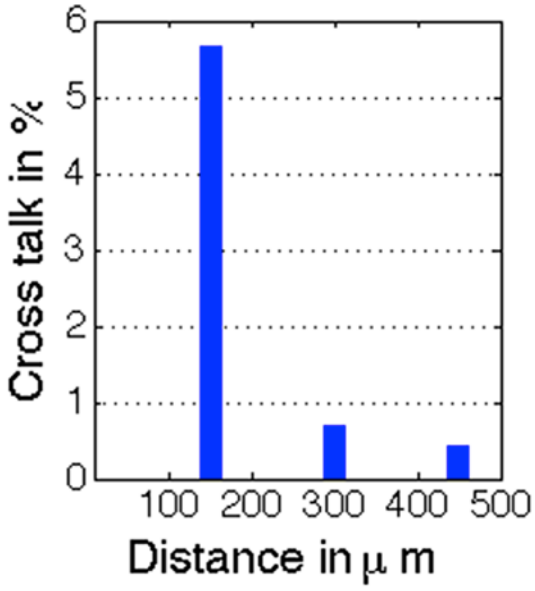

Figure 16: Measured cross talk between deflectors as a function of the distance between them.

A final measurement was done to determine the cross talk between neighboring deflectors. We have measured the deflection of a beam when switching on a neighboring deflector to a deflection voltage of 10 volt while keeping its own deflector in the off state. The cross talk is expressed as the ratio of the shift caused by a neighboring deflector and the shift caused by its own deflector. The image shift was determined using the same method as described above and the result is plotted in figure 16. We see that a nearest neighbor has an influence of 6% and the effects of more distant neighbors are below 1%. Since the deflectors have digital control, applying the appropriate deflection voltage when a neighbor is switched on can compensate the cross talk.

Discussion

In future researches we can use what we have learned about the electron optical properties of the MEMS thin plate deflector to develop new and innovative MEMS multi-beam devices. In figure 17 we have sketched two ideas. One has 8 deflection plates per beamlet instead of 4, allowing individual stigmation and deflection adjustment for each beamlet and also to reduce the effect of the higher order multipoles.

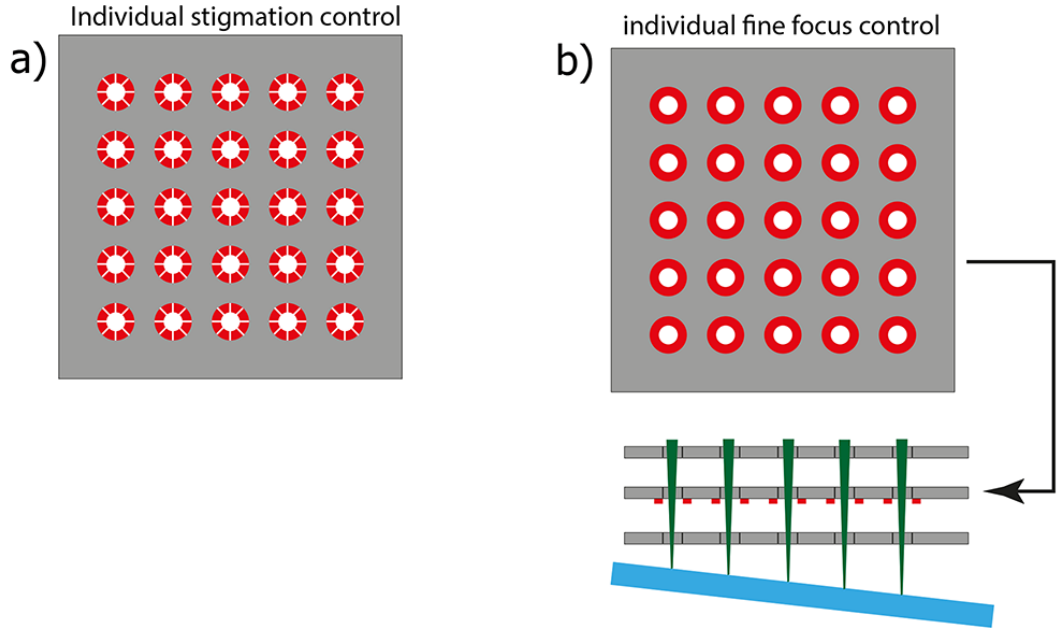

Figure 17: a) Individual stigmation control by having 8 individually controllable deflection plates per beamlet. b) Individual fine focus control by having a ring per beamlet inside a multi-beam einzel lens to compensate for example for tilt of the wafer.

The other idea is explained on the right hand side of Figure 17 where we have sketched a device for individual focus control. By incorporating an array of individual circular electrodes in a multi-beam einzel lens individual fine focusing can be achieved. This can be used for compensation of substrate tilt or height differences. Taking this idea one step further, instead of having individually controllable closed rings, we could divide the rings into 8 separate controllable electrodes. We could then have individual focus-control combined with deflection and stigmation, bringing us one step nearer to having the same control over each individual beamlet in multi-beam systems as we have in single beam systems.

For some purposes micro-fabricated deflectors with longer plates may be required in which case molybdenum might have to be deposited by other methods than sputter deposition. Our tests have shown that sputter deposition of molybdenum layers with low stress and good adhesion is limited to about 10 µm, which is still a short plate deflector. Another option would be the bonding of a polished molybdenum wafer to the silicon wafer. Hu et al. [27] has reported the patterning of 35 µm deep structures with a profile angle of 70^{o} and etch rate of 2.63 µm/min in bulk molybdenum wafers with RIE, which are promising results.

Conclusions

We have designed and manufactured a 25-beam electrostatic *x-y* deflector array, which gives individual control over each beamlet in a multi-beam system. The deflector plates and ground plane were prepared from deposited molybdenum and the micro-fabrication process is compatible with a bipolar- and CMOS integrated circuit process line. This compatibility makes it possible in the future to integrate control electronics on the substrate allowing for individual control of the beamlets in massively parallel electron beam systems.
The fabricated deflector is of the in-plane type. We have shown that it cannot be described using the same equations as for the long plate type deflectors. In-plane deflectors generally exhibit weaker deflection than equipotential long plate deflectors, however they exhibit reduced higher order multipole effects.
The deflector has been tested in a testing platform inside a SEM and simulation and experimental results are in agreement. Additionally we have measured the cross talk between neighboring beams to be less than 6%. In the outlook we have discussed some further applications and designs.

Acknowledgements

The NanoNext NL program and Mapper Lithography B.V have sponsored this work. We would like to thank the DIMES staff for their advice and help in the fabrication of this device, in particular H.Schellevis for setting up the deposition equipment for Molydbdenum in the DIMES class 100 LAB. F. Berwald, J. Nonhebel and H. van der Linden for their help and fabrication of the control software and electronics and B. Rieger for his advice which software to use to analyze the images

References

[1] www.fei.com

[2] H. Duan, D. Winston, J.K.W. Yang, B.M. Cord, V.R. Manfrinato, K.K. Berggren, J. Vac. Sci. Technol. B Microelectron. Nanom. Struct. 28 (2010) C6C58.

[3] M.J. Wieland, G. de Boer, G.F. ten Berge, M. van Kervinck, R. Jager, J.J.M. Peijster, E. Slot, S.W.H.K. Steenbrink, T.F. Teepen, B.J. Kampherbeek, Proc. SPIE 7637 (2010) 76370F.

[4] L.P. Muray, K.Y. Lee, J.P. Spallas, M. Mankos, Y. Hsu, M.R. Gmur, H.S. Gross, C.B. Stebler, T.H.P. Chang, Microelectron. Eng. 53 (2000) 271.

[5] L.P. Muray, J.P. Spallas, C. Stebler, K. Lee, M. Mankos, Y. Hsu, M. Gmur, T.H.P. Chang, J. Vac. Sci. Technol. B 18 (2000) 3099.

[6] K.Y. Lee, S.A. Rishton, T.H.P. Chang, J. Vac. Sci. Technol. B Microelectron. Nanom. Struct. 12 (1994) 3425.

[7] T.H.P.H.P. Chang, M. Mankos, K.Y. Lee, L.P. Muray, Microelectron. Eng. 57 (2001) 117.

[8] E. Slot, M.J. Wieland, G. de Boer, P. Kruit, G.F. ten Berge, a. M.C. Houkes, R. Jager, T. van de Peut, J.J.M. Peijster, S.W.H.K. Steenbrink, T.F. Teepen, a. H. V. van Veen, B.J. Kampherbeek, SPIE Lithogr. 6921 (2008) 69211P.

[9] P. Kruit, Microelectron. Eng. 84 (2007) 1027.

[10] A. Mohammadi-Gheidari, C.W. Hagen, P. Kruit, J. Vac. Sci. Technol. B 28 (2010) C6G5.

[11] A. Mohammadi-Gheidari, P. Kruit, Nucl. Instruments Methods Phys. Res. Sect. A 645 (2011) 60.

[12] T. Ichimura, Y. Ren, P. Kruit, Microelectron. Eng. 113 (2014) 109.

[13] M.A. McCord, P. Petric, U. Ummethala, A. Carroll, S. Kojima, L. Grella, S. Shriyan, C.T. Rettner, C.F. Bevis, in:, W.M. Tong (Ed.), Proc. SPIE, 2012, pp. 832311–832311–11.

[14] C. Klein, E. Platzgummer, H. Loeschner, G. Gross, SEMATECH Litho Forum – Maskless Lithogr. (2008).

[15] Y. Zhang, C.T.H. Heerkens, M.J. van Bruggen, P. Kruit, J. Vac. Sci. Technol. B 24 (2006) 2857.

[16] G. Winograd, V. Krishnamurthi, R. Garcia, L.H. Veneklasen, M. Mankos, F. Pease, J. Vac. Sci. Technol. B 18 (2000) 3052.

[17] M. Mohaupt, E. Beckert, T. Burkhardt, M. Hornaff, C. Damm, R. Eberhardt, A. Tünnermann, H.-J. Döring, K. Reimer, in:, Precis. Assem. Technol. Syst. IFIP Adv. Inf. Commun. Technol., 2012, pp. 42–50.

[18] P. Horowitz, Am. J. Phys. 58 (1990) 702.

[19] R. Waser, Anoelectronics and Information Technology : Advanced Electronic Materials and Novel Devices, 2nd ed., Weinheim: Wiley-VCH, 2005.

[20] L.E. Terry, R.W. Wilson, Proc. IEEE 57 (1969) 1580.

[21] P. Kruit, Introduction to Charged Particle Optics, Delft University of Technology, Delft, 2010.

[22] Simion 3D v.8.0, Scientific Instrument Services

[23] Labview 2011, National Instruments

[24] L. Reimer, Meas. Sci. Technol. 11 (2000) 1826.
[25] L.L. Hendriks, (2008).
[26] T.Q. Pham, M. Bezuijen, L.J. van Vliet, K. Schutte, C.L. Luengo Hendriks, in:, Z. Rahman, R.A. Schowengerdt, S.E. Reichenbach (Eds.), Proc. SPIE, 2005, pp. 133–144.
[27] J. Hu, Y. Zhang, S. Chen, S. He, N. Li, J. Chen, in:, Micro Electro Mech. Syst., IEEE, 2012, pp. 267–270.
[32] Tuan Q. Pham et al., Proc. SPIE 5817,133, 2005
[33] J. Hu, et al. Micro Electro Mechanical Systems (MEMS), 26, 2012

Ch. 5 A versatile tool for sub-micron alignment, stacking and adhesive bonding of electron optical MEMS components

Authors: A.C. Zonnevylle, R.F.C. v. Tol , C.T.H. Heerkens, C.W. Hagen and P.Kruit

Abstract

The design and construction of a sub-micron alignment tool for stacking and adhesive bonding of MEMS electron optical components is presented here. The tool consists of a six degrees-of-freedom stage and a linear motion stage, built into a system using very precisely machined components. Special test samples were fabricated with alignment markers, as well as inspection venires, to demonstrate that sub-micron alignment of multi electron beam array electrodes can be achieved using alignment markers. It was demonstrated that substrates could be adhesively bonded with sub 500 nm alignment errors after polymerization. And finally the versatility of the tool was illustrated using the alignment of electrodes positioned at different heights in a larger macroscopic optical component.

Introduction

Stacking of micro-/nano-electronic mechanical systems (MEMS/NEMS) has enabled the fabrication of complex 3D micro structures, such as pressure sensors[1], inertia sensors[2], lab on chip devices [3], micro-combustors chambers [4], and 3D integrated circuits [5,6]. Applications in this field are numerous and diverse. The emphasis is often on the bonding technique[7] used whereas alignment is less of a scientific topic. Recently, however, stacks of micro-fabricated components were also developed as optical elements in charged particle optical systems [8,9][10]. In such applications not just only the bonding technique but also the alignment of the elements in the stacks is extremely important, in fact this is largely determining the optical performance. Recent examples of such micro fabricated electron optical components and systems are i) multi beam blanker arrays [11–14], ii) a multi electron beam source [15–18], iii) multi beam array lenses[12], iv) multi beam array rotation correctors [19], v) a deflector/stigmator for micro columns [20][21], vi) micro column multi beam scanning systems [20,22], vii) high throughput multi beam lithography systems [8,23–26], viii) a novel aperture ion source(NAIS)[27,28]. Figure 1 shows a few examples of micro-fabricated electron optical component developed at Delft University of Technology.

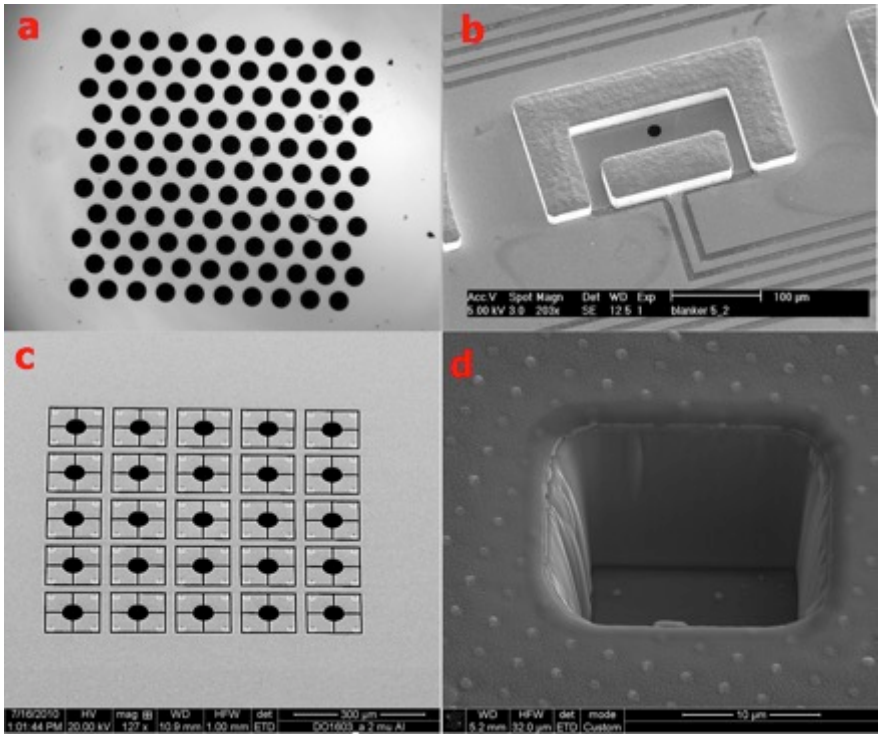

Figure 1: a) Multi beam array electrode of 100 µm diameter holes at a pitch of 150 µm. This is part of a multi beam electrostatic lens, b) Close-up of a single MEMS deflector for a multi beam lithography system [11]**, hole size 20 µm, c) 25 beam quadrupole deflector for individual beam deflection control**[21]**, d) Close up of part of the gas chamber of the NAIS**[28]**.**

A simple example of a micro-fabricated electron optical stack is the multi beam two-aperture array lens sketched in figure 2. An electrical insulating spacer separates the two aperture arrays that have to be laterally aligned, then stacked and bonded. The alignment accuracy depends on the dimensions of the elements and the optical requirements, but a general rule of thumb is that it should be better than 1% of the diameter of the apertures that constitute the array. A more specific example is a multi beam rotation corrector [21]. This device contains multiple apertures of 100 µm diameter, with a 150 µm pitch. The total stack has a height of 1.35 mm and consists of five multi beam aperture array electrodes of 150 µm thickness and three electrically insulating spacers of 200 µm thickness. The lateral alignment between the multi beam array electrodes must be equal to, or better than, 1 µm, according to our rule of thumb.

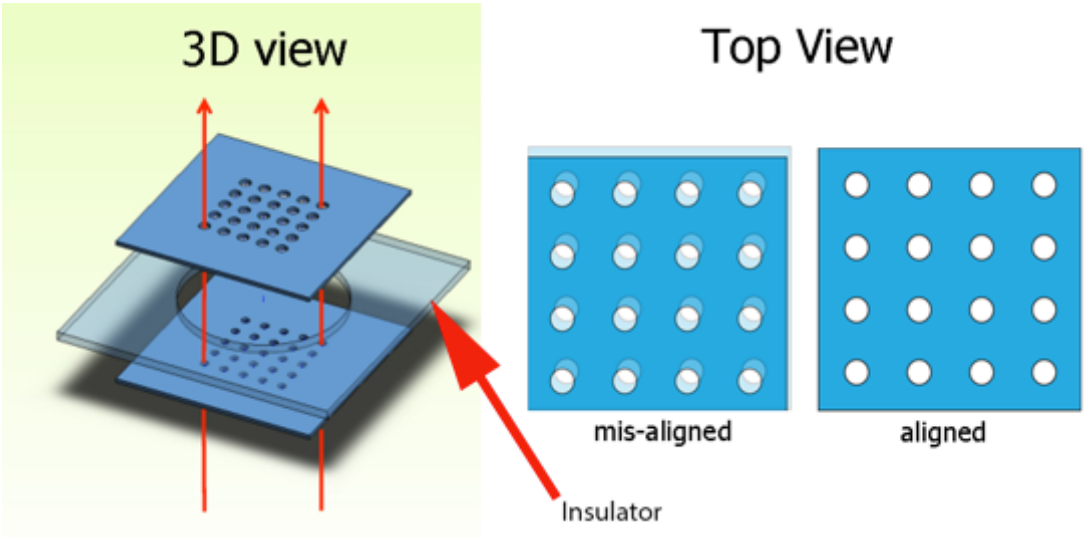

Figure 2: A simple multi beam lens stack in which two multi beam array electrodes are stacked onto each other with an electrically insulating spacer between them. The two array electrodes are aligned in the lateral direction; the criteria of good alignment depend on the application.

The challenge is now to achieve sub-micron lateral alignment of these elements that are separated by spacers, and then bond these elements together. Whereby stack height can several mm high, consisting out of multiple multi beam elements.

Although there are methods and tools described in literature to align and bond electron optical MEMS elements [13,23,29–31] they either do not meet our requirements or are so poorly described/specific that the methods can hardly be applied to our challenges.
As the authors are not aware of any commercially suitable solution for these particular challenges, a novel versatile alignment tool for sub-micron alignment of electron optical MEMS/NEMS elements was build out of as much as possible commercial available components.

The objective of this chapter is to discuss the needed requirements, design choices that were made and describe the novel alignment tool that is able to align and stack electron optical elements with sub micron precision. First the requirements, envisioned alignment procedure and typical design choices that go with this are discussed. In order to demonstrate the precision of the alignment, wafers with venire structures were fabricated, aligned and bonded with a particular adhesive. To demonstrate the versatility of the tool the alignment of a multi beam electron gun module [16] is discussed.

Requirements and alignment tool design choices

In this section we discuss the needed alignment tool requirements, envisioned alignment procedure and typical design choices, keeping in mind that we want to be able to make multi beam electron optical stacks such as the multi beam rotation corrector [19].
The lateral alignment accuracy must be sub-micron to full-fill our rule of thumb for the multi beam rotation corrector [19,32], for array sizes of 1.5x1.5mm. The positioning accuracy in height is less strict, but still needs to be at least 5 μm or better.
The fixation should be possible with adhesive bonding, without loss of alignment due to polymerization or capillary forces.
Stacks of at least 1.35 mm high and lateral sizes of 1.5x1.5 mm must be stackable, preferably higher and wider.
Additionally the alignment tool must be suited to accept components of various shapes and sizes, but also larger macroscopic column parts such as an electron emitters.
Last but not least important, due to lack in funds and time we want to use as much as possible commercial position tooling.
We summarize, the minimum of movement steps required:

- x,y: <1μm (lateral)
- z : 5μm (height)
- θ: 1.3 < mRad (rotation around lateral axis)
- ϒ,ϑ: 3.3 mRad (pitch and yaw)
-

Before we can discuss a design that may comply with these requirements, it is necessary to describe the principle of the alignment procedure (which parts are moving, how to determine proper alignment, etc.), because the procedure will determine the tool.

We have chosen an alignment procedure that is based on positioning each element in turn in a fixed image plane of a light microscope. This envisioned procedure is illustrated in figure 3 that aligns two elements.

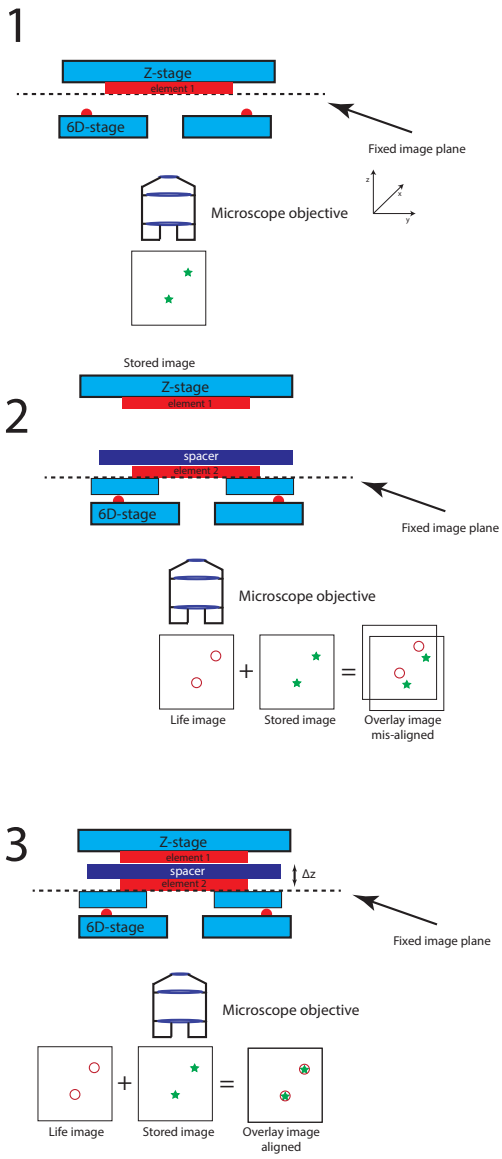

Figure 3: Alignment procedure to stack two multi beam lens arrays, with appropriate alignment markers. The shown markers are for illustrative purpose and are not the real markers used. In step 1); Element 1 is positioned on a vacuum chuck fixed to the z-stage. Element 1 is then brought into the image plane of the objective whereby a digitized image is stored in the computer. Step 2); The z-stage with element 1 is moved up a known distance to make space available for inserting the lower element 2 in combination with a prefixed electrical isolating spacers on a vacuum chuck on a kinematic mount on the 6D stage (stands for 6 axis of freedom stage, x,y,z, plus rotation axes). The system is set in such a way that element 2 is directly positioned in the image plane of the objective and is imaged live on the computer in combination with an overlay of the stored image of element 1. Step 3); The live image of element 2 and stored imaged of element 1 are aligned by moving element 2 with the 6D stage. Element 1 is positioned Δz from the image plane and bonded with an adhesive. After the polymerization this stack can be picked up by the z-stage. The bottom of the former elements 2 is now function as element 1 in step1 for the next element 2 to be stacked.

The fixed microscope image plane, and moving the elements to this plane, is an important design choice. In an alternative method, where the image plane is moved to stationary elements in the z-direction, some kind of mechanical manipulator needs to be used to move the whole microscope with cables, camera, etc.. Theoretically, in this process the optical axis could remain perpendicular to the sample and the microscope could be moved in a straight line, resulting in a stable position of the object in the image plane. In practice, however, position errors occur due to misaligned optics, non-linear strain in cabling and non-rectilinear motion, as illustrated in figure 4.

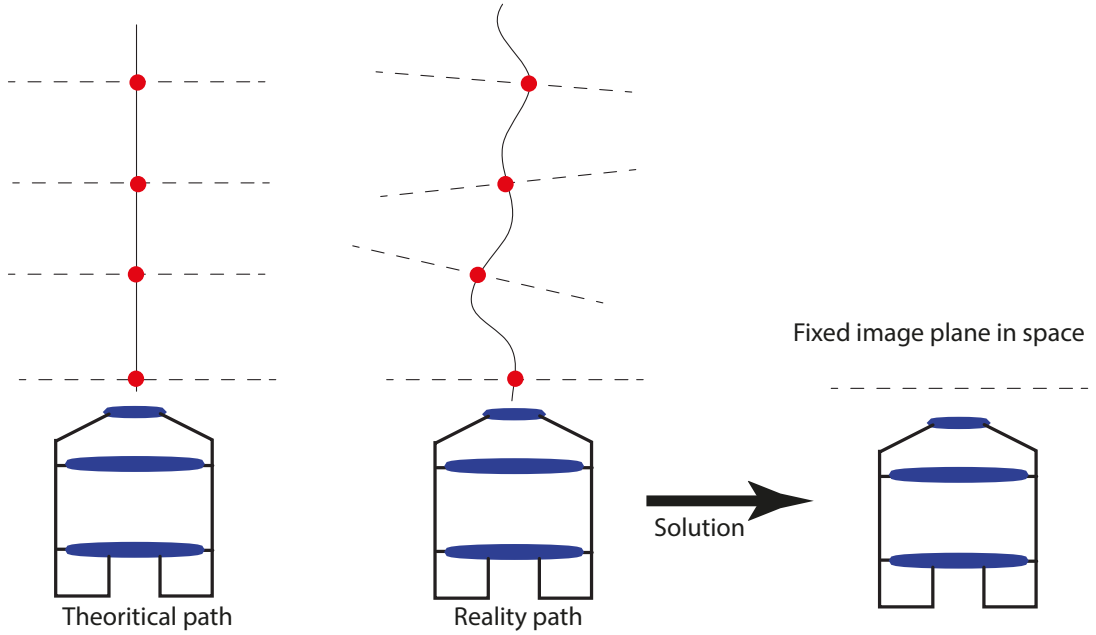

Figure 4: Left) Ideal straight path, without deviations. Middle) Path in reality with simple mechanical focus adjustment. Right) Solution with a fixed objective.

In our procedure the microscope is stationary in space, and the fixed image plane defines a single reference plane to which all elements to be aligned can be referred. By doing this we have shifted the problem to the z-stage to which element 1 is fixed. We believe that the lateral error is then easier to control, because high linearity precision stage are widely available that can handle small loads such as our elements. To our knowledge stationary image plane has never been applied before in stacking alignment.

In the alignment procedure element 1 is moved up to make space to insert element 2 and is afterwards lowered on top of element 2. Note that element 1 is not returned to the fixed image plane, but to a plane at a distance Δz (equal to the thickness of element 2 + spacer) above the stationary image plane (as indicated in figure 3) at a position. When the z-axis of motion of the upper element is perpendicular to the surface of the lower element, no lateral (Δx, Δy) displacement errors will be present after

alignment. However when it is not exactly perpendicular lateral movement errors will occur given a small lateral (Δx, Δy) displacement between the two elements after alignment. To correct this possible lateral displacement error some kind of monitoring between the 6D-stage and the z-stage is needed. Capacitance sensors are in this case a good and simple solution.

In our design where we use capacitance sensors particular attention is needed for the reference sensor planes, which need to be perpendicular to element 1, as can been seen in figure 5 where the error of movement direction is exaggerated. This specification for the tolerable error on perpendicularity can be calculated from the rule of thumb error that was set on 1µm divided by the maximum stack height of 1.35mm, giving a maximum error of 0.7mRad.

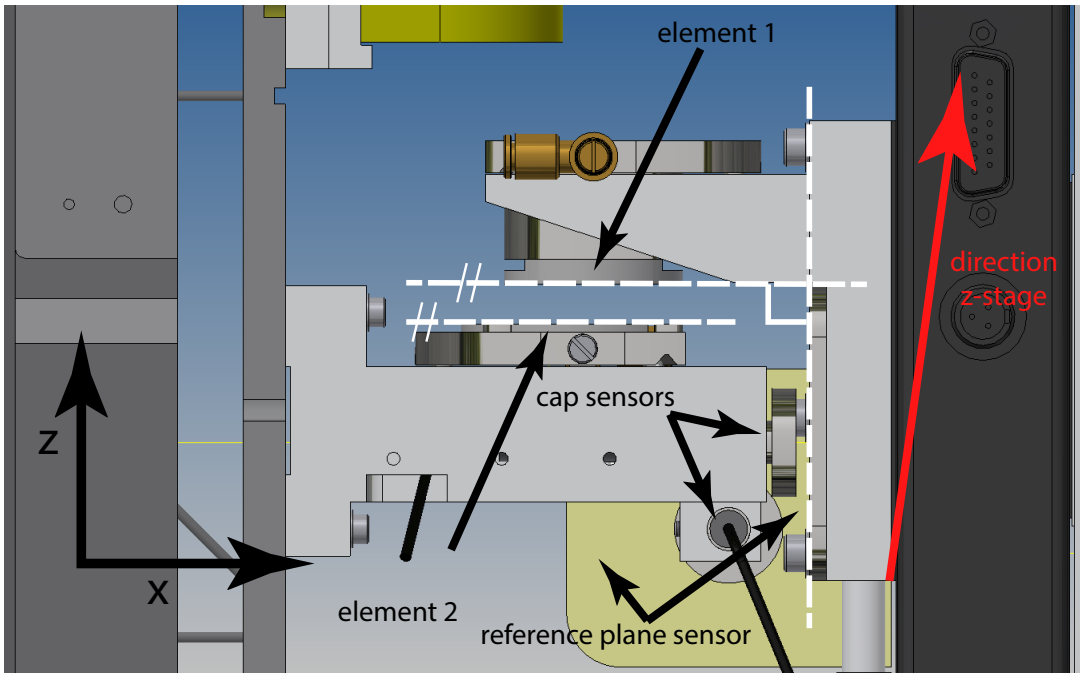

Figure 5: 3D CAD drawing of the alignment system to visualize the capacitance sensors and reference planes. For illustrating purpose we have drawn the parallel and perpendicular lines that correspond to the chuck surfaces and reference sensor planes.

The reader must have noticed that in the above design of the alignment procedure there was no mention of a pitch or jaw alignment of the elements. This would assume that the two elements were already sufficiently parallel to each other. If this is not the case, a pre-alignment needs to be conducted. The optical microscope does not have sufficient sensitivity to see small defocus gradients over the field of view, thus we use the following procedure.

It is assumed that the opposing surfaces of the elements to be aligned are flat enough. In the case of Si wafers that we typically use, wafer bow and thickness variations should be

less than 15 µm over a dice size of 20x20 mm^2. This translates to a maximum angle error in parallelism of 0.75 mRad in θ and ϕ when all other components are parallel. To adjust the parallelism between the elements, the angles between the elements are measured by determining the height difference between the elements at two different x/y locations on element 2, as sketched in figure 6.
After the the θ, ϕ angles are corrected with the 6D-stage, the measurement and correction is repeated till no further improvement can be obtained.

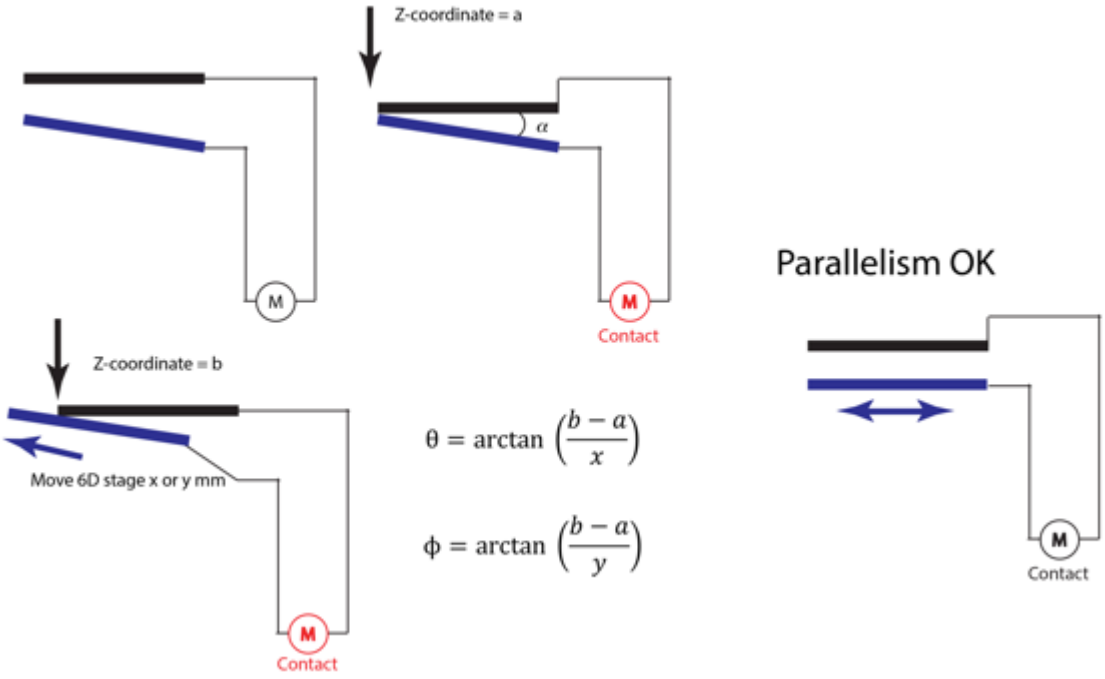

Figure 6: Determination and correction of the θ, ϕ angles between two elements by measuring the height at which the elements make electrical contact for two x positions and two y positions of the 6D-stage that holds the lower element. The two height coordinates found are z=a and z=b.

New Alignment tool

The new tool makes use of commercially available high precision stages that allow us to move parts over a range of several millimeters with smallest incremental motion steps of 100 nm.
The *z*-stage is a PI M605-1D closed loop linear stage (see figure 7) with a total travel range of 25 mm and minimal incremental motion of 300 nm. Maximum pitch and yaw displacement over the full range of motion is +/- 30 µRad. (For the full specification see the website of Physik Instrumente [33]). The 6D-
stage is a PI F206 hexapod stage (see figure 7 and 8) with a travel range of +/-5mm in the *x,y,*and *z* directions, and +/- 5 degrees in *θ, ϕ, γ,* with a smallest incremental motion of 100 nm and 2 µrad, all in closed loop motion. (For the full specification see the website of Physik instrumente [33]).

The optical detection system consists of a home-built inverted microscope with an interchangeable infinity corrected objective. Currently a Nikon 5x Plan Apo lens with an NA of 0.15 is used, but other infinity corrected lenses can be used as well. The objective lens is mounted on a manual focuser to adjust the focus of the objective when setting up the platform. After that the focus is kept fixed in the image plane as discussed above. The digital camera is an AVT Guppy F503, with 2592x1944 pixels and a pixel size of 2.2x2.2 μm^2. The optical system has been calibrated with a Thorlabs 1 mm stage calibration target, showing that one digital pixel corresponds to 870nm for the 5x lens.
The optical performance with the 5X lens has been tested with a standard USAF 1951 target whereby the smallest feature, group number 7 and element 6, could be easily resolved. This corresponds to a line width of 2.19 μm. The illumination and imaging paths are separated with a 50/50% half mirror block. The white light source and the computer are positioned approximately 3 meters away from the optical table to prevent thermal fluctuations and vibrations. All optical components other than the objective lens and the camera are standard Thorlabs parts.
The elements to be aligned are positioned on vacuum chucks (see figure 7 and 8), to make sure that they will not shift during the alignment procedure. These chucks are custom made for 20x20 mm^2 elements, but can also be easily adapted to elements having a different size. An element can be positioned on the 20x20 mm^2 chuck with a precision of +/-50 μm and an in-plane orientation accuracy of better than 5mRad. The chucks are positioned on sapphire spheres that form a kinematic mount on forks that are permanently mounted to the stages. The contact areas of the vacuum chucks have been polished with a flatness specification of 0.005 mm and roughness of 0.4 μm. This construction should guarantee a high chuck position repeatability (removing and placing back the chuck). Although gravity provides enough force to hold the chucks in place, the tubing of the vacuum lines may displace the chucks. We have increased the holding force by adding eight strong Neodymium disk magnets in both the chucks and the forks (see figure 9).
The stages are mounted on heavy precisely shaped granite blocks that are placed on an air damped optical table. All machined components are made with tolerances of at most 0.01 mm.
To minimize the influence of dust particles, temperature instabilities and floor and acoustic vibrations, the optical table with the alignment tool is placed on a special low vibration floor in a class 10000 clean room, with an 0.1 degree/hour temperature stability at the tool position.

The capacitance sensors are PI D510.101 extended range capacitance sensors, with a measurement range of 750 μm and a sensor resolution of 7.5 nm [33].The sensor reference planes were machined with a tolerance of 0.005 mm. Furthermore, the perpendicularity error between the upper chuck surface and the sensor reference planes, crucial for proper functioning of the z-tracking, was measured after fabrication, using a

hair line try square, with no visible error, convincing us that the error is much lower than the allowed 0.7 mRad, see figure 5 for more detailed image.

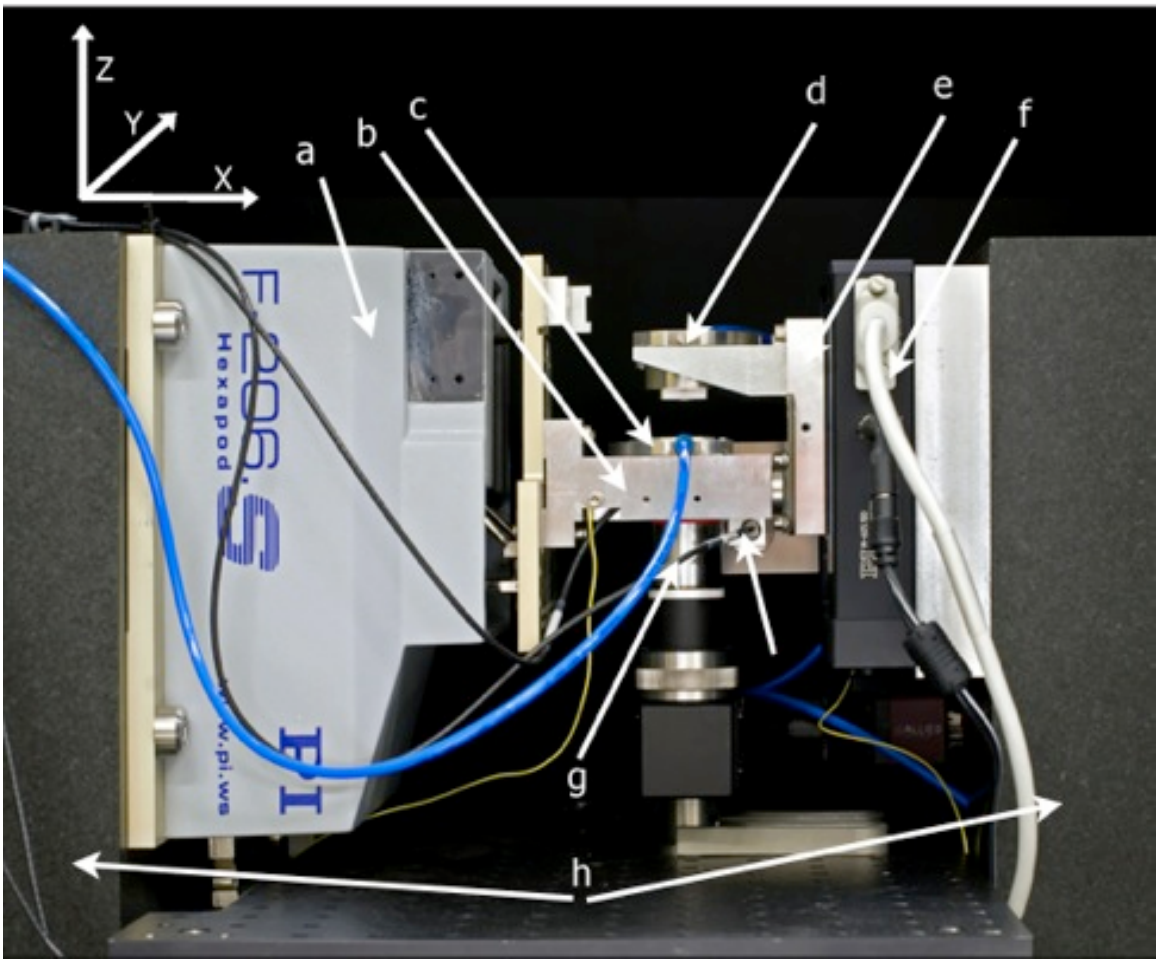

Figure 7: a) The 6D-stage (PI F206 hexapod), b) 6D-stage mounting fork, c) lower element chuck, d) upper element chuck, e) z-stage mounting fork, f) z-stage (PI M605-1D), g) microscope objective and h) granite stage mounting blocks.

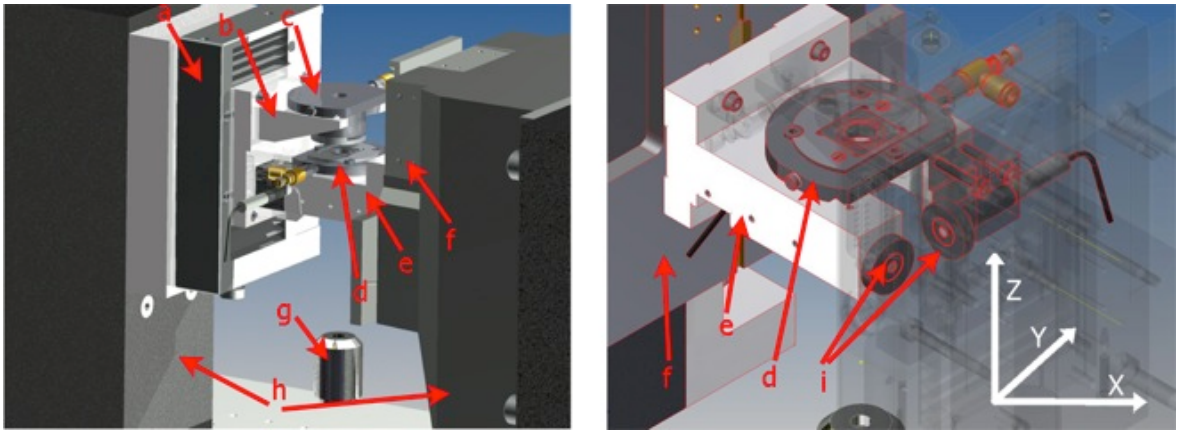

Figure 8: a) z-stage, b) z-stage mounting fork, c) upper element chuck, d) lower element chuck, e) 6D-stage mounting fork, f) 6D-stage, g) microscope objective drawn as floating element, h) granite stage mounting blocks and i) capacitance sensors for relative lateral displacement measurement between the 6D-stage and the z-stage.

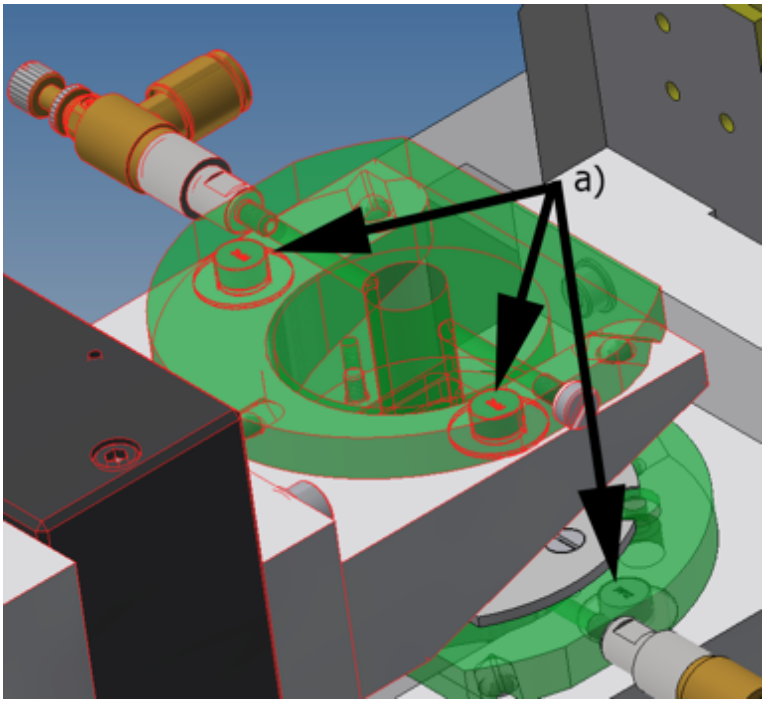

Figure 9: a) The clamping magnets in the chucks. For all four magnets in a chuck there is a counter magnet in the mounting fork.

The control of the system, i.e. the imaging and the movements, is implemented using the Labview software package. Alignment is currently done manually by matching and overlaying the stored image of element 1 and the live image of element 2 moving the 6D-stage, as described in the alignment procedure of figure 3. Figure 10 shows an example of two multi beam aperture arrays that are aligned with that procedure.

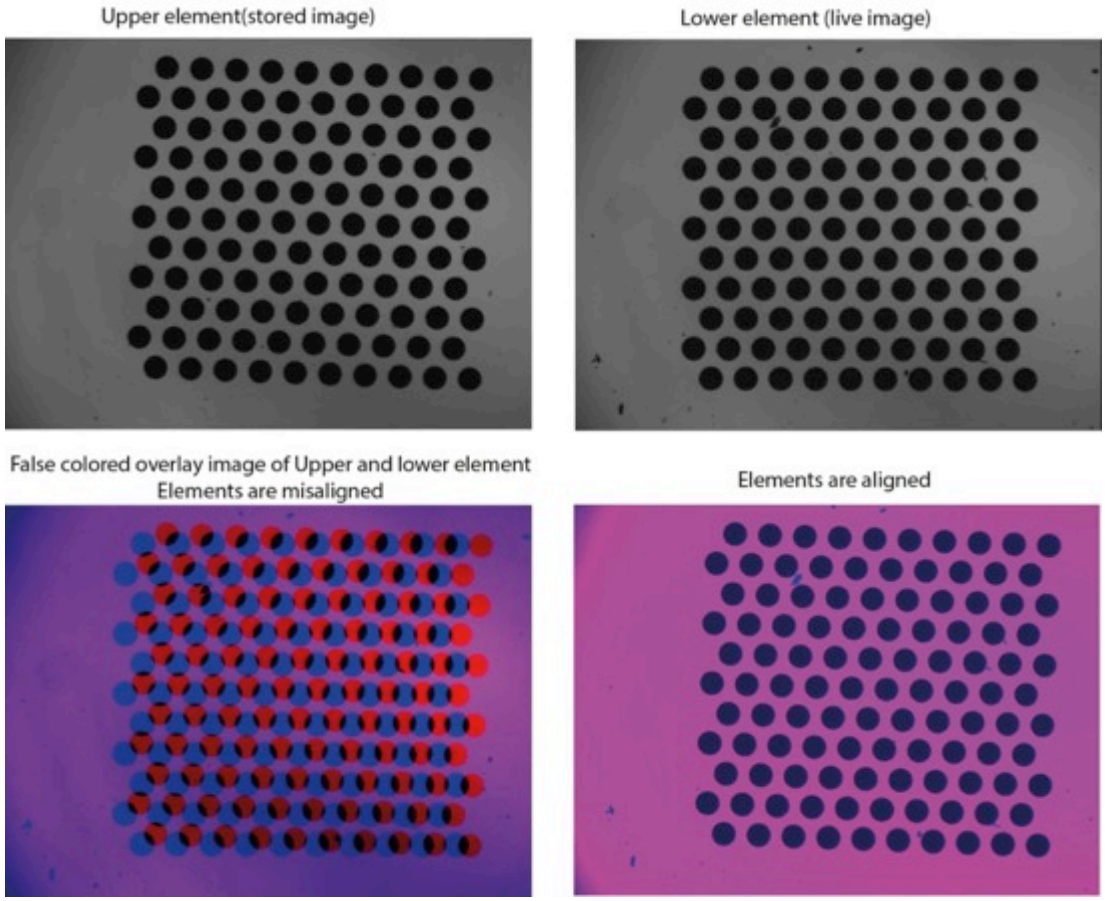

Figure 10: Upper grayscale images are the images as imaged with the camera. The false colored image is the overlay of both upper images, where element 1 is positioned on the z-stage (false color pink) and is stored in memory, and element 2 is positioned on the 6D-stage and is imaged live (false color blue).

Tool validation

The lateral displacement between the two stages when the z-stage is moved, as measured with the capacitance sensors, is plotted in figure 11 for the x and y direction. We would like to refer back to the section where we discussed the essential requirement of the sensor planes and the chuck of element 1. This difference could be expected, which is a

the deviation from perpendicularity in the two directions x and y. In the x-direction the deviation angle is 0.4 mRad and in the y-direction it is 1mRad. What is expected since the fork in the x-direction is on the z-stage construct what is well determined plane. On the other hand the y-direction in only determined with its fixing screws, giving bigger errors.

From a practical point of view it means that for small z-movements, such as the typical spacing between two multi beam array electrodes of 500 µm, no corrections for lateral shifts have to be done to fulfill the sub-micron alignment goal. Nevertheless, the lateral displacements can be measured and can be corrected for during alignment if required.

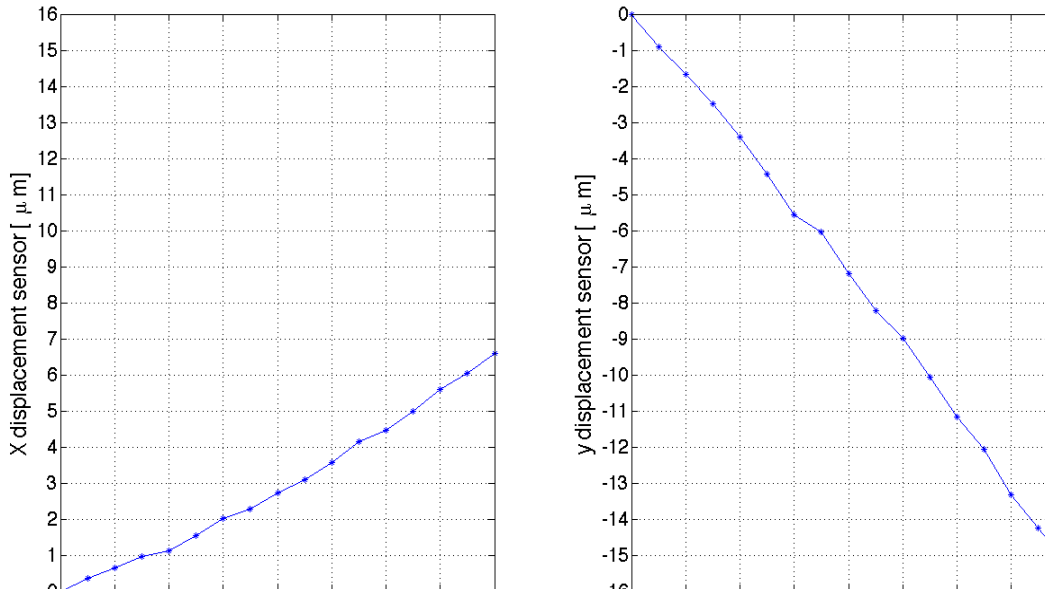

Figure 11: Lateral displacement errors of the z-stage, due to the z stage movement being not perpendicular to the element surface: left) displacement in the x-direction, right) displacement in the y-direction.

To test the alignment tool samples were made consisting of venire structures on silicon wafer dices and on a glass wafer dices. These samples were adhesively bonded with the venire structures in the same plane to facilitate inspection afterwards. The venire alignment structures are designed in such a way that it is possible to optically inspect the alignment in x and y of a central cross with an accuracy of +/-200 nm and to calculate the rotation misalignment γ up to +/- 0.5 mRad. Figure 12 shows the basic setup and the test sample layout when the glass and silicon sample are bonded.

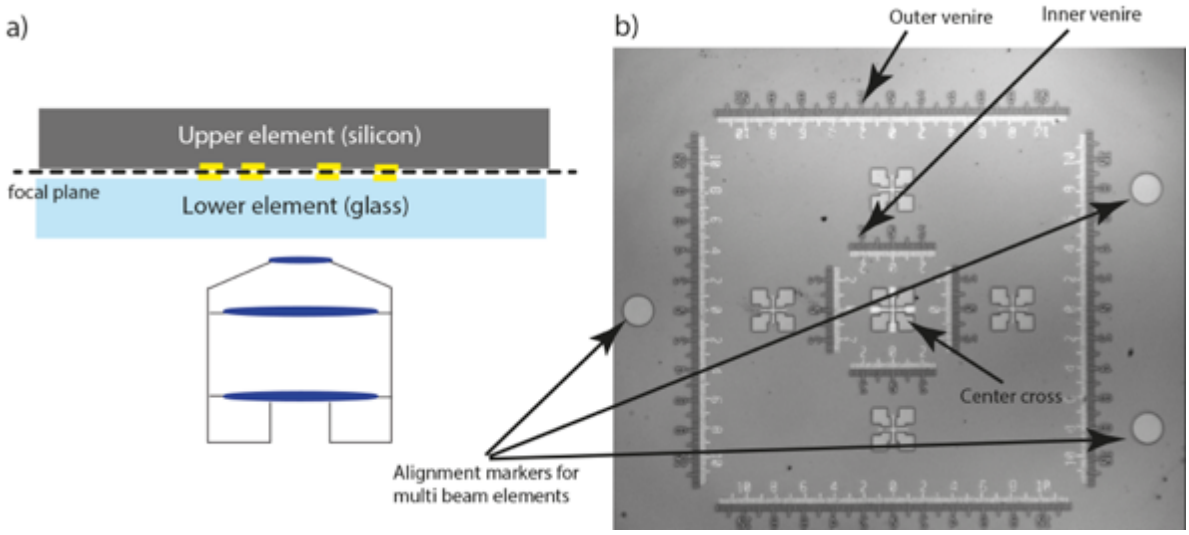

Figure 12: a) Sketch of the silicon and glass sample in contact. The venire structures are shown in yellow. b) Image of a stacked test sample. The dark patterns are on the silicon substrate and the white patterns are on the glass substrate. The outer venire has a step of 250 nm miss-alignment per bar and inner venire has a step of 200 nm misalignment per bar. The circular alignment marks visible are the marks that will be used later for the alignment of multi beam elements.

The alignment procedure sketched in Figure assumes that there are no lateral forces involved during polymerization of the adhesive. That could else lead to unwanted displacement of the elements, and which would remain unnoticed till final inspection of the bonded stack. There are a number of studies in literature on adhesive bonding [34] and the forces involved when bringing two elements in contact with an adhesive before the polymerization occurs [35,36]. What is rarely mentioned in literature [34] is that, although the initial misalignment can be sub-micron, the misalignment will increase significantly during polymerization of the adhesive. Elaborate schemes exist to reduce these errors [37], but this requires special spin-coated adhesive layers of uniform

thickness and those adhesives are unfortunately not suited for the applications described here.

There are two important requirements to the adhesives that apply here. First of all the adhesive has to be vacuum compatible (pressure $<10^{-7}$ mbar) and secondly adhesives near apertures cannot be tolerated because that will cause beam deflection due to charging of the adhesive. The forbidden areas are indicated in the left hand sketch of Figure 13. The adhesive that fulfills the requirements is proprietary glue supplied by MAPPER lithography BV with an air curing time of 12 hours.

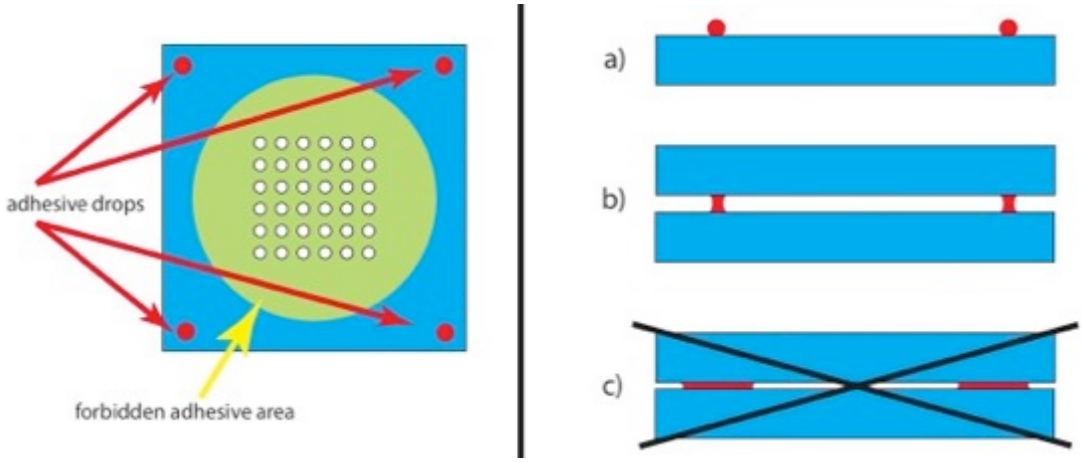

Figure 13: Left: forbidden area and the sites for the droplets of adhesive. Right: separation distance between elements. Right: a) lower element with adhesive droplets. b) lower and upper element both in contact with the adhesive. c) lower and upper element are in too close contact, making it impossible to maintain the alignment during polymerization.

To avoid adhesive in the forbidden areas, small droplets were applied at the 4 corners of the dice with a droplet volume of approximately 100 nano-liters, using a pipette. Droplets applied with an extremely sharp glass needle gave even smaller droplets, but with less well-controlled volume. Instead of pushing the elements together with the z-stage, as done in most bonding techniques, and then disengaging the vacuum of the upper chuck, during the polymerization phase of approximately 12 hours the two elements are kept at an intended separation of the order of 30-40 µm, just enough to have adhesive contact between both elements, as shown on the right hand side of Figure 13. This gives two benefits. Firstly the adhesive will not flow to the forbidden area when the elements are bonded, and secondly the separation helps to reduce the misalignment during polymerization. Figure 14 shows the experimental results of restricting the adhesive to small areas and the spacing left after polymerization.

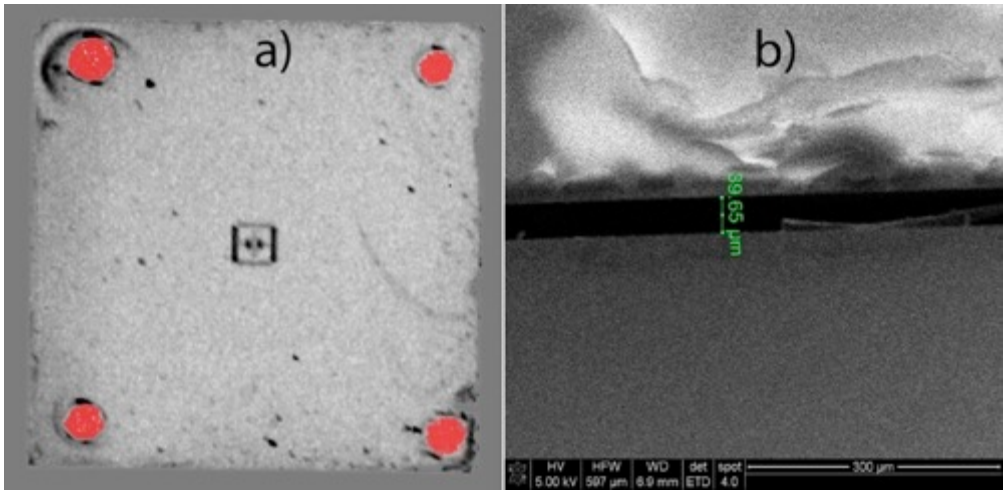

Figure 14: a) Enhanced image of a transparent test sample that was adhesively bonded on a silicon test sample. Red false-colored spots are the adhesive droplets after polymerization, illustrating the control over the adhesive positioning during bonding. b) SEM image of a broken test sample, showing the gap that is left between the elements after polymerization of the adhesive droplets. Upper white is the glass test sample and the lower dark is the silicon test sample.

Figure 15 shows a typical result obtained by aligning the inner venires and keeping a separation between the elements during polymerization. The misalignment between the elements is smaller than 500 nm, i.e. well below the sub-micron goal. To the best knowledge of the authors this is the world record for alignment with adhesive bonding at the time of writing. Although successful sub-micron alignment was achieved using adhesive bonding, the authors note that other methods exist for bonding elements. For instance Mohaupt et al. [31] describe a stacking and bonding tool for multi beam array elements that makes use of soldering bumps, also claiming sub-micron alignment, without any visible proof.

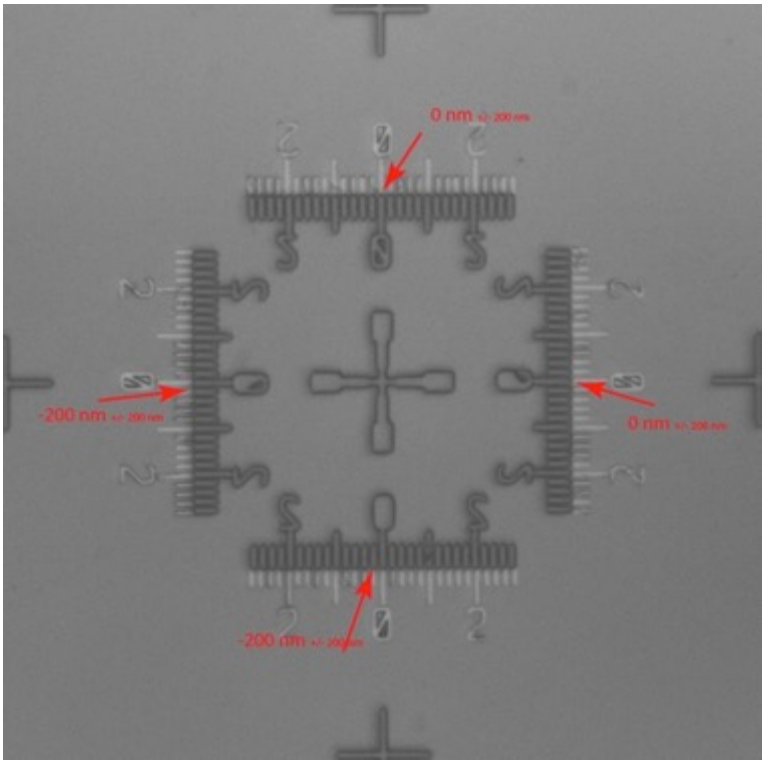

Figure 15: Adhesive bonded test elements with sub 500 nm misalignment after polymerization.

To test the alignment accuracy of electron optical elements, having different patterns on both elements, six tests were conducted with alignment of markers designed for the multi beam aperture array electrodes (see figure 12). After alignment of these markers the misalignment was quantified with the help of similar venire structures as shown in figure 15. The results are shown in Figure 16.

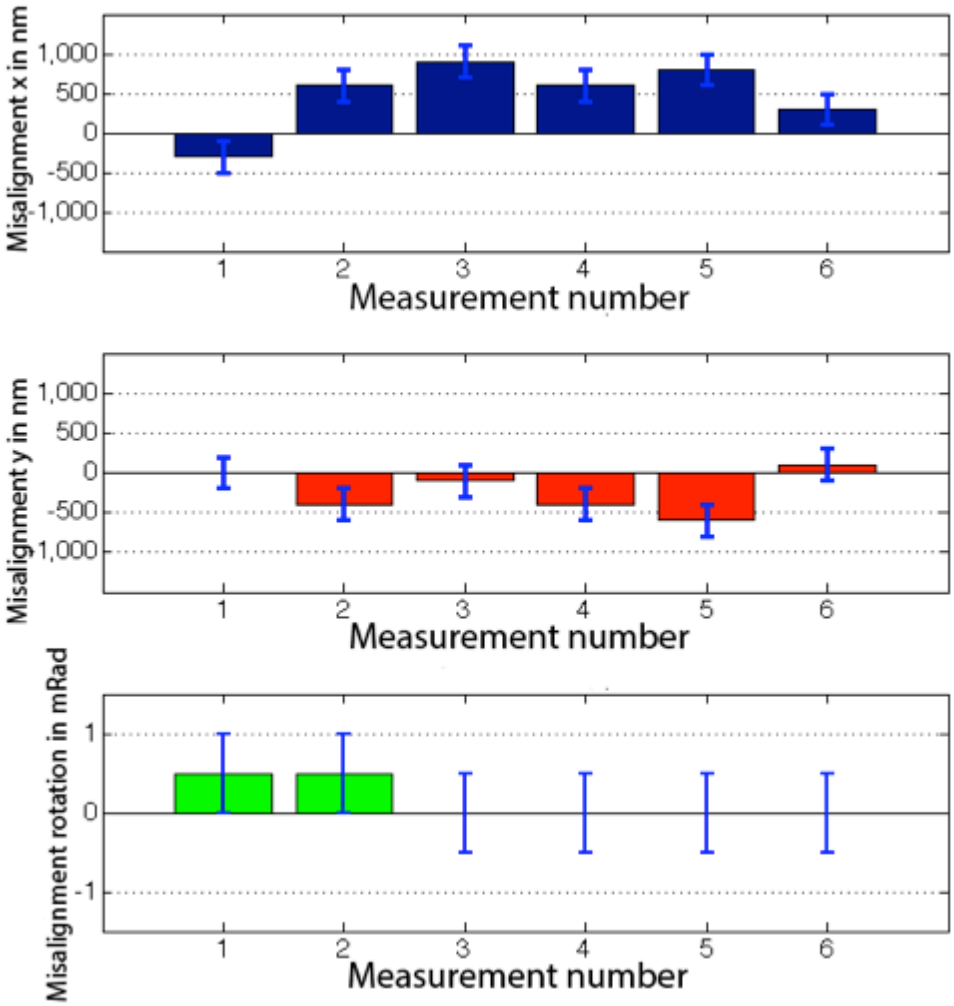

Figure 16: Misalignment in the x and y direction of the center cross and the rotation angle error. These results were obtained by using the multi beam alignment markers for alignment and inspection afterwards of the inner verniers. In total six verification experiments were conducted, demonstarting that sub-micron alignment with these marker structures is possible. The horizontal axis is the measurement number.

Alignment of larger components

One of the design criteria was that the tool should be suited for a wider range of alignment applications. As an example the tool was used to determine the alignment of two apertures positioned at different heights in a multi electron beam source module [16]. The 6D-stage is extremely well suited for this purpose, making use of the possibility to move the 6D-stage perpendicular to the focus plane of the objective. The procedure is sketched in Figure 16. After positioning the source module on the lower vacuum chuck, one of the apertures of electrode 1 or 2 (red electrodes in figure 16) is brought into focus and the center of the aperture was determined. The next step is to move a small step up or down, whereby the image of the aperture becomes defocussed. If the z-movement was perpendicular to the focus plane the determination of the center of the aperture in the defocused image should give the same value as in the focused image. When a shift is observed the tilt and/or yaw of the 6D-stage has to be adjusted, and the procedure is repeated till the result is satisfactory. Then the upper part of the module, with the field emission source and the extractor electrode (green electrode in figure 17) is brought in focus and the center of the extraction electrode aperture is determined. When the center coordinates of both apertures coincide then the alignment is within +/-5 µm. If not, then the upper part of the module needs to be adjusted using alignment screws. The accuracy could be improved by developing automated image recognition software, but this was not necessary in this application.

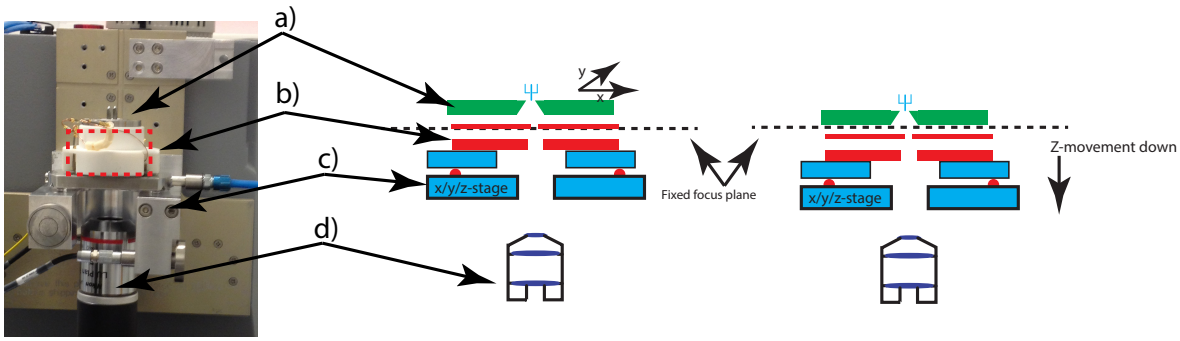

Figure 17: Alignment of a field emission electron (FEG) source and extractor assembly onto electrode 1 and 2 assembly. The lateral alignment of the FEG and extractor assembly can be adjusted with small screws. By first detecting the center of the circular aperture of electrode 1 or 2 the 6D-stage moves the gun assembly down such that the center of the aperture of the extractor can be determined, if needed the alignment is adjusted with the screws. a) In green FEG with extractor. b) In red Electrode 1 and 2 assembly. c) In blue 6D-stage stage, fork and vacuum chuck. d) Microscope objective.

Discussion

Due to its flexible design and its placement on an optical table the alignment tool can be updated and/or modified easily for all kinds of different alignment tasks and/or other strategies. The first improvement we would implement is to use pattern recognition software to determine the positions of the alignment features and to do automated alignment instead of manual alignment, taking out the human factor. Computation techniques that can detect these features with an accuracy of at least 1/10 of a image pixel [38] are nowadays widely available and could easily be implemented in the Labview software.
On the mechanical side more detail could go in the design and fabrication of the vacuum chucks. Currently the elements are bended due to the vacuum clamping that is clearly visible by human eye. This gives predictable deformations of the elements after alignment, since we release the vacuum clamping after polymerization. The simplest improvement is to make more vacuum channels instead of one big one, as in the current design.
We have used one particular adhesive that has a relatively long polymerization time, but there are other options, some already mentioned such as bump soldering[31]. Not mentioned is for example the option to use UV-light curable adhesives for example. Attention and experimental research need to be conducted to the miss-alignments induced by polymerization effects with other adhesives. We could also think about a different method to determine proper alignment for example as done by S. Ahn et al[29], by using a laser and a diffraction disk image.

Conclusion

In conclusion, we have designed, built and tested an alignment tool that is suited for multi electron beam MEMS component stacking and bonding. The tool is able to do sub micron alignment stacking with adhesive bonding after polymerization. The tool can be used for a wider variety of MEMS elements stacking and bonding and can easily be adapted due to its modular design. Making it suitable for university research were size, shapes etc. of such multi beam are not fixed components.

Acknowledgements:
This works has been funded by the NanoNext program and by Mapper lithography bv. We would like to thank C. Barend , G.Schotte † and J. de Looff for the fabrication and technical support, F. Berwald for the help and advise in programming the Labview interface, J.Nonhebel and H. van der Linden for their help in the electronics and ALT and Physik Instrumente(PI) for their advice and time to find a suitable and affordable stage. Guido Rademaker for supplying the SEM images of the NAIS. Y. Ren and D. Morsing for the 3D images of the multi beam components.

References:

[1] H. Li, C.X. Luo, H. Ji, Q. Ouyang, Y. Chen, (2008) 100871.
[2] N. Barbour, G. Schmidt, IEEE Sens. J. 1 (2001) 332.
[3] P. Abgrall, a-M. Gué, J. Micromechanics Microengineering 17 (2007) R15.
[4] N. Miki, X. Zhang, R. Khanna, A.A. Ayo, D. Ward, S.M. Spearing, 103 (2003) 194.
[5] ITRS, www.itrs.gov
[6] C.-T. Ko, K.-N. Chen, Microelectron. Reliab. 50 (2010) 481.
[7] M. Wiemer, M. Haubold, C. Jia, D. Wuensch, J. Froemel, T. Gessner, ECS Trans. 16 (2008) 81.
[8] M.J. Wieland, Proc. SPIE 7637 (2010) 76371Z.
[9] Y. Zhang, A 100-Electron-Beam Source from a High Brightnes Schottky Emitter for Fast Patterning Applications, Delft University of Technology, 2008.
[10] E. Platzgummer, in:, D.J.C. Herr (Ed.), Proc. SPIE, 2010, p. 763703.
[11] Y. Zhang, C.T.H. Heerkens, M.J. van Bruggen, P. Kruit, J. Vac. Sci. Technol. B Microelectron. Nanom. Struct. 24 (2006) 2857.
[12] P. Kruit, Microelectron. Eng. 84 (2007) 1027.
[13] H.L. Ã, C. Klein, E. Platzgummer, 49 (2010) 1.
[14] G. Winograd, V. Krishnamurthi, R. Garcia, L.H. Veneklasen, M. Mankos, F. Pease, J. Vac. Sci. Technol. B 18 (2000) 3052.
[15] M.J.J. van Bruggen, B. van Someren, P. Kruit, Microelectron. Eng. 83 (2006) 771.
[16] A. Mohammadi-Gheidari, C.W. Hagen, P. Kruit, J. Vac. Sci. Technol. B 28 (2010) C6G5.
[17] A. Mohammadi-Gheidari, P. Kruit, in:, Nucl. Instruments Methods Phys. Res. Sect. A, Elsevier, 2011, pp. 234–240.
[18] Y. Zhang, P. Kruit, Phys. Procedia 1 (2008) 553.
[19] A.C. Zonnevylle, C.T.H. Heerkens, P. Kruit, M.L. Wieland, F.M. Postma, S.W.K.H. Steenbrink, Microelectron. Eng. 87 (2010) 1095.
[20] H.S. Kim, D.Y.W.Y. Kim, S. Ahn, Y.C. Kim, J. Cho, S.K. Choi, D.Y.W.Y. Kim, Microelectron. Eng. 78-79 (2005) 55.
[21] A.C. Zonnevylle, C.T.H.T.H. Heerkens, C.W.W. Hagen, P. Kruit, Microelectron. Eng. 123 (2014) 140.
[22] T.H.P. Chang, J. Vac. Sci. Technol. B 10 (1992) 2743.
[23] C. Klein, J. Klikovits, L. Szikszai, E. Platzgummer, H. Loeschner, Microelectron. Eng. 87 (2010) 1154.
[24] S. Eder Kapl, H. Loeschner, W. Piller, M. Witt, W. Pilz, F. Letzkus, M. Jurisch, M. Irmscher, E. Platzgummer, J. Micromechanics Microengineering 21 (2011) 045038.
[25] M. Wieland, H. Derks, Proc. SPIE (2010).
[26] M.A. Mccord, P. Petric, U. Ummethala, A. Carroll, S. Kojima, L. Grella, S. Shriyan, C.T. Rettner, C.F. Bevis, O.T. Drive, Proc. SPIE 8323 (2012) 1.
[27] D.S. Jun, V.G. Kutchoukov, P. Kruit, J. Vac. Sci. Technol. B 29 (2011) 06F603.

[28] D.S. Jun, V.G. Kutchoukov, C.T.H. Heerkens, P. Kruit, Microelectron. Eng. 97 (2012) 134.
[29] S.J.S.J. Ahn, H.S. Kim, S.J.S.J. Ahn, Mater. Sci. Forum 695 (2011) 589.
[30] M. Mohaupt, R. Eberhardt, C. Damm, T. Peschel, A. Tunnermann, E. Haugeneder, H.J. Doring, C. Brandstatter, Microelectron. Eng. 83 (2006) 980.
[31] M. Mohaupt, E. Beckert, T. Burkhardt, M. Hornaff, C. Damm, R. Eberhardt, A. Tünnermann, H.J. Döring, K. Reimer, Precis. Assem. Technol. Syst. IFIP Adv. Inf. Commun. Technol. 371 AICT (2012) 42.
[32] A.C. Zonnevylle, T. Verduin, C.W. Hagen, P. Kruit, J. Vac. Sci. Technol. B 31 (2013) 06F702.
[33] Physik instruments, (n.d.).
[34] F. Niklaus, G. Stemme, J.Q. Lu, R.J. Gutmann, J. Appl. Phys. 99 (2006) 031101.
[35] W. Washburn, Phys. Rev. Lett. 17 (1921).
[36] E.J. De Souza, M. Brinkmann, C. Mohrdieck, E. Arzt, Langmuir 24 (2008) 8813.
[37] F. Niklaus, R.J. Kumar, J.J. McMahon, J. Yu, J.-Q. Lu, T.S. Cale, R.J. Gutmann, J. Electrochem. Soc. 153 (2006) G291.
[38] T.Q. Pham, M. Bezuijen, L.J. Van Vliet, K. Schutte, C.L.L. Hendriks, in:, Proc. SPIE, 2005, pp. 133–144.

Ch. 6 Integration of a high-NA light microscope in a Scanning Electron Microscope

Authors: A. C. Zonnevylle, R. F. C. v Tol, N. Liv, A.C. Narvaez, A. P. J. Effting, P. Kruit, and J. P. Hoogenboom

This chapter has been published in: Zonnevylle et al., *Journal of Microscopy, Vol. 252, Issue 1 2013, pp. 58–70*

Abstract

We present an integrated light-electron microscope in which an inverted high-NA objective lens is positioned inside a scanning electron microscope (SEM). The SEM objective lens and the light objective lens have a common axis and focal plane, allowing high-resolution optical microscopy and scanning electron microscopy on the same area of a sample simultaneously. Components for light illumination and detection can be mounted outside the vacuum, enabling flexibility in the construction of the light microscope. The light objective lens can be positioned underneath the SEM objective lens during operation for sub-10 μm alignment of the fields of view of the light and electron microscopes. We demonstrate in-situ epi-fluorescence microscopy in the SEM with a numerical aperture of 1.4 using vacuum-compatible immersion oil. For a 40 nm diameter fluorescent polymer nanoparticle, an intensity profile with a FWHM of 380 nm is measured while the SEM performance is uncompromised. The integrated instrument may offer new possibilities for correlative light and electron microscopy in the life sciences as well as in physics and chemistry.

Introduction

Light microscopy gives both intensity and color contrast. Color contrast is most notably exploited in fluorescence microscopy, where a fluorescent molecule emits light in a specific, narrow spectral band that is wavelength-shifted with respect to the excitation light. The labeling of different individual proteins with different fluorescent marker molecules, either through immuno-labeling or by endogenous labeling, makes it possible to directly image the distributions of functional proteins[1]. One limitation of fluorescence microscopy is that the resolving power of the light microscope is limited by diffraction to approximately 300 nm. Another limitation is that it is only the labeled, functional components that are visualized while the underlying cellular ultrastructure remains invisible. Electron microscopy (EM) can on the other hand image the cellular ultrastructure with nanometer resolution[2] but gives no information on the function of the structures. By combining data from light microscopy (LM) and EM the protein distribution can be analyzed with respect to the cellular ultrastructure. This combination

is called correlative light and electron microscopy (CLEM). CLEM thus closes the gap between LM and EM by giving complementary functional and structural information from the same region of interest [3–7]. In recent years, CLEM has received increasing interest from the scientific community [8–17].

Generally speaking, there are two distinct ways of using CLEM. In early CLEM applications, the fluorescence microscope was merely used to help in the localization of a region of interest (ROI) for EM, based on the positions where labeled bio-molecules are expressed. These ROIs are then imaged at high resolution in the electron microscope. The information in the light image is not used for the detailed interpretation of the sample. Recently, CLEM applications increasingly rely on more advanced use of the fluorescence microscope, e.g., to identify (rare) bio-molecules in the cellular ultrastructure. In this approach, the resulting EM and fluorescence images are overlapped in detail after relative scaling and rotation. Here, it is important to have the highest possible resolution in the light microscope image. It may even be that the electron microscope image is only used to confirm certain conclusions drawn from the light image.

Typically, CLEM is done by transferring the sample from one microscope to the other. To avoid degradation of the fluorescence signal due to electron-beam exposure, the fluorescence image is recorded prior to EM. Retrieval of a region of interest in the electron microscope can however be complicated because light and electron microscopy have different contrast mechanisms. Markers on a sample holder [6], or in the sample itself[15,16], combined with automated recognition [18], may aid in ROI retrieval and image overlap procedures. Still, this is a time-consuming procedure, which makes quantitative analysis based on large data-sets cumbersome. Moreover, during transfer from one microscope to the other, the sample is vulnerable to change, modification, damage or contamination.

These problems are overcome in integrated systems, where both microscope types are combined in a single apparatus. The experimental time is drastically reduced as all issues related to finding back a ROI in the other microscope are removed from the CLEM procedure as soon as the relative coordinate systems are defined. In addition, contamination or sample damage due to transport between separate microscopes does not occur. Going back and forth between both modes of operation also becomes much easier.

In a system built by Wouters *et al*. in the 1980's [4,19,20], the light microscope was integrated in a scanning electron microscope (SEM) under an angle of 45° with respect to the SEM optical axis. An illumination lens for transmission-LM was added at the opposite side of the SEM objective lens. Although for its time an advanced instrument, this position of the light microscope does not allow the best resolution light microscopy, nor the highest resolution EM. It also complicates analytical electron backscatter imaging and, due to the 45° angle of the sample with respect to the electron axis, this system is incompatible with electrostatic sample immersion for a decelerating electric field. The

latter option is becoming increasingly important for biological EM as it enables nanometer resolution at low electron landing energy [21,22]. Finally, in the way it was constructed, accurate re-alignment of the light microscope in the SEM was not possible.

More recently, Nakamura and co-workers incorporated a fluorescence light microscope inside a dedicated SEM column [9]. Both the light microscope and the SEM illuminate the sample from above, where a hole drilled into the center of the light objective lens allows passage of the electron beam. A major advantage of this solution is that the fields of view of both microscopes are naturally aligned. However, due to the hole in the glass lens part of the light cone will be missing, and, importantly, the increased SEM working distance will lead to loss of resolution in the focused electron beam. In addition, the ability to do backscattered electron imaging will be reduced as a backscattered electron detector centered around the electron axis would block the optical lens. In addition, the light microscope operates at long working distance with a low NA lens.

Another recent development was reported by Nishiyama *et al.*[12,23,24]. Contrary to the other solutions, in their system the light microscope and the sample are not placed in vacuum but rather in air. In this microscope, called an atmospheric scanning electron microscope, the sample is imaged by the SEM through a thin membrane that separates the SEM vacuum chamber from the surrounding ambient atmosphere. The LM is positioned above the sample and the SEM, and can be a regular microscope, where even the use of a water-immersion objective is possible. Electron imaging through the thin membrane limits the EM resolution. Also, the observable area is limited because the membrane area is small in order to withstand the pressure difference. In addition, the analytical capabilities of the SEM are limited in this configuration.

Two systems have been presented for integrated light microscopy in the transmission electron microscope (TEM). Akashi Seisakusho Ltd. developed the LEM 2000, where the sample could be moved automatically between EM and LM. The light microscope was mounted on the side of the TEM. Jones *et al.* used this machine for the study of routine histopathology [25]. In this system simultaneous microscopy is not possible. Gerritsen and co-workers created an optical path to view a TEM sample while in position between the magnetic immersion objective lens [8]. Because of the limited space in between the pole pieces, the objective lens is inevitably long working distance and low numerical aperture (NA). In addition, the sample is rotated from LM to TEM, so simultaneous microscopy is not possible.

So, in the integrated systems presented to date, the integration poses limitations to either the performance of the light microscope or of the electron microscope, as compared to stand-alone microscopes. Thus, these systems may be very useful for the localization of a region of interest (ROI) in EM, based on the positions where labeled proteins are expressed, but to overlay high-resolution LM data onto information from EM, researchers still have to resort to the use of two separate microscopes. In order to fully profit from the analytical power of both types of microscopy in CLEM research, it is

crucial that the integration does not compromise the capabilities of either the light or the electron microscope. In principle, the sample could be moved fast between the electron microscopy position and the light microscopy position, but we judge that simultaneous imaging will ultimately lead to faster and more accurate CLEM and will moreover increase imaging capabilities with possibilities such as detection of cathodoluminescence [26] or simultaneous excitation by light and electrons. Thus, our goal is to build an integrated system without compromises, with the possibility to do simultaneous CLEM on the same region of interest.

This poses several challenges. For high-resolution fluorescence microscopy and for compatibility with advanced types of LM, such as confocal or super resolution microscopy, it should be possible in the integrated system to use a light objective lens with a large Numerical Aperture (NA). Compatibility with the use of (vacuum-compatible) immersion oils is also necessary. Ultimate resolution for the electron microscope means a short enough working distance between the objective lens and the sample to be able use a magnetic immersion objective. At the same time, integration should be performed in such a way that none of the illumination or detection paths of either microscope are obstructed. In addition, there should be flexibility in the construction of the light microscope illumination and detection paths so that optical components can be easily added or removed, e.g., to achieve spatial or spectral filtering. The integrated microscope should also hold sufficient degrees of freedom for independent focusing of both microscopes, for mutual alignment of the focal planes and optical axes of both microscopes, and for lateral sample translation.

Simultaneous imaging increases the demands on alignment of the objective lenses and on the materials used in the construction: for electron microscopy they must not be magnetic and the electron beam must be shielded from external magnetic fields and insulating surfaces. A final restriction we set ourselves in the design was that we did not want to design a new electron microscope or a new type of light microscope. In fact, we wanted to create as much as possible an interface to couple an existing electron microscope with an existing light microscope, or components thereof, with proven high-performance capabilities. In the next sections, we will first describe the technical implementation of this microscope, followed by validation results on its performance and a discussion on the applicability for correlative light and electron microscopy.

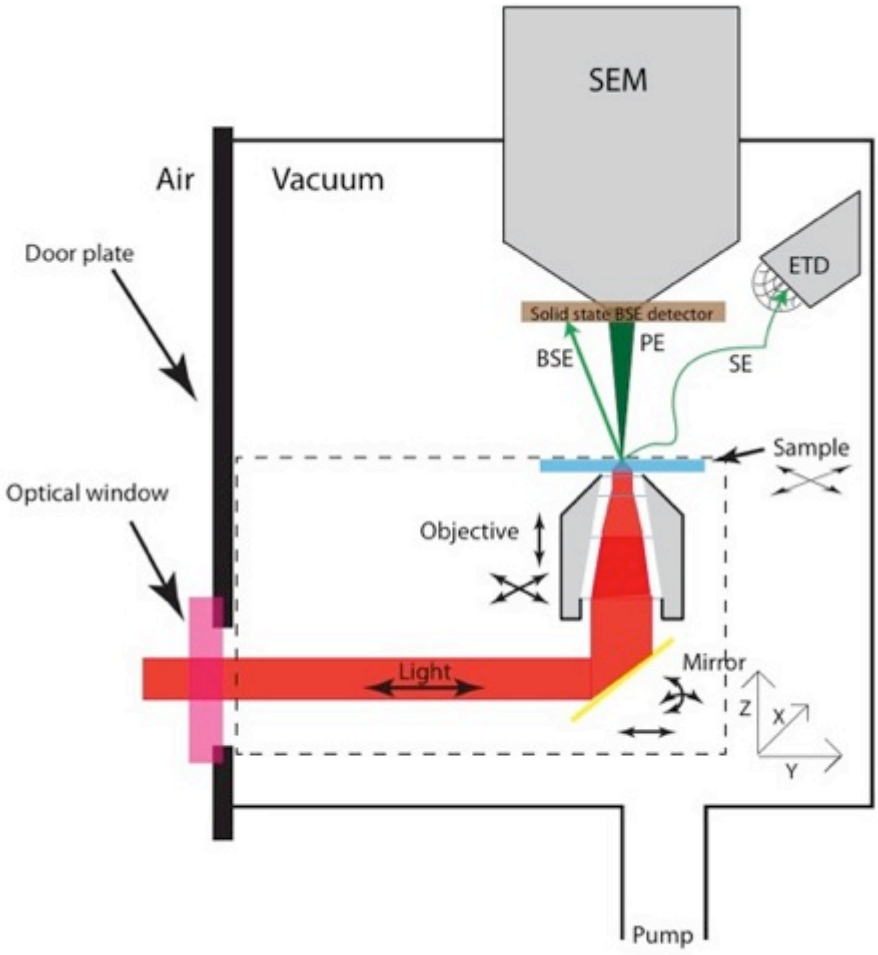

Figure 1: Schematic illustration of the system with an inverted light objective positioned in epi-configuration below the sample inside a SEM. All SEM functionality is contained in the half-space above the sample, while all light microscopic functionality is contained in the lower half-space. Additional components for optical illumination/detection are placed outside the vacuum. Directional two-way arrows indicate the required degrees of freedom for sample, objective, and mirror in order to perform SEM-LM alignment and sample navigation. The dashed box encircles all components that are mounted on the doorplate to the SEM vacuum chamber. PE: Primary Electrons; BSE: Back Scattered Electrons; SE: Secondary Electrons; ETD: Everhard-Thornley Detector.

Construction of the integrated microscope

In the design of the integrated microscope, we exploit the fact that the standard detectors in a SEM [26] are positioned in the half-space above the sample (see Figure 1). Conversely, the epi-fluorescent illumination and detection in an inverted light microscope occur in the half-space below the sample through a transparent cover glass onto which the sample is mounted. Thus, in the design illustrated in Figure 1, both

microscopes occupy opposing sides of the sample and can thus in principle be used in their regular, uncompromised mode of operation. Only the use of transmission detection in SEM and top illumination in LM is difficult, and, samples need to be thin and sufficiently transparent for the light microscope to reach the SEM image plane. Additional components, such as x-ray detectors or gas-deposition needles for EM and filters, and polarizers for LM, could be used provided they can be inserted in the corresponding half-space.

We have implemented the setup depicted in Figure 1 in a FEI Quanta 200 FEG using Nikon infinity-corrected CFI60 objective lenses. In the Quanta 200 FEG, the sample stage is mounted on the doorplate. This allows us to replace the door of the vacuum chamber with a new doorplate onto which the inverted LM and a new custom-designed sample stage are mounted. The sample is fixed on a *xy*-stage at a working distance of 5–10 mm below the electron objective lens. The light objective lens, additional optics and alignment mechanics are fixed onto the doorplate. We tested our set-up with the following objectives: Nikon 5X PLAN NA=0.15, Nikon 10x PLAN APO dry NA=0.45, Nikon 40X CFI PLAN APO dry NA=0.95 with a coverslip correction collar, Nikon 60X CFI PLAN APO dry NA=0.95 with a coverslip correction collar and Nikon 100x CFI PLAN Apo NCG immersion NA=1.4. Note that, as sketched, only one objective lens can be mounted in the SEM vacuum chamber at a time and objective exchange requires the SEM vacuum door to be opened. However, as we have recently shown, the function of a low-magnification objective lens may in experiments be performed with the SEM[27]. Note furthermore that in this setup the sample has to be mounted on a transparent support as is usually done in an inverted light microscope. Preferably, this cover glass has a conductive coating at the upper side to prevent charging artifacts under electron beam exposure. This can be done with a coating of Indium Tin Oxide (ITO)[10] or Diamond-Like Carbon (DLC) [14].

The system is designed in such a way that all components of the light microscope except the objective lens can be positioned outside the vacuum. In order to guide the light into and out of the vacuum chamber, an optical window is mounted in the door plate and a mirror guides the light from this window to the objective lens and vice versa. The mirror, a 45° elliptical mirror with aluminum coating, is mounted on a home-built vacuum compatible kinematic mirror mount. The window consists of a 10 mm thick optical flat (CVI Melles Griot, USA). All components inside the vacuum chamber, including objectives lenses, were subjected to cleaning procedures prior to use, to ensure that the platform is compatible with a vacuum base pressure of at least 10^{-6} mBar. The window has a clear diameter of 29 mm, which is sufficient for wide-field imaging with the objectives used in this research. Special attention might be needed when using a low magnification lens with a large exit pupil, as vignetting may occur when the clear opening of the window becomes too small to transmit the entire exit pupil.

For alignment, focusing, and sample translation several parts of the light microscope have to be movable. The required degrees of freedom have been indicated with arrows in

Figure 1. In Figure b and 2c we show the part of the platform that is placed inside the vacuum (i.e., the boxed area in Figure 1). The letters indicate parts that belong to the same component. We will discuss these components below. All mechanical components inside the SEM vacuum chamber have been selected for their vacuum-compatibility [28] and non-magnetic properties.

The light objective lens is mounted on a *z*-translation stage, which in turn is connected to a *xy*-translation stage. The *xy*-direction alignment of the lens is carried out by a motorized stage driven by two PI 310 NEXACT drives (Physik Instrumente, Germany) with a range of 1 mm. The minimal incremental motion of the NEXACT drives is in the picometer regime making it possible to perform very precise *x*-*y* alignment if needed.

The *z*-stage used for focusing the objective consists of a spring leaf guide translation stage. The stage is driven by an open loop PI 310 NEXACT drive that gives a translation range of 2 mm. For optical modes of operation whereby absolute movement is necessary, such as confocal microscopy, a vacuum-compatible closed-loop piezo pen (PI 841, Physik Instrumente, Germany) can be incorporated inside this mechanism with a close looped range of 15 μm.

Samples are mounted on a holder fork that is attached to a sample stage driven by two vacuum-compatible linear piezo-electric stepper motors (PI M662.4V, Physik Instrumente, Germany), with a open loop movement range of 18 mm. The sample stages are mounted on a sample pillar with which the sample plane can be rotated over a range of 20 mrad in both directions with respect to the focal plane of the objective. This ensures that the sample and focal plane can be aligned parallel to each other. As the sample can be translated independently of the electron and light optical systems, the entire sample can be inspected with both microscopes.

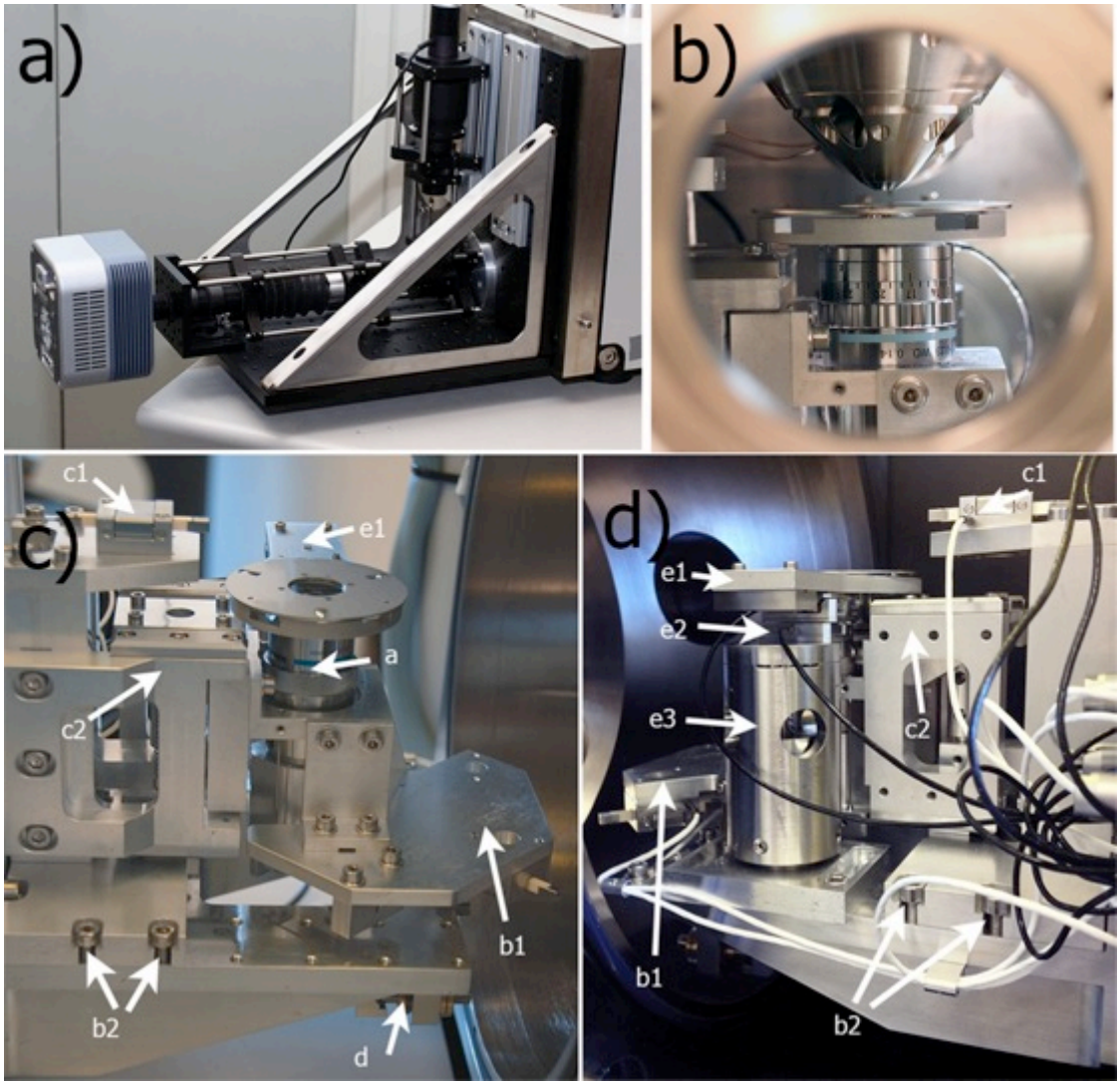

Figure 2: (a) Image of optical components mounted on the outside of the platform vacuum door. (b) View of the integrated microscope through a side-opening of the SEM. Below the sample is the light objective lens, above the sample the final electron lens. (c) and (d) Vacuum part of the platform. Arrows indicate individual parts where the lettering groups parts that belong to the same component according to the following scheme; a: Objective lens; b: Objective translation stage consisting of a (b1) motorized objective x/y-translation system, and (b2) a manual course x/y-translation fixing screws; c: Objective focusing stage consisting of a (c1) motor for driving the z-stage, and (c2) a leaf spring z-translation stage; d: 45°-Kinematic mirror for guiding the light to/from the objective lens; e: Sample stage consisting of (e1) sample holder fork onto which the sample is positioned (e2) x/y-translation stage, and (e3) a sample stage pillar for adjusting the tilt and yaw between the sample and objective lens.

Experimental performance of the integrated microscope

LM-SEM field-of-view alignment

The SEM has a field of view that ranges from approximately 100 nm to a few millimeters. In experiments, the SEM will be mainly used for high-magnification structural images within the light optical field of view. The center of this high-magnification SEM zoom can be selected throughout the optical field of view by application of a constant deflection voltage to the electron beam, but too large a deflection will introduce aberrations in the SEM image. For this reason, the axes of both microscopes need to be aligned to within 10 µm or lower.

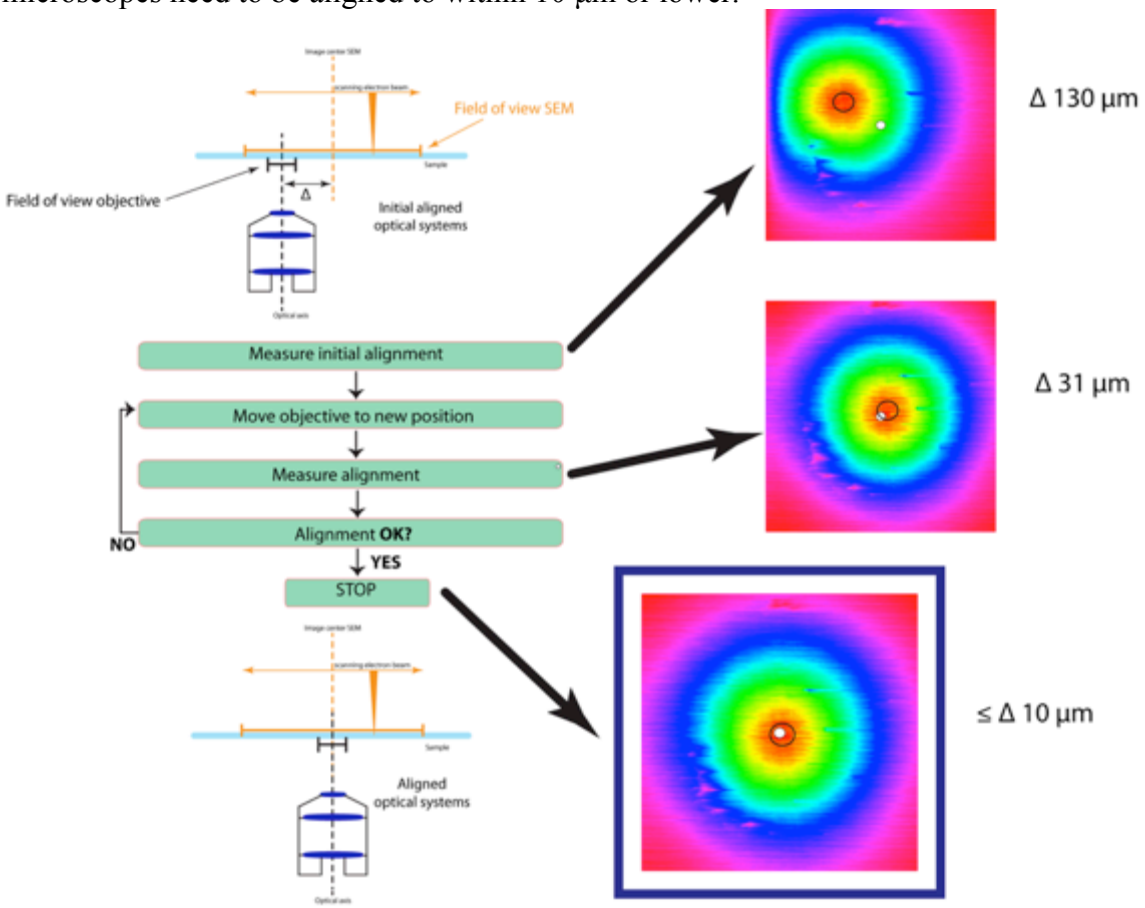

Figure 3: Illustration of the procedure to align the LM objective onto the center of the SEM field of view (FOV). The open circle indicates the center of mass of the cathodoluminescence profile, while the smaller white circle indicates the center of the SEM FOV. See text for description.

To perform this alignment, we exploit large field of view of the SEM. For the light microscope the field of view is generally smaller with the actual size depending on the magnification of the objective lens and on the tube lens configuration. We now map the collection efficiency of the light objective lens by scanning the electron beam over a field size larger than the optical field of view while detecting the cathodoluminescence generated in the substrate with the light microscope and using this signal to create a SEM image. Note that we here assume that the cathodoluminescence emission intensity is constant throughout the scan area, which is reasonable for a flat, homogeneous, transparent substrate. Thus, we effectively image the collection efficiency of the objective lens, which is rotationally symmetric around the axis (see Figure 3). From this intensity profile, we determine the position of the center of the optical field of view with respect to the SEM field of view by applying a pseudo-Gaussian fit. The objective lens is then translated towards the center of the SEM field of view until the desired alignment accuracy has been achieved. This iterative procedure is illustrated in Figure 3. Fine-adjustment of the alignment between a wide field light image and the electron image can be obtained by giving the electron beam deflectors an appropriate offset. In this way, we have recently obtained alignment accuracy in the order of 10 nm.

Electron microscopy and transmission light microscopy

We illustrate the use of the integrated microscope as a kind of further "zoom-in option" for light microscopy by combining the SEM with a simple white-light bright-field transmission setup. For the transmission microscopy, a non-collimated light source was integrated in the SEM chamber by incorporating a ring with white-light LED sources around the final SEM electron lens as schematically indicated in Figure 4. Further experimental details are given the Materials and Methods section.

A sample of cheek cells was stained with gold chloride to render contrast in both EM and LM. The gold chloride predominantly stains the chromosomes and other charged compartments in the cell [29], and thus in the LM gives visibility to the nucleus. Individual cells can be clearly identified in the transmission image in Figure 4, with the nuclei visible as black spots. Based on this image, a region can be selected for SEM inspection, as indicated by the red box in Figure 4. The SEM image shows the selected cells at high-magnification. The inner chromosome structure of the nuclei targeted by the gold chloride staining can be identified.

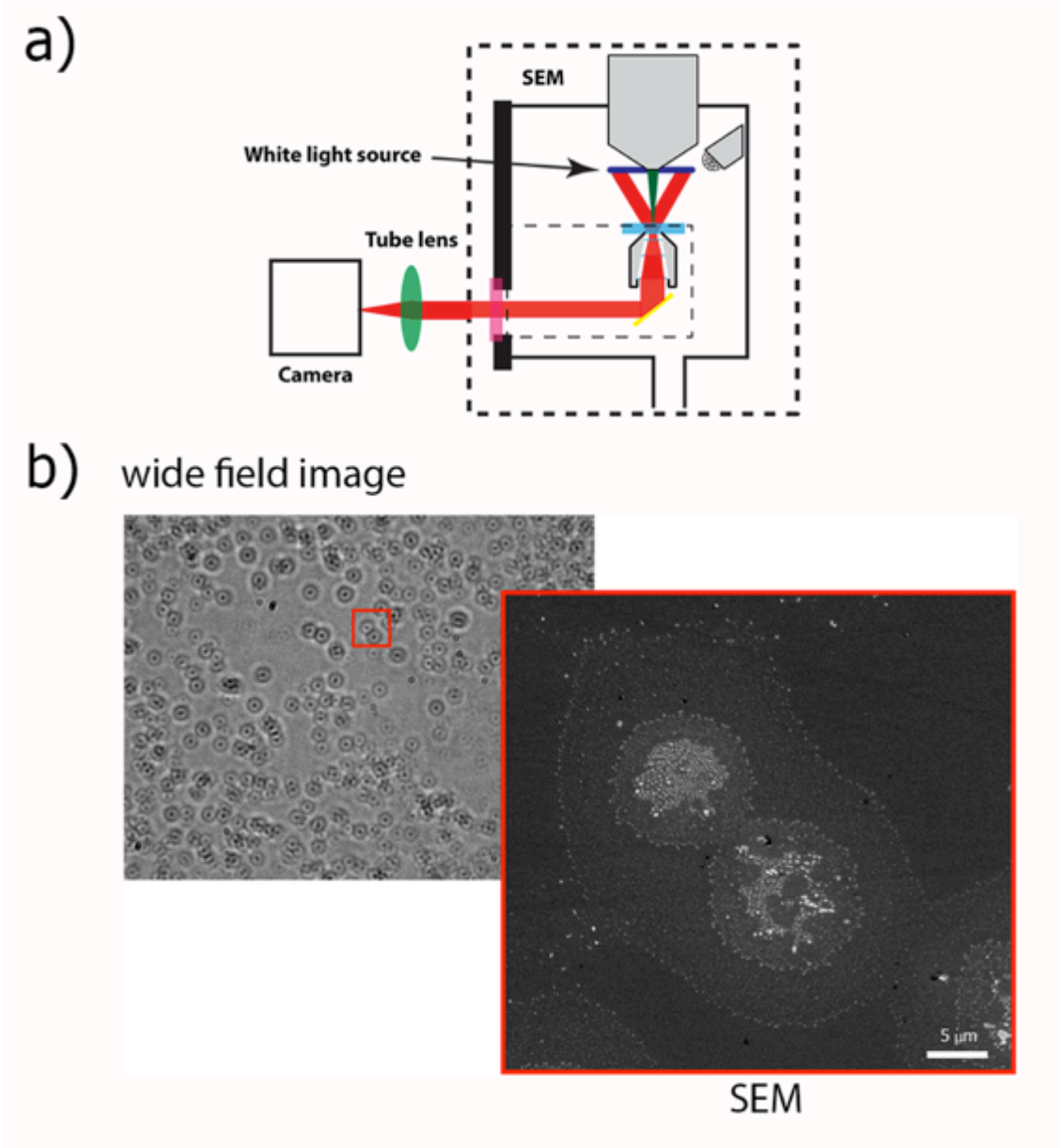

Figure 4: (a) The platform set up for white light transmission microscopy. (b) Wide field transmission image of cheek cells stained with HAuCl4. The SEM image shows a high resolution image of the region of interest marked with the red box in the wide field image.

Correlated electron microscopy and epi-fluorescence microscopy

For correlative SEM and fluorescence microscopy, the platform was set up as an epi-fluorescence microscope, according to the scheme depicted in Figure 5. For illumination a 470nm LED light source with collimator lens is used. Also shown in Figure 5 are example fluorescence and electron microscopy images of auto fluorescent pollen from

Chrysanthemum Indicum, taken with the 10x objective lens. No staining has been applied to this sample and the pollen was directly deposited on ITO-coated coverslips, dehydrated via degraded ethanol series and air-dried as in the example above. Upon comparison of FM and EM images, non-fluorescent debris can be identified in the SEM image, as indicated with the red arrow. In addition, pollen marked with yellow and red stars are (partly) obscured in FM and EM images respectively as they are positioned on top of other material resp. shadowed.

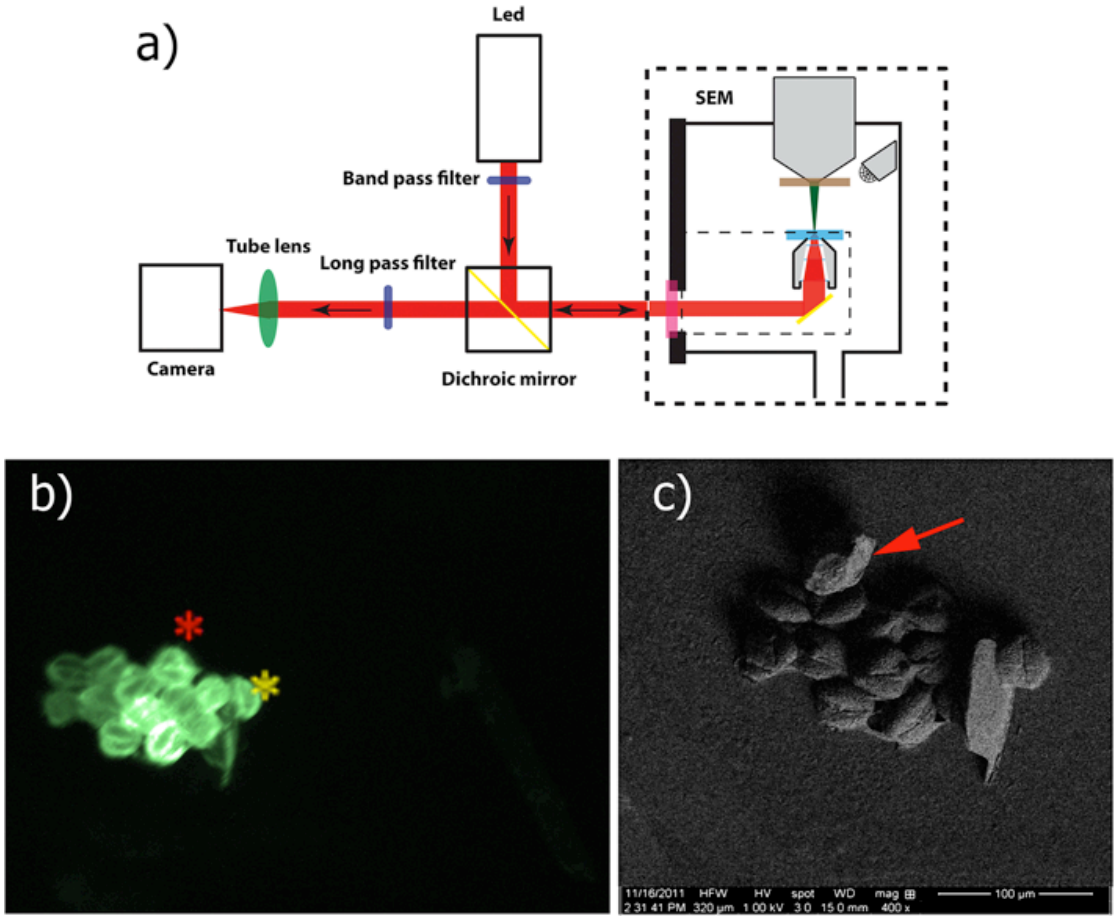

Figure 5: (a) Schematic illustration of the platform equipped with an epi-fluorescence microscope. (b) fluorescence image of pollen from the Chrysanthemum Indicum with (c) the SEM image from the corresponding area. The red arrow in the SEM image marks debris that is not autofluorescent. The red and yellow star mark pollen that are partly obscured in the SEM image.

To illustrate the resolution of the epi-fluorescence microscope we imaged two types of standard fluorescence microscopy samples with a 100 X NA=1.4 objective using vacuum compatible immersion oil.

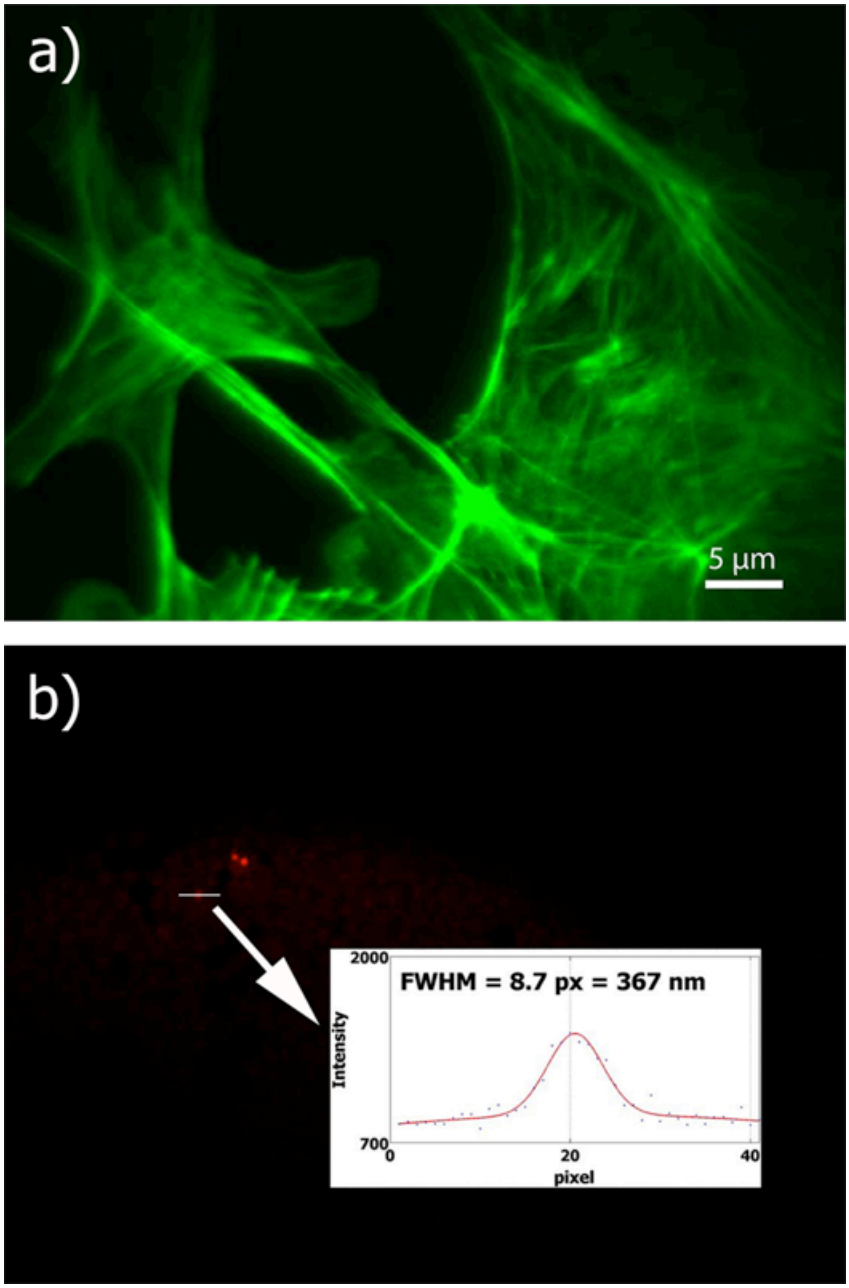

Figure 6. Illustration of performance of the epi-fluorescence microscope, (a) Image of a commercially available sample of BPAEC cells labeled for F-actin. (b) Image showing single 40nm fluorescent beads. The inset shows the intensity profile taken over the red line in the image.

Figure 6a shows an image of a standard commercially available fluorescence microscopy sample consisting of BPAEC cells, where F-actin is stained with Alexa488 phalloidin. As expected, the actin network is clearly resolved with our microscope. In Figure 6b we

show a measurement of 40 nm diameter fluorescence labeled polystyrene beads dried on a coverslip. The inset in Figure 6b shows the intensity profile taken along a line through the center of a particle as indicated in the image, showing a full width at half maximum of 376 nm.

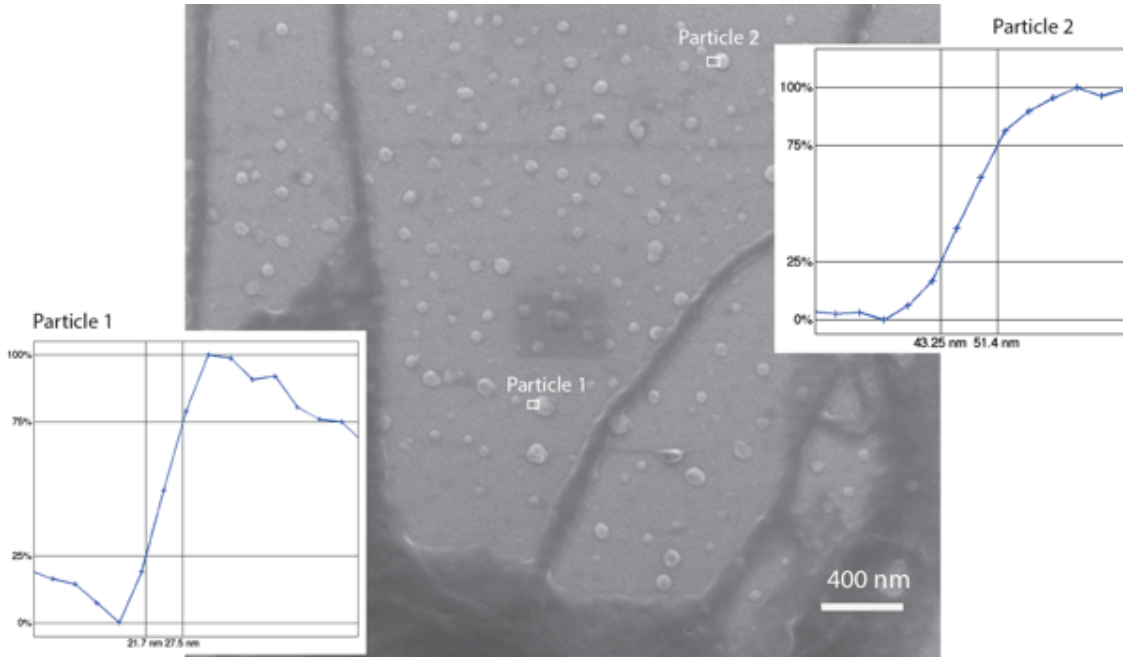

Figure 7: High resolution SEM image of cellular structure on an ITO coverslip, taken in SE mode (ETD detector). The two insets show intensity profiles for two selected grains on the ITO layer, with 25%-75% intensity edges indicated, corresponding to the FW50. The SEM is capable of resolving 6 nm structures as expected for this type of SEM at these experimental conditions.

Finally, we assess the resolution of the SEM, which we expect not to have suffered from the addition of the light microscope. Figure 7 shows a high-magnification zoom of the edge of a cellular sample on ITO where nanometer size features can be observed on the ITO substrate. The insets show the 25% to 75% intensities representing the FW50 size of the beam that indicate a resolution of the order of 6 nm at a working distance of 15 mm.

CLEM application and discussion

Finally, we want to illustrate the use of the integrated microscope with a basic CLEM example and discuss the further application of our instrument for biological CLEM. In

our example we use the fluorescence signal for identifying labeled cellular material and selecting regions of interest for subsequent EM inspection. Here, only fluorescence labeling has been applied, so the SEM serves to add sub-diffraction limited structural detail to the fluorescence image. Figure 8a-c shows results for colon adenocarcinoma cells labeled for actin with Alexa488-phalloidin. We note that for this cell type, the detailed actin network is not visible in wide-field fluorescence as it was for the cell type depicted in Figure 6a. In order to image the fine network of cell-cell connections, two neighboring cells were selected based on the FM image. Figure 8a shows the fluorescence image and overlay EM of a selected area. A higher-magnification SEM image zooming in on the area between the two cells is displayed in Figure 8b and 8c. This clearly highlights the details of the network of tentacles and small lamellae that connect the two cells. The typical width of individual tentacles in Figure 8 is 60 to 100nm and spacing are such that the detailed topography cannot be resolved in the fluorescence microscope.

A further step is to investigate the structural detail in the SEM images in relation to the expression of specific proteins visualized in the fluorescence microscope. We illustrate this with Figures 8d-f, displaying fluorescence and SEM images of the same cell type, but with a labeling for cortactin, a protein involved in the formation of filopodia and lammelipodia. The combination of these three images directly correlates the cortactin expression (Figure 8d) to the cellular topography visualized in secondary electron detection (Figure 8e) and the structural outline in backscatter electron mode (Figure 8f). Thus, it is immediately evident that the bright spot in the lower left corner in the fluorescence image corresponds to a slightly thicker part of the cell (Figure 8e).

To fully exploit the power of integrated CLEM, a combination with EM staining would be advantageous, especially for thin tissue sections. While heavy-metal stains may drastically quench fluorescence, dedicated probes and preparation protocols for CLEM that maintain molecular fluorescence in combination with EM staining, have recently been reported [15,30,31]. Immuno-fluorescence probes can be used for tissue navigation in combination with heavy-metal staining[6], and a protocol that after EM staining preserves sufficient signal from green fluorescent protein to perform optical super resolution has also been reported[14]. An attractive option for CLEM would also be the use of dual-contrast probes, such as fluorescent labeled nanoparticles or luminescent quantum dots [32].
The consequence of our choice to look at samples with the SEM from one side and with the light microscope from the other side is that it is well suited for the study of thin samples, but not for thicker samples. With secondary electron detection, the SEM can only image the surface and in backscatter imaging mode only the upper micrometer or so, while the light microscope has to look through the sample to see this slice. As indicated with the examples above, this is not an issue for the study of processes taking place in the thinner parts of cell, such as those related to cellular motility, and cell-cell signaling [27]. In addition, the thickness of many relevant specimens in bio-imaging, such as fixated cells and thin tissue sections, is readily covered by the focal range of high-NA objective

lenses. For thicker samples and samples with spatial variations in refractive index the fact that the light has to traverse the sample for correlation with SEM data, inevitably leads to optical aberrations. However, as there is flexibility in the optical path, the use of confocal microscopy, two-photon microscopy and aberration-correction by optical phase shaping can provide solutions for imaging thicker specimen.

In the present design, the sample cannot be tilted, while the original sample stage in the SEM does have this option. However, for high resolution fluorescence microscopy tilting is never possible and for CLEM, the sample is usually not tilted in the SEM either. Sample tilt could be a valuable addition in the combination with a dual-beam, i.e. electron and ion beam, system. In such a system, in-situ fluorescence monitoring could guide the precise removal of materials during ion milling [33].

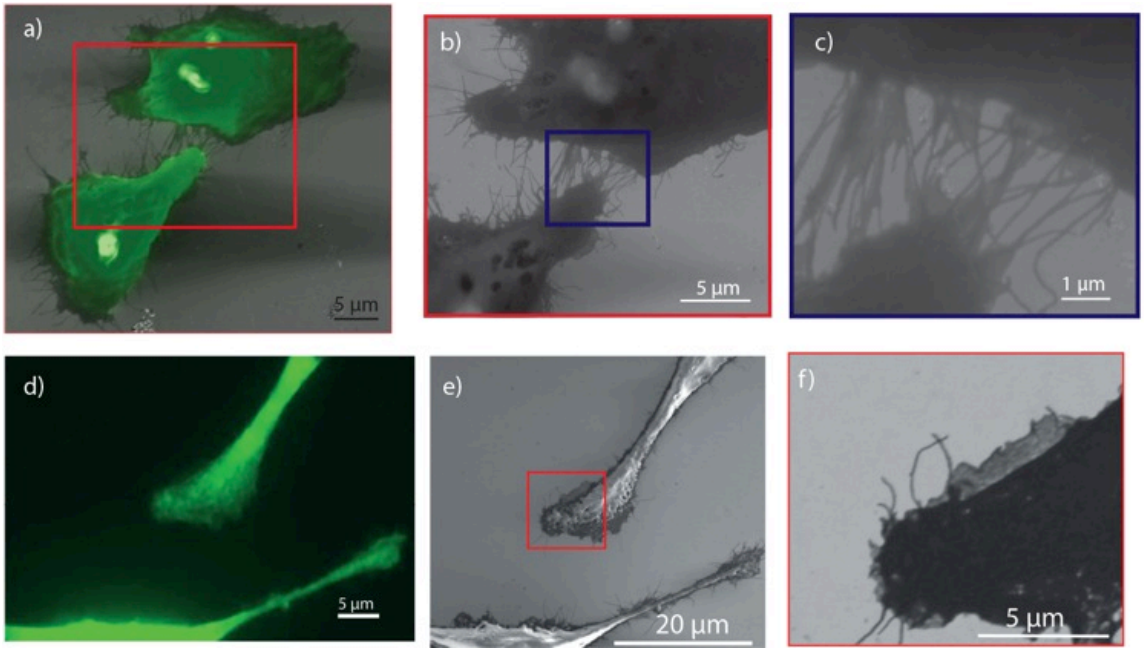

Figure 8: Correlative fluorescence and SEM images of colon adenocarcinoma cells immuno-labeled for actin with the fluorescence dye Alexa488. (a) Overlay image of fluorescence and SEM images of two nearby actin-labeled cells. (b) SEM image of the area marked with a red square in (a). (c) High-magnification SEM image of the sample showing the high resolution obtainable in the EM images. The "particles" in between the lamellae are structures in the ITO. (d) Fluorescence image of a cortactin-labeled adenocarcinoma cell. (e) Secondary electron image of the same region. (f) Back-scattered electron image of the boxed region in (e).

Samples have to be mounted on transparent substrates, just as in inverted microscopy, with preferably a transparent, conductive coating such as ITO. ITO-coated glass slides

have been shown to be compatible with cell culture for several cell types [10,34] and, in addition, the stronger scattering of electrons by the ITO as compared to the biological material offers a novel way for contrast generation in the SEM [10]. This is also evident from Figures 8 b, c, and f, where cellular features appear dark on a bright substrate background. Moreover, for correlative investigations and in techniques like array tomography [35], tissue sections that are usually prepared for inspection with TEM are now mounted on conductive transparent slides and inspected by SEM. In this way the sample can be transferred on the substrate from LM to SEM and the SEM allows for rapid inspection of a large array of sections. As noted by Micheva and Smith, the use of tissue sections offers the additional advantage that optical resolution in the axial direction is now determined by the thickness of the section and not anymore by the intrinsic poor axial resolution of the light microscope.

We have shown the integrated combination of EM with transmission light microscopy and wide field fluorescence microscopy. However, the integrated microscope can be equipped with a variety of light optical systems by (re)placing components on a breadboard attached to the SEM. This means that in principle any high-NA microscopy that is compatible with epi-illumination can be used, including super-resolution techniques such as STED, STORM, and PALM [36–38]. We anticipate that standard commercial optical illumination and detection modules that are mountable on the side-port of a regular inverted microscope can be mounted onto the integrated microscope, such as a confocal laser scanning module.

It is one of the main advantages of integrated microscopy that a sample can be inspected rapidly with both microscopes. In the presented system, high-NA fluorescence microscopy and SEM can in principle be performed simultaneously and this Simultaneous CLEM (SCLEM) [27] may drastically reduce CLEM inspection times and increase sample throughput. Aside from the fields of CLEM and bio-microscopy, the possibility to perform high-NA light microscopy in-situ in the SEM with the new platform may be useful in other areas of science. Correlative microscopy may find important applications in the chemical sciences in areas such as catalysis [39]. The high-NA objective lens provides a very efficient light collection system that may be beneficial for high-resolution cathodoluminescence investigations in materials sciences, nano-photonics [40], and plasmonics [41,42]. In addition, high-resolution light microscopy inspection of a sample during electron-beam irradiation may provide a unique, novel technique for studying electron-matter interactions and structural changes induced by electron exposure.

Conclusion

In conclusion, we have shown the integration of a high-NA light microscope in a standard scanning electron microscope without compromising on essential performance in either, as compared to stand-alone systems. The objective lens of the light microscope

can be pre-aligned to the center of the field of view of the SEM to within 10 μm by imaging its collection efficiency using cathodoluminescence generated in a transparent substrate. We have shown results for implementation with a white-light transmission microscope and with an epi-fluorescence microscope. In our opinion, this not only removes all issues related to sample transfer in the application of CLEM for finding regions of interest to image with electron microscopy, but also, perhaps more importantly, it extends the applications in which the information from high resolution fluorescence images is combined with the SEM-resolution structural information to draw conclusions on cellular functioning. In addition, this microscope may open novel possibilities for research in physics and chemistry that relies on highly efficient light detection and/or high-resolution light microscopy inside the SEM.

Acknowledgements
We would like to thank Daan van Oosten Slingeland, Martijn Haring, Frans Berwald, Jan de Loof, Ger Schotte, and Cor Barends for their assistance and discussions. The actin-labeled colon adenocarcinoma cells were kindly provided by Philip Voorneveld and James Hardwick (Leiden University Medical Center). A.P.J. Effting acknowledges support from a STW Valorization Grant.

References

[1] B.N.G. Giepmans, S.R. Adams, M.H. Ellisman, R.Y. Tsien, Science 312 (2006) 217.

[2] J. Orloff, ed., Handbook of Charged Particle Optics, 2nd Edition, Edited by J. Orloff, 2nd ed., CRC Press, 2009.

[3] R.E. Webster, M. Osborn, K. Weber, Exp. Cell Res. 117 (1978) 47.

[4] C.H. Wouters, J. Microsc. 147 (1987) 5.

[5] B.N.G. Giepmans, Histochem. Cell Biol. 130 (2008) 211.

[6] M.S. Lucas, M. Günthert, P. Gasser, F. Lucas, R. Wepf, Methods Cell Biol. 111 (2012) 325.

[7] J. Caplan, M. Niethammer, I.I. Taylor Russell M., K.J. Czymmek, R.M. Taylor, K.J. Czymmek, Curr. Opin. Struct. Biol. 21 (2011) 686.

[8] A. V. Agronskaia, J. a. Valentijn, L.F. van Driel, C.T.W.M. Schneijdenberg, B.M. Humbel, P.M.P. van B. en Henegouwen, A.J. Verkleij, A.J. Koster, H.C. Gerritsen, J. Struct. Biol. 164 (2008) 183.

[9] T. Kanemaru, K. Hirata, S.-I. Takasu, S.-I. Isobe, K. Mizuki, S. Mataka, K.-I. Nakamura, Ultramicroscopy 109 (2009) 344.

[10] H. Pluk, D.J. Stokes, B. Lich, B. Wieringa, J. Fransen, J. Microsc. 233 (2009) 353.

[11] C. Spiegelhalter, V. Tosch, D. Hentsch, M. Koch, P. Kessler, Y. Schwab, J. Laporte, PLoS One 5 (2010).

[12] Y. Maruyama, T. Ebihara, H. Nishiyama, M. Suga, C. Sato, J. Struct. Biol. 180 (2012) 259.

[13] G.E. Murphy, K. Narayan, B.C. Lowekamp, L.M. Hartnell, J.A.W. Heymann, J. Fu, S. Subramaniam, J. Struct. Biol. 176 (2011) 268.

[14] S. Watanabe, A. Punge, G. Hollopeter, K.I. Willig, R.J. Hobson, M.W. Davis, S.W. Hell, E.M. Jorgensen, Nat. Methods 8 (2011) 80.

[15] W. Kukulski, M. Schorb, S. Welsch, A. Picco, M. Kaksonen, J.A.G. Briggs, J. Cell Biol. 192 (2011) 111.

[16] B.G. Kopek, G. Shtengel, C.S. Xu, D.A. Clayton, H.F. Hess, Proc. Natl. Acad. Sci. 109 (2012) 6136.

[17] K.A. Jahn, D.A. Barton, K. Kobayashi, K.R. Ratinac, R.L. Overall, F. Braet, Micron 43 (2012) 565.

[18] A. Sartori, R. Gatz, F. Beck, A. Rigort, W. Baumeister, J.M. Plitzko, J. Struct. Biol. 160 (2007) 135.

[19] C.. Wouters, H.K. Koerten, Cell Biol. Int. Rep. 6 (1982) 955.

[20] C.H. Wouters, H.K. Koerten, J. Bonnet, W.T. Daems, J.S. Ploem, J. Microsc. 141 (1986) 41.

[21] H. Pluk, D.J. Stokes, B. Lich, B. Wieringa, J. Fransen, J. Microsc. 233 (2009) 353.

[22] K. Ohta, S. Sadayama, A. Togo, R. Higashi, R. Tanoue, K. ichiro Nakamura, Micron 43 (2012) 612.

[23] H. Nishiyama, M. Suga, T. Ogura, Y. Maruyama, M. Koizumi, K. Mio, S. Kitamura, C. Sato, J. Struct. Biol. 169 (2010) 438.
[24] I.E.G. Morrison, C.L. Dennison, H. Nishiyama, M. Suga, C. Sato, A. Yarwood, P.J. O'Toole, Methods Cell Biol. 111 (2012) 307.
[25] S. Jones, S.K. Chapman, P.R. Crocker, G. Carson, D. a Levison, J. Clin. Pathol. 35 (1982) 425.
[26] L. Reimer, Meas. Sci. Technol. 11 (2000) 1826.
[27] N. Liv, A.C. Zonnevylle, A.C. Narvaez, A.P.J. Effting, P.W. Voorneveld, M.S. Lucas, J.C. Hardwick, R.A. Wepf, P. Kruit, J.P. Hoogenboom, PLoS One 8 (2013).
[28] W.C. Bigelow, ed., Vacuum Methods in Electron Microscopy, Portland Press, 1994.
[29] L. Kass, Stain Technol. 54 (1979) 17.
[30] M.A. Karreman, A. V. Agronskaia, E.G. van Donselaar, K. Vocking, F. Fereidouni, B.M. Humbel, C.T. Verrips, A.J. Verkleij, H.C. Gerritsen, J. Struct. Biol. 180 (2012) 382.
[31] M. a Karreman, E.G. Van Donselaar, A. V Agronskaia, C.T. Verrips, H.C. Gerritsen, J. Histochem. Cytochem. 61 (2013) 236.
[32] B.N.G. Giepmans, T.J. Deerinck, B.L. Smarr, Y.Z. Jones, M.H. Ellisman, Nat. Methods 2 (2005) 743.
[33] A. Rigort, F.J.B. Baeuerlein, E. Villa, M. Eibauer, T. Laugks, W. Baumeister, J.M. Plitzko, Proc. Natl. Acad. Sci. U. S. A. 109 (2012) 4449.
[34] N. Rushe, M. Ball, W.M. Carroll, S. Healy, J. Mcmanus, D. Cunningham, J. Mater. Sci. Mater. Med. 16 (2005) 247.
[35] K.D. Micheva, S.J. Smith, Neuron 55 (2007) 25.
[36] S.W. Hell, Science 316 (2007) 1153.
[37] M. Bates, B. Huang, G.T. Dempsey, X. Zhuang, Science 317 (2007) 1749.
[38] E. Betzig, G.H. Patterson, R. Sougrat, O.W. Lindwasser, S. Olenych, J.S. Bonifacino, M.W. Davidson, J. Lippincott-Schwartz, H.F. Hess, Science 313 (2006) 1642.
[39] M.A. Karreman, I.L.C. Buurmans, J.W. Geus, A. V. Agronskaia, J. Ruiz-Martínez, H.C. Gerritsen, B.M. Weckhuysen, Angew. Chemie - Int. Ed. 51 (2012) 1428.
[40] L.F. Zagonel, L. Rigutti, M. Tchernycheva, G. Jacopin, R. Songmuang, M. Kociak, Nanotechnology 23 (2012) 455205.
[41] T. Coenen, E.J.R. Vesseur, A. Polman, Appl. Phys. Lett. 99 (2011).
[42] T. Coenen, E.J.R. Vesseur, A. Polman, A.F. Koenderink, Nano Lett. 11 (2011) 3779.

Ch. 7 Conclusive summary and outlook

The goal of this PhD research was to develop new beam position correction methods for multi electron beam systems. What is the first step in the general improvement scheme for scanning electron beam systems, that is also applicable for most multi electron beam systems.

For this we studied two beam alignment concepts:

A] 'One knob' alignment, to correct rotation misalignment between array blocks placed at different positions along the beam path

B] Individual beam control, to control each beamlet independently

The second goal of this PhD research was to develop tooling for fabrication, inspection and testing of MEMS multi beam optical elements. For the purpose of building MEMS electron optical devices an alignment tool has been developed for aligning, stacking and bonding multi beam components. For inspection and testing a versatile platform that can be incorporated in a standard SEM has been developed, whereby the SEM can function both as imaging tool and electron illumination system for multi beam elements. Incorporating a high NA inspection microscope for imaging the position and shape of the multiple electron beams on a fluorescent screen has proved to be a very useful inspection tool. When the fluorescent screen is replaced by a sample, this microscope can be used as an imaging tool for correlative microscopy (light microscopy combined with scanning electron microscopy on the same sample) for life sciences. Short summaries of each chapter are highlighted below.

Chapter 2: Electrostatic rotator for alignment purposes in multi electron beam systems

This chapter has been published in: A.C. Zonnevylle et al., *Microelectronic Engineering 87 (2010) 1095–1099*

In single charged particle beam column the alignment is obtained either by mechanical shift of the lenses or by XY alignment deflectors. The problem in multi beam array systems is that it is only possible to deflect the array of beams in the XY direction and not able to correct for a possible rotation errors between arrays blocks. In chapter 2, we have shown a conceptual method that proofs rotation misalignments can be solved with a special five-electrode array (multi beam) electrostatic lens. We have shown the working of the concept by discussing a single beam lens and lens array version. In the five electrode electrostatic lens we have shown that XY beam shifts can be induced without changing the focal distance. The fabrication method of such a device has been described.

Chapter 3: Deflection properties of an electrostatic electron lens with a shifted electrode

This chapter has been the basis for the publication: A.C. Zonnevylle et al. J. Vac. Sci. Technol. B 31(6), Nov/Dec 2013

In chapter 3, we have proposed a new electron optical component: an electrostatic lens in which one electrode is intentionally shifted laterally, breaking the rotational symmetry. This lens is called a 'shift lens'. Usually, a shifted electrode is undesired and the resulting aberrations are calculated only for the purpose of setting manufacturing requirements. However, the shift lens can be applied as a deflector. Thus, in multi beam systems with an individual microlens for each beam, all beams can be deflected with a single voltage. By giving a different shift to each lens, the deflection can be different for each beam. This allows the creation of a multi beam rotation error corrector, as discussed in chapter 2. The optical properties of an electrostatic 5-electrode lens with a shifted central electrode are analyzed. For describing the optical properties of the shift lens, a simple mirror symmetric model in combination with Taylor polynomials is used. The validation has been done with a newly developed simulation package based on the boundary element method run on a General-Purpose Graphics Processing Unit (GPGPU), so called standard graphic PC card, to dramatically speed up the calculation processing. The central electrode is shifted over a range of 1% up to 20% of the diameter of the lens. We find the dependences of deflection, defocus, astigmatism, second order and third order aberrations on shift distance and excitation. We expect the shift lens to be a useful new optical component, especially in multi beam systems.

Chapter 4: Multi-Electron-Beam Deflector Array

This chapter has been published: A.C. Zonnevylle et al., Microelectronic Engineering 123 (2014) 140–148

In chapter 4, we have designed and manufactured a 25-beam electrostatic *x-y* deflector array, which gives individual control over each beamlet in a multi-beam system. The deflector plates and ground plane were prepared from deposited molybdenum and the micro-fabrication process is compatible with a bipolar- and CMOS integrated circuit process line. This compatibility makes it possible in the future to integrate control electronics on the substrate allowing for individual control of the beamlets in massively parallel electron beam systems. The fabricated deflector is of the in-plane type. We have shown that it cannot be described using the same equations as for the long plate type deflectors. In-plane deflectors generally exhibit weaker deflection than equipotential long plate deflectors, however they exhibit reduced higher order

multipole effects. The deflector has been tested in a testing platform inside a SEM and simulation and experimental results are in agreement.

Chapter 5: A versatile tool for sub-micron alignment, stacking and adhesive bonding of electron optical MEMS components

In chapter 5, we describe the design, building and testing of an alignment tool that is suited for multi electron beam MEMS component stacking and bonding. The tool is able to do sub micron alignment stacking with adhesive bonding after polymerization. The tool can be used for a wider variety of MEMS elements stacking and bonding and can easily be adapted due to its modular design. To make it suitable for university research, many different sizes and shapes of such multi beam components can be stacked. We were able to align and fixate elements better then 500nm.

Chapter 6: Integration of a high-NA light microscope in a Scanning Electron Microscope

This chapter has been published in: Zonnevylle et al., *Journal of Microscopy, Vol. 252, Issue 1 2013, pp. 58–70*

In chapter, 6 we have shown the integration of a high-NA light microscope in a standard scanning electron microscope without compromising on essential performance in either, as compared to stand-alone systems. The objective lens of the light microscope can be pre-aligned to the center of the field of view of the SEM to within 10 μm by imaging its collection efficiency using cathodoluminescence generated in a transparent substrate. We have shown results for implementation with a white-light transmission microscope and with an epi-fluorescence microscope. In our opinion, this not only removes all issues related to sample transfer in the application of CLEM for finding regions of interest to image with electron microscopy, but also, perhaps more importantly, it extends the applications in which the information from high resolution fluorescence images is combined with the SEM-resolution structural information to draw conclusions on cellular functioning.

General conclusion, discussion and outlook

Two methods for individual beam position correction methods for multi beam systems, a versatile alignment tool for stacking multi electron beam MEMS parts and integrated high NA microscope in a SEM have been presented and discussed in this thesis.

'One knob' correction

The rotation corrector for rotation errors between multi beam array blocks has been simulated and mathematically described. It is discussed in chapter 2 and 3. We would like to note that a first experimental test with the corrector, built with the alignment setup as described in chapter 5, has been conducted and looks promising. These results have not yet been reported in this thesis. Experimental data are too preliminary for publication and some experimental issues still need to be addressed. It would have been interesting to see if this multi beam rotation corrector would work as modeled, because it would also have given us an insight into the accuracy of the alignment tool in building high multi beam electron stacks.

Individual beam control

The possibility of individual beamlet control in a multi beam component with MEMS fabricated components has been described, simulated, fabricated and proven to work by experimental testing. It is described in chapter 4. We would like to mention that MAPPER Lithography, a company developing multi beam electron lithography systems, has started to incorporate an individual beam deflection control in their design, based on the work of this PhD project. An interesting next step would be to see if it would also be possible to build a device that can be used for the next two improvement steps (individual focus and stigmation control) with this technology, as discussed in chapter 4.

In general we can conclude that both described alignment concepts work in theory and simulation and that the individual beam control has been tested experimentally. We can therefore conclude that both concepts are applicable methods in multi electron beam systems.

Alignment tool

The versatile alignment tool for alignment, stacking and bonding for multi electron beam MEMS components has been built and tested, as described in chapter 5. We have shown that sub micron alignment of two components is possible with the use of special adhesive. Whether the tool is actually suited to make 'perfect' five-component array stacks as described in chapters 2 and 3 has not been proven yet. The data from the experimentally tested build stacks are too preliminary to come to a conclusion. It is worthwhile to mention that in 2016 the tool still functions for general purposes in the general research topics in the Charged Particle Optics group. Several PhD/Msc/Bsc

candidates are using the tool (sometimes with some small modifications) for the fabrication of multi electron beam systems and related devices. The chapter in which the author describes the tool dates from 2013.

Integration of high NA microscope in a SEM

The designed and build versatile inspection platform works and can be used in various experiments whereby a high NA microscope is needed in the SEM positioned under the final lens. Currently several PhD/Msc/Bsc candidates are using and further developing the systems for their research on combined light/electron imaging, testing and fabrication of multi electron beam systems and related devices. Some examples of use are: multi electron beam transmission detection in the Charged Particle Optics group multi beam SEM (see patent list), fluorescence imaging combined with SEM imaging (see publication list) and cathodoluminescence experiment (see publication list and patent list)

The development of the versatile inspection platform has led to a Spin Off company called DELMIC BV that has further developed, in collaboration with the TU Delft and other academia partners, the SECOM platform into a commercially saleable product. The SECOM platform is now actively sold by DELMIC and has sparked a worldwide scientific interest and research in various applications.

Ch. 7 Concluderende samenvatting en vooruitzicht

Het eerste doel van dit promotieonderzoek was om nieuwe bundel correctie positie methoden voor multi-elektronenbundel systemen te ontwikkelen. Hiervoor bestudeerden wij twee concepten:

> ***A] 'Één knop' uitlijning, om rotatie fouten tussen verschillende lens matrix blokken te corrigeren geplaatst op verschillende posities in het bundel pad.***
> ***B]Individuele bundel controle, voor individuele controle van iedere straal.***

Het tweede doel van dit promotieonderzoek was om tooling voor de productie, inspectie en testen van MEMS multi-beam optische elementen te ontwikkelen.
Ten behoeve van de bouw MEMS elektron-optische componenten een uitlijning instrument is ontwikkeld voor het uitlijnen, stapelen en fixeren van multi-beam componenten. Voor inspectie en het testen een multi zijdig platform is ontwikkeld dat in een standaard SEM geplaats kan worden, waarbij de SEM kan functioneren zowel als imaging tool en elektronen bundel voor multi-beam elementen. Een hoge NA inspectie microscoop voor beeldvorming van de positie en de vorm van de meerdere elektronenbundels op een fluorescerend scherm heeft bewezen een zeer nuttig inspectie apparaat te zijn. Wanneer het fluorescerend scherm wordt vervangen door een sample kan deze microscoop worden gebruikt als een imaging tool voor correlatieve microscopie (lichtmicroscopie gecombineerd met scanning elektronenmicroscopie op hetzelfde monster) voor de biowetenschappen.
Korte samenvattingen van elk hoofdstuk worden hieronder aangegeven.

Hoofdstuk 2: Elektrostatisch rotator voor uitlijning van multi elektronen bundel systemen

Dit hoofdstuk is gepubliceerd in: A.C. Zonnevylle et al., *Microelectronic Engineering 87 (2010) 1095–1099*

In enkele bundel kolom van geladen deeltjes wordt de uitlijning verkregen door een mechanische verschuiving van de lenzen of door XY uitlijning doormiddel van deflectoren. Het probleem bij multi-beam systemen is dat het alleen mogelijk de matrix van de alle bundels in de XY richting af te buigen en is niet in staat om de eventuele rotatie fouten te corrigeren tussen de matrix blokken. In hoofdstuk 2 hebben we een conceptuele methode laten zien die rotatie afwijkingen kan corrigeren met een speciale vijf-elektrode-matrix (multi-beam) elektrostatische lens. We hebben de werking van het concept aan getoond door het bespreken van een enkele straal lens en de lens matrix-versie. In de vijf elektrode elektrostatische lens hebben we aangetoond dat XY bundel

verschuivingen worden verkregen zonder de brandpuntsafstand verandering. De vervaardigingsmethode van een dergelijke ontwerp is verder beschreven.

Hoofdstuk 3: Afbuiging eigenschappen van een elektrostatische elektronenlens met een verschoven electrode

Dit hoofdstuk is de basis voor de publicatie: A.C. Zonnevylle et al. J. Vac. Sci. Technol. B 31(6), Nov/Dec 2013

In hoofdstuk 3, hebben wij een nieuw elektron optische component voorgesteld: een elektrostatische lens waarin één elektrode opzettelijk is verschoven, waarbij de rotatiesymmetrie is gebroken Deze lens is een 'shift lens' genoemd. Meestal is een verschoven elektrode ongewenst en resulterende afwijkingen worden alleen bepaald voor het zetten van de fabricatie eisen. Echter, de shift lens worden gebruikt als een deflector. In multibeam systemen met een individuele microlens voor iedere bundel, kunnen alle bundels worden afgebogen met een enkele spanning. Door een andere verschuiving voor elke micro lens, kan de afbuiging verschillend zijn voor iedere bundel. Dit geeft de mogelijkheid voor het creëren van een multi beam rotatie fout corrector, zoals besproken in hoofdstuk 2. De optische eigenschappen van een elektrostatische 5-elektrode lens met een verschoven midden elektrode zijn geanalyseerd. Voor het beschrijven van de optische eigenschappen van de shift lens, wordt een eenvoudige spiegel symmetrisch model in combinatie met Taylorpolynomen gebruikt. De validatie is gedaan met een nieuw ontwikkelde simulatie-pakket op basis van de boundary element methode gedraaid op een General-Purpose Graphics Processing Unit (GPGPU), de zogenaamde standaard grafische PC card, om de berekenings tijd dramatisch te versnellen. De midden elektrode is verschoven over een bereik van 1% tot 20% van de diameter van de lens. Wij vinden de afhankelijkheid van de afbuiging, defocus, astigmatisme, tweede orde en derde orde aberraties als functie van de verschuiving en excitatie. We verwachten dat de shift lens een nuttige nieuwe optische component is, vooral in multibeam systemen.

Hoofdstuk 4: Multi-elektron bundel deflector matrix

Dit hoofdstuk is gepubliceerd in: A.C. Zonnevylle et al., Microelectronic Engineering 123 (2014) 140–148

In hoofdstuk 4 hebben wij een 25-beam elektrostatische x-y deflector matrix ontworpen en vervaardigd, wat individuele controle over iedere bundel geeft in een

multi-beam systeem. De afbuigplaten en massaplaat zijn gemaakt uit molybdeen en het micro-fabricage proces is compatibel met een bipolar- en CMOS process lijn. Deze compatibiliteit maakt het mogelijk in de toekomst de stuur elektronica geïntegreerd op de drager te fabriceren waardoor individuele besturing van de bundels in massive parallel elektronenbundel system mogelijk wordt. De gefabriceerde deflector is van het in-plane type. We hebben aangetoond dat deze niet kan worden beschreven met behulp van dezelfde vergelijkingen als op lange plaat deflector. In-plane deflectoren vertonen in het algemeen zwakkere afbuiging dan de lange plaat deflectoren, maar ze vertonen een lagere hogere orde multipool effecten.
De deflector is getest in een testplatform in een SEM en de simulatie en experimentele resultaten zijn in overeenstemming.

Hoofdstuk 5: Een veelzijdige tool voor sub-micron uitlijning, stapelen en lijmen van elektronen optisch MEMS componenten

In hoofdstuk 5 beschrijven we het ontwerp, bouw en het testen van een alignement instrument dat geschikt is voor het stapelen en lijmen van multi-elektronenbundel MEMS component. De tool is in staat om met sub-micron te aligneren, te stapelen en te lijmen. Het apparaat kan worden gebruikt voor het stapelen en fixeren van een breed scala van MEMS elementen stapelen en kan gemakkelijk worden aangepast door zijn modulaire opbouw. Om het geschikt te maken voor universitair onderzoek, kunnen veel verschillende maten en vormen van dergelijke multi-beam componenten worden gebruikt. We waren in staat elementen beter dan 500nm te aligneren en te fixeren.

Hoofdstuk 6: Integratie van een hoge-NA lichtmicroscoop in een raster elektronen microscoop

Dit hoofdstuk is gepubliceerd in: Zonnevylle et al., *Journal of Microscopy, Vol. 252, Issue 1 2013, pp. 58–70*

In hoofdstuk 6 hebben we de integratie van een hoge-NA lichtmicroscoop in een standaard raster elektronen microscoop zonder concessies te doen aan de prestaties van beide, ten opzichte van stand-alone systemen. De objectieflens van de lichtmicroscoop kan vooraf worden afgestemd op het centrum van het gezichtsveld van de SEM binnen 10 μm door het afbeelden van het collectie rendement met behulp van kathodoluminescentie opgewekt in een transparant substraat. We hebben resultaten getoond met een wit-lichttransmissie microscoop en met een epi-fluorescentie microscoop. Naar onze mening, verwijdert dit niet alleen alle kwesties in verband met de overdracht bij CLEM experimenten voor het vinden van de regio's die van belang zijn voor de afbeelding met elektronenmicroscopie, maar ook, misschien nog belangrijker, het breidt de toepassingen waarin de informatie van hoge resolutie fluorescentie-beelden

wordt gecombineerd met de SEM-resolutie structurele informatie om conclusies te trekken over de cellulaire functioneren.

Generieke conclusie, discussie en voortuitzicht

Er zijn twee methoden voor individuele beam positie correctie in multi beam systemen, een veelzijdig tool voor het stapelen en uitlijnen van multi-elektronen bundel MEMS onderdelen en geïntegreerde high NA microscoop in een SEM gepresenteerd en besproken in dit proefschrift.

‘ één knop correctie’

De rotatie corrector voor rotatie fouten tussen de multi beam blokken is gesimuleerd en wiskundig beschreven. Besproken in hoofdstuk 2 en 3. We willen graag meegeven dat de eerste experimentele test met de corrector, gebouwd met de uitlijning setup zoals beschreven in hoofdstuk 5, zijn uitgevoerd en zien er veelbelovend uit. Deze resultaten zijn niet gemeld in dit proefschrift. Experimentele gegevens zijn nog te voorlopig voor publicatie en een aantal experimentele kwesties moeten nog worden opgelost. Het zou interessant zijn om te zien of deze multi beam rotatie corrector zou werken zoals gemodelleerd, omdat het ons ook een inzicht in de nauwkeurigheid van de uitlijning tool in de bouw van hoge multi-beam elektron stacks kan gegeven.

Individuele bundel aansturing

De mogelijkheid om individuele bundels te controlen in een multi-beam component met MEMS gefabriceerde onderdelen is beschreven, gesimuleerd, gefabriceerd en bewezen te werken door middel van experimenten. Beschreven in hoofdstuk 4. We zouden graag vermelden dat MAPPER Lithography, een bedrijf dat multi-beam electron lithografie-systemen ontwikkeld, is begonnen met een individuele beam aansturing op te nemen in hun ontwerp, gebaseerd op het werk van dit promotieonderzoek. Een interessante volgende stap zou zijn om te zien of het ook mogelijk is om deze technologie ook kan worden gebruikt voor de volgende twee stappen van verbetering (individuele focus en stigmation controle), zoals besproken in de discussie van hoofdstuk 4.

In het algemeen kunnen we concluderen dat beide beschreven correctie concepten werken in theorie en simulatie en dat de individuele bundel controle experimenteel is aangetoond. We kunnen dus concluderen dat beide concepten bruikbare methoden zijn in multi elektronenbundel systemen.

Uitlijn tool

De multi inzetbare uitlijn tool voor stapelen en lijmen voor multi elektronen bundel MEMS componenten is gebouwd en getest, zoals beschreven in hoofdstuk 5. We hebben

aangetoond dat sub-micron uitlijning van twee componenten mogelijk is met het gebruik van speciale lijm. Of het gereedschap daadwerkelijk geschikt is voor het maken van 'perfecte' vijf-component stacks arrays, zoals beschreven in hoofdstuk 2 en 3 is nog niet bewezen. De gegevens van de experimenteel geteste gebouwde stacks is nog te voorlopig om tot een conclusie te komen. Het is de moeite waard om nog te vermelden dat in 2016 de tool nog steeds wordt gebruik in de algemene onderzoeksthema's van de Deeltjesoptica groep. Verscheidene PhD / Msc / Bsc kandidaten (soms met enkele kleine modificaties) vervaardigen hun multi elektronenbundel en aanverwante apparaten met de tool. Het hoofdstuk waarin de auteur de tool bespreekt komt uit 2013.

Integratie van hoge NA microscoop in een SEM

Het ontworpen en gebouwde inspectieplatform werkt en kan worden gebruikt voor diverse experimenten waarbij een hoge NA microscoop nodig is in een SEM gepositioneerd onder de laatste lens van de SEM. Momenteel gebruiken verschillende PhD / MSc / Bsc kandidaten deze tool in hun onderzoek en wordt deze verder gebruikt in hun onderzoek op gecombineerde lichte / elektron beeldvorming, testen en fabricage van multi elektronenbundel systemen en aanverwante apparaten. Enkele voorbeelden van het gebruik zijn: multi-elektronenbundel transmissie detectie in de multi beam SEM van de Deeltjesoptica groep (zie patent lijst), fluorescentie beeldvorming in combinatie met SEM beeldvorming (zie publicatielijst) en cathodoluminescentie experiment (zie publicatielijst en patent lijst)

De ontwikkeling van dit veelzijdige inspectie platform heeft geleid tot een spin-off bedrijf genaamd DELMIC BV dat de technologie verder heeft ontwikkeld, in samenwerking met de TU Delft en andere academische partners. Het SECOM platform wordt actief verkocht door DELMIC en heeft een wereldwijde wetenschappelijke interesse en onderzoek in diverse toepassingen aangewakkerd.

Acknowledgements

A great deal of people have contributed to this PhD project. First of all I would like to thank Pieter Kruit, my promotor, mentor and scientific advisor over the years. I would like to express additional gratitude for helping me to write this thesis. I know it was sometimes difficult and frustrating for you to correct my strange sentences over and over again.
Thank you for having me in your group from my Bsc up to my PhD and helping me to become a scientist and engineer over the years.

Kees Hagen who has been a great listener, helper and a critical co-author who kept everybody sharp. I enjoyed being involved in your course Technology Management for two years.

Jacob Hoogenboom it was great fun driving with you everyday from Utrecht to Delft. I still miss the conversations we had in the car (except the times you were exhausted when your youngest daughter was born, being a parent myself I fully understand now). I know for sure that our best ideas and inventions were sparked during these conversations which has led partially to the founding and success of DELMIC.

MAPPER BV, for sponsoring the first year of this PhD project. Old MAPPER colleagues Marco, Ferry and Stijn for their input and support in the first year of my PhD research.

Fellow CPO group members, Martijn, Leon, Guido, Merijntje, Ben, Vincenzo, Anand, Willem, Anda, Yanxia, David, Angela, Nanlan, Robert, Sangeeta, Marijke , Gerwald, Marco, Marco V, Takashi, Martin, Maykel, Neda, Diederick, ChrisP and Yan Ren. It was a great experience to work with you for several years. It would like to express a little more gratitude to following former colleagues: Ali who was a great colleague to discuss multi beam electron optics. Ivan for your great help with chapter number 3. Thomas for his invaluable contribution of developing the new charged particle simulator, I was happy for you that you could also use it for your Msc thesis in Utrecht as well.

The support staff of CPO and DEMO that were of a great help to get things really happen. Anjella, and Margaret thank you for helping me with all kind of paper work and travel stuff. Carel, Vladimir, Frans, Jacques, Jan and Han, I learnt a lot of technical skills from all of you that I am still using on a daily basis. Ruud, Alix, Ger and late Cor Barends for designing, drawing and making all my needed tools and devices.

The Dimes and Kavli Nano lab staff for the facilities and technical advise to make all my MEMS devices.

Andries, Sander and Eric it was great experience sharing an office with you in the first year of DELMIC.

My family: Willemijn my wife, my children Olivier, Josephine and Julius, my parents and parents-in-law and the rest of my family for their never-ending support while finishing this thesis.

About the Author

Aernout Christiaan Zonnevylle was born at 9-March- 1981 in Leiderdorp, The Netherlands. He has a MSc in Applied physic from the Delft University of Technology. He did his PhD research in the Charged Particle Optics group of Professor Kruit at the faculty of Applied Sciences, department of Imaging Physics on the topic of Individual beam control in multi beam systems, sponsored by MAPPER BV and Nano Next nl. During his PhD research a part of his research time was used for developing the SECOM platform that was sponsored by Delft University of Technology. In 2010 he co-founded the company DELMIC BV that specializes in correlative microscopy solutions that can be added to a scanning electron microscope. He started working for Vistec-Gaussian beam lithography (later Raith) in 2013 as an electron optical and system engineer.

Rewards

Finalist TSMC outstanding student research award 2010

2013 Microscopy Today Innovation Award

List of peer reviewed publications

This thesis

A.C. Zonnevylle, C.T.H. Heerkens, P.Kruit, M.L. Wieland, F.M.Postma and S.W.K.H. Steenbrink, Electrostatic rotator for alignment purposes in multi electron beam systems, Microelectronic Engineering 87 (2010) 1095–1099

A.C. Zonnevylle, T.Verduin, C.W. Hagen and P.Kruit. Deflection properties of an electrostatic electron lens with a shifted electrode, J. Vac. Sci. Technol. B 31(6), Nov/Dec 2013

A.C. Zonnevylle, C.T.H. Heerkens, C.W. Hagen and P. Kruit, Multi-Electron-Beam Deflector Array, Microelectronic Engineering 123 (2014) 140–148

A.C. Zonnevylle, R.F.C. van Tol, N. Liv, A.C. Narvaez, A.P.J. Effting, P. Kruit and J.P. Hoogenboom, Integration of a high-NA light microscope in a Scanning Electron Microscope, Journal of Microscopy, Vol. 252, Issue 1 2013, pp. 58–70

Outside this thesis

A.C. Zonnevylle, C.W. Hagen, P. Kruit and A. Schmidt-Ott, Directed assembly of nano-particles with the help of charge patterns created with scanning electron microscope Microelectron. Eng. 86 (2009) 803.

A.C. Zonnevylle, C.W. Hagen, P. Kruit, M. Valenti and A. Schmidt-Ott,, Positioning Pd catalyst particles for carbon nanotube growth using charge patterns created with a scanning electron microscope**,** J. Vac. Sci. Technol. B 27 (2009) 3048.

N. Liv, A.C. Zonnevylle, A.C. Narvaez, A.P.J. Effting, P.W. Voorneveld, M.S. Lucas, J.C.H. Hardwick, R.A. Wepf, P. Kruit and J.P. Hoogenboom, Simultaneous Correlative Scanning Electron and High-NA Fluorescence Microscopy PLoS One 8 (2013) e55707.

A.C. Narvaez, I.G.C. Weppelman, R.J. Moerland, N. Liv, A.C. Zonnevylle, P. Kruit and J.P. Hoogenboom, Cathodoluminescence Microscopy of nanostructures on glass substrates, Optics express, 21(4), (2013)

P.W. Voorneveld, L.L Kodach, J. Rutger, N. Liv, A.C. Zonnevylle, J.P. Hoogenboom, I. Biemond, H.W. Verspaget, D.W. Hommes, K. De Rooij, C.J.M. van Noesel, H. Morreau, T. van Wezel, G.J.A. Offerhaus, G.R. van den Brink, M.P. Peppelenbosch, P. Ten Dijke and J.C.H. Hardwick, Loss of SMAD4 alters BMP signaling to promote colorectal cancer cell metastasis via activation of Rho and ROCK**,** Gastroenterology 147 (2014)

M. T. Haring, N. Liv, A.C. Zonnevylle, A. C. Narvaez, L. M. Voortman, P. Kruit and J. P. Hoogenboom, Automated sub-5nm image registration in correlative fluorescence and electron microscopy using cathodoluminescence pointers, Accepted to Scientific Reports

List of Patents

Multi electron beam detection scheme for multi electron beam transmission scanning, by optical detection, with a hybrid SECOM door as described in chapter 6.

Kruit, Zonnevylle, Yan Ren, Apparatus and method for inspecting a sample using a plurality of charged particle beams, WO2015170969

Multi beam correction method for alignment errors between multi beam array blocks such as rotation or shift misalignment. Chapter 2 and 3 describe a possible application of this patent.

Kruit, Zonnevylle, CHARGED PARTICLE OPTICAL SYSTEM WITH MULTIPLE BEAMS, WO2011034428

Individual beam control in a multi electron beam MEMS based system, an implementation a part is described in chapter 3.

Zonnevylle, Kruit, CHARGED PARTICLE MULTI-BEAMLET APPARATUS, WO2012165955

High NA optical microscope integrated in a SEM by replacing the standard SEM door, as described in chapter 6.

Kruit, Hoogenboom, Zonnevylle, INSPECTION APPARATUS AND REPLACEABLE DOOR FOR A VACUUM CHAMBER OF SUCH AN INSPECTION APPARATUS AND A METHOD FOR OPERATING AN INSPECTION APPARATUS, WO2012008836

Alignment and overlay method for sub 5 nm overlay between light and electron microscope that has been integrated in a SEM, partly described in chapter 6.

Kruit, Hoogenboom, Liv Nalan, Zonnevylle, INTEGRATED OPTICAL AND CHARGED PARTICLE INSPECTION APPARATUS, WO2013151421

Method of producing high NA immersion microscopy in the vacuum of SEM, with an integrated optical microscope, partly described in chapter 6.

Hoogenboom, Zonnevylle, INTEGRATED LIGHT OPTICAL AND CHARGED PARTICLE BEAM INSPECTION APPARATUS, WO2014007624

Alignment of an intergrated optical microscope in a SEM, described in chapter 6.

Hoogenboom, Zonnevylle, Kruit, Narvaez-Gonzalez, INTEGRATED OPTICAL AND CHARGED PARTICLE INSPECTION APPARATUS, WO2014042538